Coupling between the Antarctic ice flow, subglacial regimes and regional climate conditions

Dissertation

zur Erlangung des Doktorgrades
der Naturwissenschaften
vorgelegt von

Jorge Bernales

am Fachbereich Geowissenschaften der Freien Universität Berlin,
angefertigt am Deutschen GeoForschungsZentrum GFZ, Potsdam.

Berlin, 2017

To my family.

Abstract

The Antarctic ice sheet is part of an intricate feedback system that includes the solid Earth, the atmosphere, and the ocean. A deep understanding of the interactions between these subsystems would path the way for improved reconstructions of the Antarctic ice dynamics during past periods, particularly when global climate conditions were similar to those expected in the upcoming centuries. However, the acquisition of observational data needed to strip some of the key ice sheet processes, such as basal ice sliding modulated by the presence of water and soft earth materials, has proven to be difficult due to the particular remoteness and harsh climate conditions of the Antarctic continent. This thesis interconnects three scientific papers to demonstrate that uncertainties in subglacial regimes may explain commonly large discrepancies between the model-based and observed dynamical states of the present-day Antarctic ice sheet and that model-based reconstructions of these regimes can be used to reveal biases in the external forcing.

Until now, most of ice sheet modelling studies have either relied on simplified representations of basal sliding that assume homogeneous bedrock conditions or employed inferences from previous studies as boundary conditions. Using an automated calibration technique of a continental-scale ice-sheet model, the first scientific paper within this thesis deciphers subglacial sliding regimes under the Antarctic ice sheet and shows that they are likely highly heterogeneous across the Antarctic continent. They also appear sensitive to differences in model formulations implying that a direct transfer of such reconstructions from a different model is ill-fated.

Ice shelves respond strongly to the thermal regime of the Southern Ocean that modulates iceberg calving and sub-shelf melting, with the latter being the largest source of ice loss from the Antarctic ice sheet at present. Thus, an accurate representation of ice-shelf basal melting regimes is key to realistic modelling of the Antarctic ice sheet. The second scientific paper uses a combination of an ice sheet model and observations to derive the spatial distribution of melting and freezing rates at the base of the entire Antarctic ice shelf system. This novel technique captures the complexity of the observation-based basal mass balance of ice shelves well, including high ice-shelf melt rates near grounding lines and along the East Antarctic coasts and extensive accretion zones under the largest ice shelves. These estimates appear largely insensitive to uncertainties in the internal model parameters, but respond strongly to changes in the model grid resolution and external forcing. In particular, this study demonstrates that the basal mass balance of ice shelves required by ice sheet models is similar to that inferred from observational studies, and far from the values suggested by commonly utilised parameterisations.

High sensitivity of the reconstructed subglacial regimes of the Antarctic ice sheet to external forcing has motivated the third and last scientific paper included in this thesis. Using ensemble simulations driven by a wide range of atmospheric data sets, this study shows that large biases in the atmospheric forcing can be erroneously compensated through a calibration of highly uncertain ice-sheet model parameters. This error cancellation is difficult to detect if the modelled ice sheet state is analysed in terms of the resulting ice sheet volume and ice distribution only. However, an inclusion of the observed surface flow velocity and ice shelf basal regimes in the validation procedure helps unfolding biases in the climate model outputs.

This thesis reveals that a complementary use of the reconstructed subglacial sliding conditions and sub-shelf melting rates can significantly reduce the discrepancies between the modelled and observed ice geometries and flow patterns over large tracts of the grounded and floating Antarctic ice sheet sectors. Such model-based reconstructions contain large-scale features that are rarely taken into account by modelling experiments of the Antarctic ice sheet, demonstrating that the complexity of the subglacial regimes required by ice sheet models is similar to observed, and far from the inferences of commonly utilised parameterisations. Furthermore, these subglacial regimes can complement observational data sets during the evaluation of climate model reconstructions across Antarctica which traditionally provide external forcing to numerical simulations of future ice sheet changes.

Kurzfassung

Der antarktische Eisschild ist Teil eines komplizierten gekoppelten Systems, bestehend aus der festen Erde, der Atmosphäre und dem Ozean. Ein tiefgreifendes Verständnis der Interaktionen dieser Subsysteme würde den Weg hin zu verbesserten Rekonstruktionen antarktischer Eisdynamiken während vergangener Zeitperioden ebnen; insbesondere während jener Zeitperioden, in denen ähnliche globale klimatische Bedingungen herrschten, wie sie in den bevorstehenden Jahrhunderten erwartet werden. Die Erfassung von Beobachtungsdaten – wie zum Beispiel das basale Gleiten von Eis, welches durch Wasser und weiche Erdmaterialien moduliert wird – hat sich wegen der Abgelegenheit und der harschen klimatischen Bedingungen des antarktischen Kontitents als schwierig erwiesen. Diese Arbeit verbindet drei wissenschaftliche Artikel, um zu demonstrieren, dass Unsicherheiten in subglazialen Regimen die häufig großen Diskrepanzen zwischen modellbasierten und beobachteten dynamischen Zuständen des heutigen antarktischen Eisschildes erklären können und, dass modellbasierte Rekonstruktionen dieser Regime verwendet werden können um Fehler im externen Antrieb aufdecken zu können.

Bis zuletzt stützten sich die meisten Studien zur Eisschild-Modellierung auf eine vereinfachte Representation des basalen Gleitens durch die Annahme homogener Bedingungen des Grundgesteins, oder durch die Ableitung und Anwendung von Randwerten basierend auf vorherigen Studien. Mittels einer automatisierten Kalibrierungstechnik eines kontinentalen Eisschild-Modells entschlüsselt die erste wissenschaftliche Studie dieser Arbeit subglaziale Gleitregime unter dem antarktischen Eisschild und zeigt deren hohe Heterogenität über den gesamten antarktischen Kontinent. Die Gleitregime zeigen sich ebenso sensitiv gegenüber unterschiedlichen Modellformulierungen, was impliziert, dass die Übertragung solcher Rekonstruktionen aus verschiedenen Modellen problematisch ist.

Eisschelfe reagieren besonders auf das thermale Regime des Südlichen Ozeans, welches das Kalben von Eisbergen und Schmelze im Sub-Schelf moduliert, wobei letzteres gegenwärtig die größte Quelle von Eisverlust des antarktischen Eisschildes darstellt. Daher ist eine akkurate Representation basaler Schmelzregime der Eisschelfe essentiell für eine realistische Modellierung des antarktisches Eisschildes. In der zweiten wissenschaftlichen Studie werden ein Eisschild-Modell und Beobachtungen vereint, um räumliche Verteilungen von

Schmelz- und Gefrierraten an der Basis des gesamten antarktischen Eisschildes abzuleiten. Diese neue Technik eignet sich gut, um die Komplexität der Beobachtungs-basierten basalen Massenbilanz von Eisschelfen zu erfassen; insbesondere für die hohen Schmelzraten der Eisschelfe nahe der Aufsatzlinen und entlang der Ost-antarktischen Küste, und für weitreichende Wachstumszonen unter den größten Eisschelfen. Diese Abschätzungen scheinen weitestgehend unsensitiv gegenüber Unsicherheiten der internen Modellparameter, reagieren jedoch stark auf Änderungen in der Gitterauflösung des Modells und im externen Antrieb. Diese Studie zeigt insbesondere, dass die von Eisschild-Modellen benötigte basale Massenbilanz der Eisschelfe vergleichbar ist mit der aus Beobachtungs-basierten Studien und zudem stark von den Werten abweicht, die sich aus den üblicherweise verwendeten Parametrisierungen ergeben.

Die hohe Sensitivität der rekonstruierten subglazialen Regime des antarktischen Eisschildes gegenüber dem externen Antrieb hat die dritte und letzte wissenschaftliche Studie in dieser Arbeit motiviert. Mittels Ensemblesimulationen, erzeugt durch eine breite Auswahl atmosphärischer Datensätze, zeigt diese Studie, dass große Fehler im atmosphärischen Antrieb fälschlicherweise durch die Kalibrierung sehr unsicherer Modellparameter des Eisschildes kompensiert werden können. Diese Fehleraufhebung ist schwierig zu detektieren, wenn der Zustand des modellierten Eisschildes nur anhand des resultierenden Eisschild-Volumens und der Eisverteilung analysiert wird. Die Hinzunahme von beobachteten Oberflächenflussgeschwindigkeiten und basaler Regime des Eisschildes im Validierungsprozess hilft jedoch die Fehler der Klimamodellausgaben aufzudecken.

Diese Arbeit zeigt, dass die komplementäre Verwendung von rekonstruierten subglazialen Gleitbedingungen und Schmelzraten an Subschelfen die Diskrepanzen zwischen modellierten und beobachteten Eisgeometrien und Flussmuster über große Gebiete des grundierten und schwimmenden antarktischen Eisschildes signifikant reduzieren kann. Solche modellbasierten Rekonstruktionen enthalten großskalige Merkmale, die nur selten in Modellexperimenten des antarktischen Eisschildes berücksichtigt werden. Es wird außerdem gezeigt, dass die von Eisschild-Modellen benötigten subglazialen Regime von ähnlicher Komplexität wie beobachtete Regime sind, und stark von allgemein gebräuchlichen Parametrisierungen abweichen. Weiterhin können diese subglazialen Regime bestehende Beobachtungsdatensätze in der Evaluierung von Klimamodell-Rekonstruktionen der gesamten Antarktis ergänzen, welche traditionell den externen Antrieb für numerische Simulationen zukünftiger Änderungen des Eisschildes bereitstellen.

Contents

Chapter 1

Introduction

1.1 The Antarctic ice sheet

The Antarctic continent (Figure 1.1) was a result of the continuous break-up of the supercontinent Gondwana, between 160 and 23 millions of years ago, after a successive separation from the rest of the modern continents (e.g., Jokat et al., 2010). Each separation prompted a change in the global ocean circulation, opening sea gateways that formed latitudinal currents, presumably resulting in more CO_2 draw-down by the ocean due to an increased surface-water nutrient concentration (Zachos et al., 1996). Near the end of this period, global CO_2 levels have decreased significantly, transitioning from a "greenhouse" to an "icehouse" state, and around 34 million years ago the inception of the Antarctic ice sheet occurred (DeConto and Pollard, 2003). These early ice masses (mostly located in the East Antarctic interior) were highly dynamic, advancing and retreating in response to variations in the solar insolation due to Earth's precession and obliquity, and reached a more stable, continental-scale configuration comparable to the present-day ice sheet only about 1.2 million years later (Galeotti et al., 2016).

Starting from its inception, the Antarctic ice sheet has always played a pivotal role in a complex feedback system with the global climate and ocean circulation. Around 23 million years ago, the opening and deepening of the Drake Passage separating Antarctica and South America led to the formation of the Antarctic Circumpolar Current and a definitive isolation of the climate in the Antarctic region that potentially strengthened the ocean's CO_2 reservoir capabilities and further lowered temperatures, thereby cooling the global climate (Fyke et al., 2015). In turn, the growth of the ice sheet triggered shifts in the regional atmospheric patterns due to an increased surface albedo and changes in surface topography, affecting the surrounding ocean conditions through variations in the ocean temperatures, productivity, carbon burial, and sea level (e.g., Hay et al., 2002, and references therein). Although the Antarctic ice sheet has been a permanent feature of the
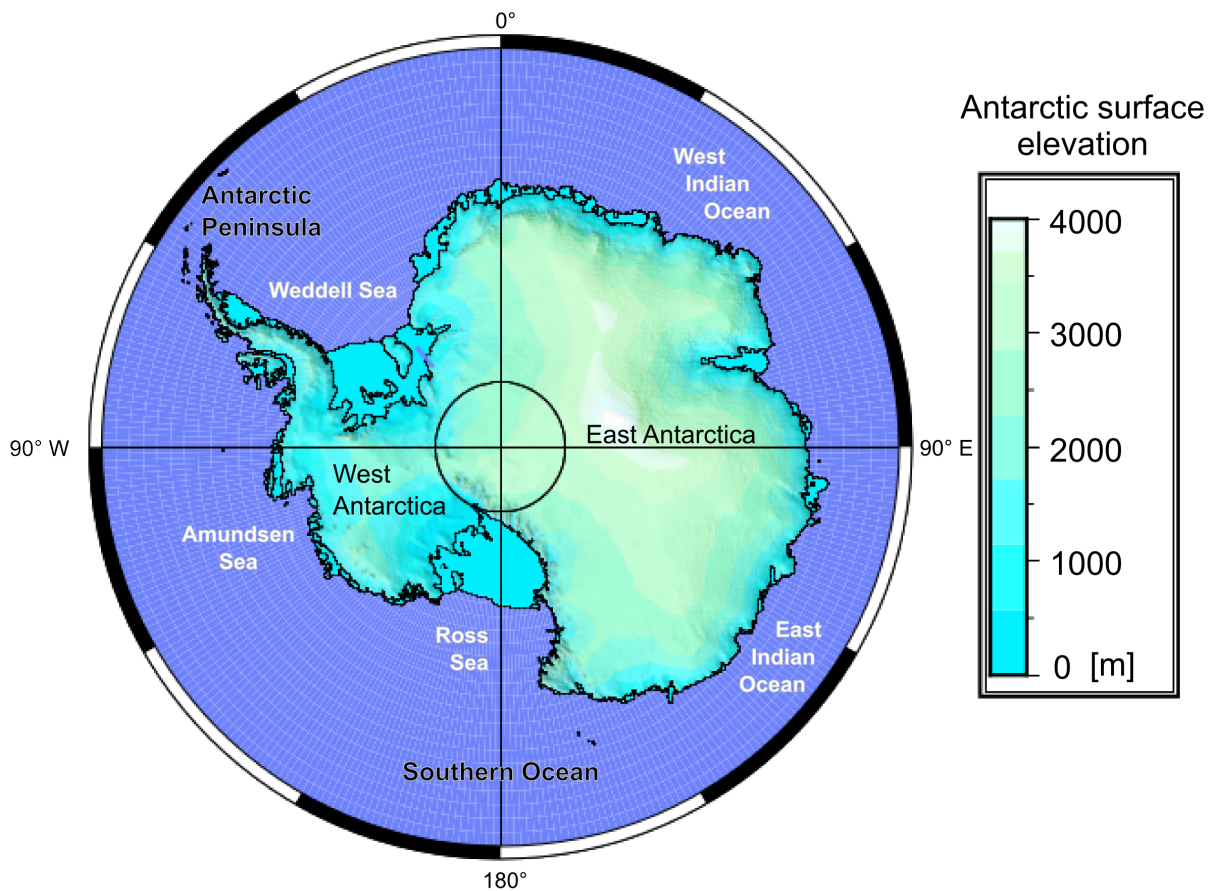
Figure 1.1: A geographical map of the Antarctic region, showing the locations discussed in this chapter. Antarctic topography and positions of grounding lines and ice fronts are based on the BEDMAP2 data set (Fretwell et al., 2013).

Earth's surface in the course of tens of millions of years, its stability has been tightly tied to variations in these surrounding sub-systems, which have caused significant fluctuations in the volume and extent of the ice mass (Naish et al., 2001; Pollard and DeConto, 2009). These fluctuations include the advance, retreat, collapse and re-build of vast regions of the ice sheet over glacial–interglacial cycles, leading to significant changes in the global sea level.

The modern Antarctic ice sheet extends over an area of around $1.2 \times 10^7 \, \text{km}^2$ (about twice the size of Australia), covering approximately 98% of the continent. This ice mass is on average $2 \, \text{km}$ thick and has attained a thickness of up to $4 \, \text{km}$ in some places. Its total ice volume is $2.5 \times 10^7 \, \text{km}^3$, holding enough water to rise the global sea level by $\sim 58 \, \text{m}$ (Fretwell et al., 2013), if all Antarctic ice were to melt. The mass input into the ice sheet is mainly provided by the atmosphere (see Figure 1.2), in the form of liquid (rain) and solid (snow) precipitation, which together with drifting snow transport, runoff, melt water formation, erosion, surface sublimation, retention, and refreezing form the surface mass balance of the ice sheet. The total surface ice mass balance of the grounded

Antarctic ice sheet is currently estimated at approximately $2,000\,\mathrm{Gt\,a^{-1}}$ (Lenaerts et al., 2012; Shepherd et al., 2012), although it is subject to large uncertainties (e.g., Alley et al., 2007) and varies considerably across different ice sheet sectors. The accumulated snow is buried progressively under new layers of snow, and the increasing pressure converts it first into firn, which eventually becomes a solid mass of crystalline glacial ice. The ice is redistributed by thermomechanical feedbacks that transport it from the interior regions towards the ice sheet margins (Clarke et al., 1977). These drainage pathways are dominated by rapidly flowing (several hundreds of meters to a few kilometers per year) ice streams that represent a merger of several tributaries extending hundreds of kilometers inland (Rignot et al., 2011). In many locations, the ice flow that reaches the ocean feeds floating extensions of the coastal glaciers, known as *ice shelves*, that fringe around 75% of the Antarctic ice sheet. They cover a total area of $1.56 \times 10^6\,\mathrm{km^2}$, directly receiving a fifth of the snowfall of Antarctica (Barkov, 1985) that together with the ice flux from the grounded sectors ($\sim 2050 \pm 150\,\mathrm{Gt\,a^{-1}}$) amounts to a total mass input of approximately $2500\,\mathrm{Gt\,a^{-1}}$ (Rignot et al., 2013). Besides the ice inflow and surface mass balance, changes in the ice shelf thickness and geometry are caused by ocean-induced basal melting and refreezing, and calving at the ice front, which together amount to a mass loss of approximately $-2800\,\mathrm{Gt\,a^{-1}}$ and largely dominate the mass loss from the Antarctic ice-sheet-shelf system. Since ice shelves are already floating, these changes have a minimal effect on the sea level variability (Shepherd et al., 2010), mainly due to density and temperature differences between fresh- and sea-water (Jenkins and Holland, 2007). However, they exert an important control on the dynamics of the grounded ice sheet sectors, through buttressing and buffering the ice flux before it reaches the ocean.

The Antarctic ice sheet is often divided geographically into three distinct major sectors: the East and West Antarctic ice sheets, and the Antarctic Peninsula ice sheet (Figure 1.1). The latter is the smallest of the three and has experienced a major atmosphere and ocean warming over the last 50 years (Turner et al., 2005), potentially making it the most vulnerable of the Antarctic ice sheets under the conditions of the global climate change (Davies et al., 2012). The collapse of the Larsen B ice shelf, which fringed the eastern side of the Antarctic Peninsula, coincided with an observed five- to eight-fold peak acceleration of no-longer-buttressed glaciers (Rignot et al., 2004; Rott et al., 2011), showcasing the potential effects of an ice-shelf removal caused by climate variations. In contrast, the East Antarctic ice sheet seems to be in a relatively stable state, even experiencing thickening in some regions (Davis et al., 2005) that can be explained by an increased snowfall under warmer climate conditions (Ligtenberg et al., 2013). Finally, the West Antarctic ice sheet has been the topic of an extensive scientific debate during the last decades (e.g., Bamber and Aspinall, 2014). This ice sheet is grounded well below the sea level (Fretwell et al.,
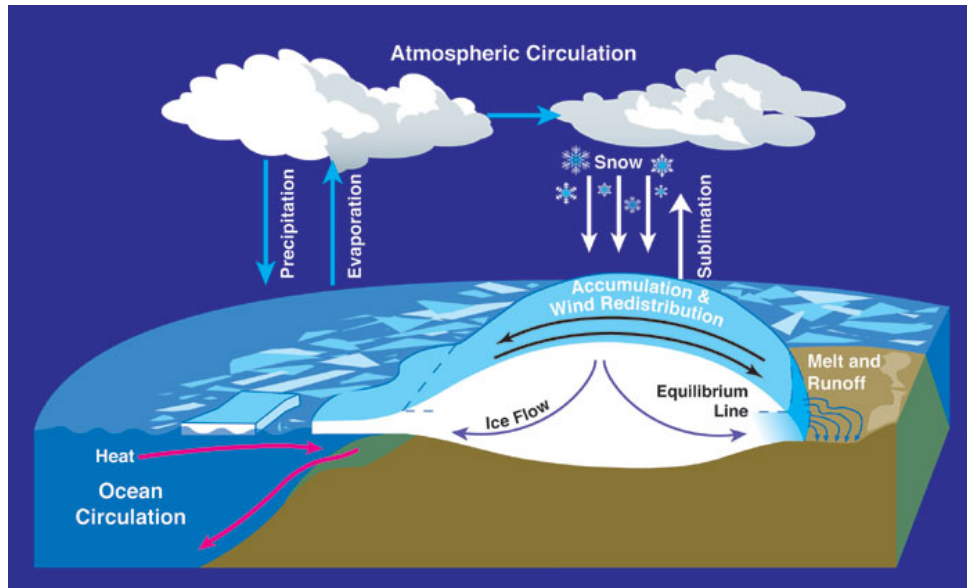
Figure 1.2: A schematic representation of the processes involved in glacier mass balance. Original figure by NASA. Adapted from Wikimedia Commons.

2013) on a bedrock that in many places deepens inland, thus opening the possibility of a marine ice-sheet instability in the form of a rapid deglaciation under global warming conditions (Mercer, 1978; Joughin and Alley, 2011). A partial or complete disintegration of the West Antarctic ice sheet would lead to a significant sea-level rise of up to 5 m (Bamber et al., 2009). There is evidence suggesting that the West Antarctic ice sheet collapsed in the past (e.g., Scherer et al., 1998; Naish et al., 2009), during interglacial periods when global temperatures were similar to some of those projected for the next centuries. Examples of such past periods can be used to deepen our understanding of the Antarctic ice sheet sensitivity to potential climate warming scenarios (e.g., de Boer et al., 2015). Because changes in the Antarctic ice sheets can have a profound impact on the global climate system and large societal consequences (IPCC, 2013), studies of the Antarctic ice masses and their complex interactions with other Earth sub-systems have become a focus of many scientific programs.

1.2   Modelling the flow of an ice sheet

Due to the high complexity of the feedbacks between the Antarctic ice sheet, the atmosphere, the ocean, and the underlying bedrock, making accurate predictions of the future ice sheet behaviour has proven to be difficult without gaining first a better understanding of both its current state and its sensitivity to external influences of the other sub-systems. In the last decades, an increasing availability of remote-sensing–based measurements (particularly satellite and airborne observations) has provided a continental-scale picture

of the Antarctic ice sheet dynamics, supplying valuable information on the ice sheet behaviour across remote regions where in situ measurements are currently not feasible. Examples of such data sets include ice-sheet mass balance (e.g., Velicogna and Wahr, 2013; Martín-Español et al., 2016), ice sheet thickness and elevation (Fretwell et al., 2013), and surface velocities (Rignot et al., 2011), with significant contributions to the determination of, e.g., changes in the ice-sheet topography and ice-shelf basal mass balance (Rignot et al., 2013; Depoorter et al., 2013). These observations can be used as input data in numerical ice-sheet models that incorporate mathematical representations of the key processes at play, which are in turn translated into a computer code in order to simulate the ice sheet behaviour under hypothetical scenarios. Once a model is calibrated and validated against observational data, it can be used to perform predictive experiments that aim to provide possible answers to general questions regarding, for example, the ice sheet stability and sea-level contribution under warmer-than-present climate conditions, or more specific information about the likelihood, timing, and extent of significant events, such as a potential collapse of the West Antarctic ice sheet.

The next paragraphs summarise and follow closely the comprehensive derivation by Greve and Blatter (2009) of the equations found at the core of the state-of-the-art in ice flow modelling, to which the reader is referred for further details. Starting from Newton's Second Law, the mathematical description of the ice dynamics starts from the momentum balance equation

$$\rho \frac{\mathrm{d}\mathbf{v}}{\mathrm{d}t} = \nabla \cdot \mathsf{t} + \mathbf{f} \; , \tag{1.1}$$

where the temporal change of the momentum (left-hand side of Eq. (1.1)) is equal to the sum of the internal and external forces acting on an ice element (first and second terms on the right-hand side of Eq. (1.1), respectively). Here, ρ and $\mathbf{v}$ are the mass density and velocity of the ice, respectively, and t is a tensor representing the internal stresses acting within the ice. The external forces $\mathbf{f}$ include the gravity field and the inertial centrifugal and Coriolis forces:

$$\mathbf{f} = \rho \mathbf{g} - 2\rho \boldsymbol{\Omega} \times \mathbf{v} \; , \tag{1.2}$$

where $\rho \mathbf{g}$ is the effective force of gravity (including the dependence on position of the centrifugal force), $\mathbf{g}$ is the gravitational acceleration, and $\boldsymbol{\Omega}$ is the angular velocity of the Earth. For a viscous material such as ice, the internal stress tensor t is related to the deformation and velocity gradients. If glacier ice is assumed to be incompressible, that is $\nabla \cdot \mathbf{v} = 0$, t can be decomposed as (Greve and Blatter, 2009)

$$\mathsf{t} = -\frac{1}{3}\mathrm{tr}(\mathsf{t}) + \mathsf{t}^{\mathrm{d}} = -P\mathsf{I} + 2\eta\mathsf{D} \; , \tag{1.3}$$

where $\text{tr}(\cdot)$ represents the trace operator, $\mathsf{t}^{\mathrm{d}} = 2\eta\mathsf{D}$ is the traceless stress component, P is the pressure, I is the unit tensor, η is the ice shear viscosity, and D is a strain-rate (stretching) tensor that depends on the velocity gradient. For the type of ice found in glaciers and ice sheets (a deformable polycrystalline compound), the viscosity η is assumed to depend not only on the ice temperature T, but also on its internal deformation. This relation is usually described through an empirical flow law in the form (Glen, 1955; Nye, 1957)

$$\eta(T_{\mathrm{m}}, \sigma_e) = \frac{1}{2A(T_{\mathrm{m}})[\sigma_e^{n-1} + \sigma_0^{n-1}]} \;, \tag{1.4}$$

where T_{m} is the temperature relative to the pressure melting point of ice, σ_e is the effective stress, defined as $\sigma_e = \sqrt{\frac{1}{2}\text{tr}(\mathsf{t}^{\mathrm{d}})^2}$, A is a temperature- and pressure-dependent *rate factor* (Paterson, 1994), σ_0 is a small positive constant introduced to avoid singularities where σ_e is very small, and n is a power-law exponent, usually chosen as $n = 3$ (e.g., Paterson, 1994; van der Veen, 1999).

In order to derive an equation of motion for the ice dynamics, Eqs. (1.2) and (1.3) are inserted into the right-hand side of Eq. (1.1), yielding

$$\rho\frac{\mathrm{d}\mathbf{v}}{\mathrm{d}t} = -\nabla P + \eta\nabla^2\mathbf{v} + (\nabla\mathbf{v} + (\nabla\mathbf{v})^{\mathrm{T}})\cdot\nabla\eta + \rho\mathbf{g} - 2\rho\boldsymbol{\Omega}\times\mathbf{v} \;. \tag{1.5}$$

An analysis of the ratios of typical vertical to horizontal lengths of ice sheets and velocities (often called *aspect ratios*) reveals that the ice acceleration and Coriolis force terms in Eq. (1.5) are negligible in comparison to the pressure gradient term (Greve and Blatter, 2009). Thus, Eq. (1.5) can be simplified to

$$-\nabla P + \eta\nabla^2\mathbf{v} + (\nabla\mathbf{v} + (\nabla\mathbf{v})^{\mathrm{T}})\cdot\nabla\eta + \rho\mathbf{g} = \mathbf{0} \;, \tag{1.6}$$

which is known as the *Stokes equation*, central to the modelling of the ice sheet flow. To account for the dependence of the viscosity η on the ice temperature (Eq. (1.4)), an evolution equation for the temperature field is introduced in the form (Greve and Blatter, 2009)

$$\rho c\frac{\mathrm{d}T}{\mathrm{d}t} = \nabla\cdot(\kappa\nabla T) + 4\eta d_e^2 \;, \tag{1.7}$$

where c is the specific heat, κ the heat conductivity, and d_e the effective strain rate, defined as $d_e = \sqrt{\frac{1}{2}\text{tr}(\mathsf{D}^2)}$. The solution for the ice velocity field of the resulting equation system (incompressibility, motion, viscosity, and temperature equations) is vertically integrated to compute the volume flux $\mathbf{Q}$, which enters an evolution equation for the ice thickness in the form

$$\frac{\partial H}{\partial t} = -\nabla\cdot\mathbf{Q} + a_s - a_b \;, \tag{1.8}$$

where the source/sink terms a_s and a_b represent the vertical component of the surface mass balance and basal melt rate, respectively.

The mathematical description presented above forms the core of the *Full Stokes* ice flow models. However, its numerical formulation is associated with very high expenses in terms of computational resources required to solve the resulting system of non-linear equations in large-scale (e.g., continental-size ice sheets) and/or long-term (thousands of years) simulations. To overcome this limitation, the momentum balance is often simplified by neglecting a number of terms based on their relative significance and/or aspect ratios, giving rise to a variety of approximations to the Full Stokes model (Hindmarsh, 2004). For example, the *hydrostatic approximation* (also described in Greve and Blatter, 2009) equals the magnitude of the vertical normal stress to that of the hydrostatic pressure, which is large compared to the shear stresses. As a result, the shear stresses are neglected from the vertical component of the momentum balance, and the explicit dependence on the unknown pressure field is eliminated. The hydrostatic approximation can be further simplified by comparing the components of the velocity gradient included in Eq. (1.3) and neglecting the horizontal derivatives of the vertical velocity, which are much smaller than the vertical derivatives of the horizontal velocities. This effectively eliminates the dependence on the vertical velocity, which can be computed independently once the horizontal velocities are determined, using the continuity condition for an incompressible material $\nabla \cdot \mathbf{v} = 0$. On the one hand, under certain conditions (small surface and basal slopes, significant basal drag, and away from the ice-sheet margins and ice divides), the approximated hydrostatic ice flow described above is dominated by the horizontal shear stresses. Therefore, a final simplification can be applied to the hydrostatic approximation by neglecting all other stress components except for the normal stresses, resulting in the *shallow ice approximation* (Hutter, 1983; Greve and Blatter, 2009), which represents a considerable reduction in the computational expenses required to perform large-scale, long-term ice-sheet model simulations. On the other hand, ice shelves floating in sea water experience almost no friction at their base, and their behaviour is often described by the *shallow shelf approximation* (Morland, 1987; Greve and Blatter, 2009), which omits vertical shear stress and neglects basal drag. However, at the transition between grounded and floating ice regions, the membrane stresses neglected in the shallow ice approximation become increasingly important, since rapidly flowing features known as ice streams dominate the ice flow in these sectors. In these regions, current continental-scale ice-sheet models reproduce ice stream dynamics using a variety of approaches, ranging from depth-integrated Blatter–Pattyn models (Blatter, 1995; Pattyn, 2003) to *hybrid* models that employ heuristic combinations of the shallow ice and shallow shelf approximations, the latter including a non-negligible basal drag (Bueler and Brown, 2009; Winkelmann et

al., 2011; Bernales et al., 2017a,b).

1.3   Current challenges in ice-sheet modelling

Independently of the degree of simplification, a common difficulty with state-of-the-art numerical ice flow models is the incorporation of many important processes that are not well understood. For example, glacier sliding at the base of an ice sheet contributes to the formation of rapidly flowing ice streams and relatively high speeds of some outlet glaciers, which are also influenced by other factors such as the deformation and failure of sub-glacial sediments, the existence of water-filled cavities, the presence of obstacles, and many other external agents (Fowler, 2010; Winsborrow et al., 2010). These processes are difficult to separate due to an inability of current observational techniques to penetrate the kilometers-thick Antarctic ice sheet at a sufficiently large scale and provide high-quality, homogeneously distributed observations of the ice-bedrock interface. As a result, most of these processes are commonly represented in ice-sheet models in an implicit manner by empirical sliding laws (Fowler, 2010), which at their core assume the basal velocity to be proportional to some power of the basal shear stress. The proportionality is realised through an adjustable parameter called *basal sliding coefficient* that strongly influences the ice flow in the areas where the occurrence of basal sliding is predicted by the model (e.g., Dunse et al., 2011). Since an accurate prescription of this poorly constrained parameter is crucial for the correct application of ice flow models, its determination has been the subject of many recent studies, using a variety of approaches, models, and sliding laws (e.g., Joughin et al., 2009; Morlighem et al., 2010; Pollard and DeConto, 2012b; Arthern et al., 2015).

Ocean-induced melting and freezing at the base of the ice shelves represents another example of a crucial process that remains difficult to implement in large-scale ice-sheet models. This is due to a large number of variable mechanisms that influence the ocean thermal forcing, such as the cooling effect of high-salinity water production and the incursions of warm waters from the Antarctic Circumpolar Current (e.g., Pritchard et al., 2012). These could be potentially derived from high-resolution ocean models capable of simulating the circulation in the shape-variable ice shelf cavities (e.g., Schodlok et al., 2012; Padman et al., 2012; Hellmer et al., 2012), but such model-based reconstructions over sufficiently long time spans are currently lacking. In addition, a correct implementation of the simulated ocean-forcing as a time-variable boundary condition would require improved ice-sheet models that can accurately and efficiently simulate the ice dynamics in the grounding-line zone and calving fronts (e.g., Pattyn et al., 2013). For these reasons, the implementation of ice-ocean interaction in stand-alone continental-scale ice-sheet models
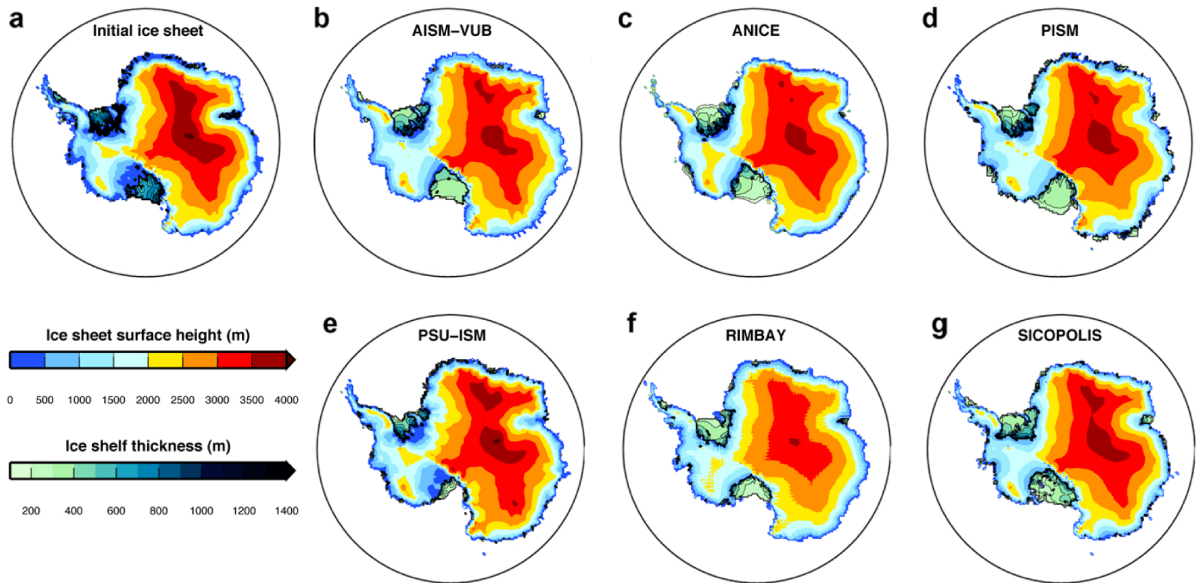
Figure 1.3: Ice surface topography and thickness of ice shelves for a present-day equilibrium simulation from the collaboration study of de Boer et al. (2015), forced by climate and oceanic outputs from the global circulation model HadCM3 (Bragg et al., 2012). (a) Reference ice sheet-shelf configuration from the BEDMAP1 data set (Lythe et al., 2012). (b–g) Equilibrium ice sheet-shelf configuration after $100,000$-years-long simulations from different continental-scale ice sheet models, including a previous version of the model SICOPOLIS used in this thesis. Adapted from de Boer et al. (2015).

has mostly relied on simplified parameterisations that range from a simple, single-value basal melt rate applied to the entire ice-shelf domain (e.g., Sato and Greve, 2012) to more elaborated models that compute this forcing at varying depths utilizing the mass and heat fluxes between ice and ocean (e.g., Beckmann and Goosse, 2003; Holland et al., 2008), based on 3D ocean temperature and salinity fields generated by ocean circulation models (e.g., de Boer et al., 2015). Since these parameterisations are often primarily calibrated to yield target total ice-sheet volumes and/or area extents, the resulting distributions of basal melting and freezing rates do not necessarily reproduce the complex patterns of basal thermal regimes of ice shelves as reported in recent observational studies (e.g., Rignot et al., 2013; Depoorter et al., 2013).

Finally, it is important to keep in mind that the present-day state of the Antarctic ice sheet is a result of the deglaciation process that started between $20,000$ and $15,000$ years ago, after the Last Glacial Maximum when the ice sheet covered most of the Antarctic continental shelf (Bentley et al., 2014). This deglaciation may still exert an influence on the ice dynamics through processes such as post-glacial rebound or the remanent signal in the internal ice sheet temperatures from a much colder time period. Geological and glaciological reconstructions of this recent deglaciation are crucial to our understanding of the Antarctic ice sheet responses to documented and potential changes in the climatic and oceanographic forcing, since they provide the ice sheet modelling community with

data against which models can be tested and constrained. However, the observational record prior to the satellite era is still sparse and heterogeneous. In addition, the climate forcing required by continental-scale ice-sheet models to predict the responses of ice sheets to past and potential future climate variations is usually provided by global-scale climate models that differ significantly and often disagree with observations in polar regions, due to their insufficient horizontal resolution ($\sim 100\,\mathrm{km}$) and a lack of polar-oriented physics (e.g., Agosta et al., 2015). Therefore, accurate model-based reconstructions and future predictions of the Antarctic ice sheet dynamics require a solid assessment of the impact of such disagreements on the model results. Furthermore, such assessment would allow for an identification of biases in both climate and ice sheet models, representing a critical step towards an inclusion of ice-sheet–climate feedbacks in more complex coupled models that include other Earth sub-systems.

1.4   Aims and structure of this thesis

The significance of the challenges described in the previous section was demonstrated in an initial collaborative study carried out at the beginning of the present project, published as de Boer et al. (2015). In this study, different state-of-the-art ice sheet models —including a preliminary version of the model used in this thesis— were used to reconstruct the geometry of the Antarctic ice sheet during the mid-Pliocene warm period and its contribution to the sea-level high stand relative to the present day (e.g., Raymo et al., 2011). During the validation phase where the modelled present-day Antarctic ice thickness was compared to observations (Figure 1.3), the ice-sheet configurations from all models presented:

i) widespread differences between the modelled and observed ice-sheet and ice-shelf thickness locally reaching several hundreds of meters. Additional experiments suggested that these errors can be largely attributed to uncertainties in the basal sliding conditions and their limited model representation, which together have a strong impact on the modelled ice flow patterns and geometries,

ii) disagreements between the positions of the ice fronts and the grounding line (which separates the grounded ice sectors from ice shelves), mainly due to lack of high-quality ocean data in the ice shelf cavities and an over-simplified model treatment of the ocean-ice interactions, and

iii) significant discrepancies between the resulting ice sheet geometries from experiments driven by a different set of model-based atmospheric and oceanic forcing, reflecting a potentially strong model sensitivity to the uncertainties and biases in external data sets.

The need to resolve these issues has been identified as a key step towards the inclusion of numerical ice flow models in future projections of climate and sea-level variability, and will

be central to an extensive research in the following years (e.g., Nowicki et al., 2016; Eyring et al., 2016). This thesis aims to contribute to the exciting research of the above-mentioned interactions between the ice sheet and the surrounding sub-systems: bedrock, ocean, and atmosphere. In particular, this thesis investigates the following questions:

- Can uncertainties in subglacial sliding conditions and ocean-induced sub-shelf melting explain large deviations between the model-based and observed geometries and flow regimes of the present-day Antarctic ice sheet?

- Are model-based reconstructions of these subglacial regimes below the grounded and floating ice sheet sectors in agreement with available observations?

- Can ice-sheet modelling experiments reveal biases and errors in the external model forcing and other boundary conditions?

To answer these questions, three consecutive and complementary studies have been carried out using a numerical model of the Antarctic ice sheet and the surrounding ice shelves. These studies present new features developed within the model to address the three major questions discussed above and have materialised into three scientific manuscripts that are, at the time of the thesis writing, either published or in review. These three studies form the core chapters of the present cumulative thesis and are bridged together by context passages that describe how each study provides the foundation to the follow-on research. The first study (Chapter 2) focuses on the ice-bedrock interface, investigating how the choice of different approximations of the momentum-balance equations impacts reconstructions of the mechanical properties of the subglacial bedrock and basal sliding of rapidly flowing ice sheet sectors. The second study (Chapter 3) focuses on the ice-ocean interaction, and presents a new reconstruction of basal melting and freezing rates for the entire Antarctic ice-shelf system using a novel combination of an ice sheet-shelf model and a calibration technique. Building upon the outcomes of these two studies, the third study (Chapter 4) focuses on the ice-atmosphere interaction and investigates the possibility of using model-based reconstructions of subglacial regimes below the Antarctic ice sheet to complement observational data during the evaluation of external model-based climate reconstructions. Finally, Chapter 5 summarizes the results of this thesis and presents directions for future research.

Chapter 2

Comparison of hybrid schemes for the combination of shallow approximations in numerical simulations of the Antarctic Ice Sheet

Chapter Abstract

The shallow ice approximation (SIA) is commonly used in ice-sheet models to simplify the force balance equations within the ice. However, the SIA cannot adequately reproduce the dynamics of the fast flowing ice streams usually found at the margins of ice sheets. To overcome this limitation, recent studies have introduced heuristic hybrid combinations of the SIA and the shelfy stream approximation. Here, we implement four different hybrid schemes into a model of the Antarctic Ice Sheet in order to compare their performance under present-day conditions. For each scheme, the model is calibrated using an iterative technique to infer the spatial variability in basal sliding parameters. Model results are validated against topographic and velocity data. Our analysis shows that the iterative technique compensates for the differences between the schemes, producing similar ice-sheet configurations through quantitatively different results of the sliding coefficient calibration. Despite this we observe a robust agreement in the reconstructed patterns of basal sliding parameters. We exchange the calibrated sliding parameter distributions between the schemes to demonstrate that the results of the model calibration cannot be straightforwardly transferred to models based on different approximations of ice dynamics. However, easily adaptable calibration techniques for the potential distribution of basal sliding coefficients can be implemented into ice models to overcome such incompatibility, as shown in this study.

2.1 Introduction

Accurate projections of ice-sheet-driven sea level changes require the use of numerical models that are capable of capturing the dynamics of rapidly flowing regions and grounding-line zones (Pattyn et al., 2013). This requirement can be best accommodated using the most complete models currently available for modelling the ice dynamics, referred to as full Stokes (FS) models (e.g., Gagliardini et al., 2013). However, the timescales over which an ice sheet builds up and disintegrates in response to variations in the climatic forcing typically involve many thousands of years. Numerical experiments over such time spans are necessary to separate the long term transient component from relatively fast fluctuations in the ice volume during the observational record. These long-term, continental-scale palaeo-simulations are currently infeasible using FS models due to the computational expenses triggered by the non-linearity of the model equations and the complex interdependence of the involved quantities.

To overcome the contemporary spatio-temporal limitations of FS models, a hierarchy of approximations has been developed over the last decades (e.g., Hindmarsh, 2004). The shallow ice approximation (SIA; Hutter, 1983) is a zeroth-order approximation of the momentum balance equations that keeps only the gravity-driven vertical shear stress, predicting reasonably well the behaviour of grounded ice masses which are characterised by a thickness much smaller than their horizontal length scales. Ice floating in the sea water experiences almost no friction at the base, and its behaviour is often described by the shallow shelf approximation (SSA; Morland, 1987), which omits the vertical shear stress from the FS equations and neglects the basal drag. The transition between grounded and floating ice regions exhibits areas where ice flow is often enhanced by basal conditions favourable for sliding, generating rapid ice flow features known as ice streams. In these ice-sheet sectors membrane stresses become increasingly important, sharing many similarities with the ice shelves, and thus the SIA is no longer appropriate to describe the ice dynamics. It is also important to note that the absence of a membrane stress transfer in the SIA renders this approximation invalid for modelling the grounding line migration, i.e. the migration of an interface between grounded and floating ice sectors (Pattyn et al., 2012).

More sophisticated methods have been designed to overcome the limitations of SIA models when reproducing the dynamics of ice streams, which still aim at low computational costs. The approaches used by this new generation of continental-scale ice-sheet models include depth-integrated Blatter–Pattyn models (Blatter, 1995; Pattyn, 2003) based on

the asymptotic analysis by Schoof and Hindmarsh (2010), algorithms that detect and use the SIA where it is applicable and the FS elsewhere (Ahlkrona et al., 2016), and so-called hybrid models utilising heuristic combinations of the SIA and the shelfy stream approximation (SStA, which is the SSA including basal drag; Bueler and Brown, 2009; Winkelmann et al., 2011; Pollard and DeConto, 2012a). These hybrid models utilise a number of algorithms to identify zones of potential fast flow where ice streams may operate and then combine contributions of each approximation based on predefined criteria. The use of hybrid models enables simulations over hundreds of thousands of years on continental scales, yet show a reasonable performance compared to higher-order models in idealised scenarios and intercomparison tests (e.g., Pattyn et al., 2013; Feldmann et al., 2014). Since the combination of the SIA and the SStA is based on heuristics, the approaches used to combine the two approximations vary from model to model, ranging from weighted averages of both velocity solutions to a simple summation over the entire domain.

Despite the above differences among existing models, all of them are subject to common limitations when applied to the present-day Antarctic Ice Sheet (AIS). These limitations include the scarcity of observational data needed to reduce the errors introduced by poorly constrained model parameters and boundary conditions, e.g., the flow enhancement factors introduced to account for anisotropy of ice flow, geothermal heat flux, glacial isostatic adjustment, and distribution of water-saturated sediments at the ice-sheet base. The latter has the potential to enhance basal sliding and is currently considered to be a major source of large, widespread misfits between the observed and modelled elevations of the AIS (e.g., de Boer et al., 2015). Recent studies have attempted to quantify potential distributions of these intrinsic bed properties using sophisticated inverse methods (e.g., Joughin et al., 2009; Morlighem et al., 2010; Arthern and Gudmundsson, 2010; Pralong and Gudmundsson, 2011; Arthern et al., 2015). These diagnostic methods focus mainly on the fit between the modelled and observed ice velocities. Pollard and DeConto (2012b) presented a much simpler algorithm, aiming to fit the observed surface elevations instead of velocities. The prognostic model is run forward in time, and the local elevation error is used to periodically adjust the basal sliding parameters until the best fit between the observed and modelled elevations is attained. This procedure has the ability to drastically reduce large elevation errors during the calibration and initialisation of ice-sheet models, which is an important requirement for simulations that would otherwise be undermined

by poor parameter choices.

In this paper, we evaluate the performance of four different hybrid schemes implemented as part of the same continental-scale ice-sheet model, applied to the entire AIS. To this end, a calibration procedure based on the aforementioned iterative technique of Pollard and DeConto (2012b) is applied to each hybrid scheme. For comparison purposes, the same procedure is carried out using a SIA-only model. The results of these experiments are validated against an independent, observational data set of surface ice velocities (Rignot et al., 2011). Additionally, we provide insights into the relative contributions of the shallow approximations in different hybrid schemes. By exchanging the inferred distributions of basal sliding parameters between the applied hybrid schemes, we test the applicability of the model calibration results in different types of ice flow models. For hybrid approaches involving adjustable parameters, we also explore the sensitivity of the results to parameter variations. First, the ice-sheet model and the hybrid schemes are described in Section 2.2, where we also detail the adapted iterative technique for the calibration of the basal sliding parameters. The observational and model-based data sets used in our simulations are described in Section 2.3. The set-up of the numerical experiments can be found in Section 2.4. The results are presented and discussed in Section 2.5, followed by the summary and conclusions provided in Section 2.6.

2.2 Methods

2.2.1 Model overview

In this study, the simulations of the AIS are carried out using the open source, three-dimensional, thermomechanical ice sheet–shelf model SICOPOLIS (SImulation COde for POLythermal Ice Sheets) version 3.2-dev, revision 619 (Greve, 1997; Greve and Blatter, 2009; Sato and Greve, 2012). It uses finite differences to solve the numerically approximated SIA and SSA equations for grounded and floating ice, respectively. Relevant modifications introduced in the model specifically for this study are presented in a greater detail in Sections 2.2.2 and 2.2.3.

SICOPOLIS is applicable for the modelling of polythermal ice sheets; i.e. it explicitly identifies potential temperate regions in which the modelled ice temperature is at the pressure-melting point (Greve, 1997). Within these regions, ice and small amounts of liquid water can coexist, and the water content is used as an additional input for a regularised

Glen's flow law (Glen, 1955) utilised in our experiments, following Greve and Blatter (2009), in the form

$$\eta\left(T_{\mathrm{m}}, \sigma_{\mathrm{e}}\right) = \frac{1}{2EA\left(\sigma_{\mathrm{e}}^{n-1} + \sigma_0^{n-1}\right)}, \tag{2.1}$$

where η denotes ice shear viscosity, T_{m} is the temperature difference relative to the pressure melting point, σ_{e} is the effective shear stress, $\sigma_0 = 10\,\mathrm{kPa}$ is a small constant used to prevent singularities when σ_{e} is very small, $n = 3$ is the flow law exponent, and A is a temperature- and pressure-dependent rate factor (Cuffey and Patterson, 2010). In temperate ice regions, A is modified to account for the aforementioned water content, following Lliboutry and Duval (1985). The empirical coefficient E is a flow enhancement factor, which is introduced to account for the effects of anisotropic ice fabric. The value of E depends on the deformation regime of ice, which is different for grounded ice, where horizontal shear prevails, and floating ice, dominated by longitudinal stretching (Ma et al., 2010). In general, large-scale marine ice-sheet models use a homogeneous, constant value ranging between 1 and 8 for the grounded ice and between 0.2 and 1 for ice shelves (e.g., de Boer et al., 2015). Within these ranges, the computed age of ice is often used to assign different values for glacial and interglacial ice. Here, we use $E = 1$ and $E = 0.5$ for grounded and floating ice, respectively. These values are smaller than those chosen in previous studies using SICOPOLIS (e.g., Sato and Greve, 2012) and are based on our initial tests and the sensitivity analysis by Pollard and DeConto (2012b).

At the base of the grounded ice sectors, stress conditions at the bedrock and the associated potential for sliding are linked to the basal velocity, $\vec{u}_{\mathrm{b}}$, used as a boundary condition for the computation of the SIA velocities, through an empirical Weertman-type sliding law (Weertman, 1964; Dunse et al., 2011), in the form

$$\vec{u}_{\mathrm{b}} = -\frac{C_{\mathrm{b}}}{N_{\mathrm{b}}^q}|\vec{\tau}_{\mathrm{b}}|^{p-1}\vec{\tau}_{\mathrm{b}}, \tag{2.2}$$

where $\vec{\tau}_{\mathrm{b}}$ is the basal shear stress, and $p = 3$ and $q = 2$ are the sliding law exponents. N_{b} is the effective basal pressure, computed as

$$N_{\mathrm{b}} = \rho_{\mathrm{ice}}gH - \rho_{\mathrm{sw}}gH_{\mathrm{sw}}, \tag{2.3}$$

where ρ_{ice} and ρ_{sw} are the density of ice and sea water, respectively, g is the gravitational

Table 2.1: Symbols and values for the model parameters used in this study.

Symbol	Description	Units	Value
g	gravitational acceleration	$\mathrm{m\,s^{-2}}$	9.81
ρ	density of ice	$\mathrm{kg\,m^{-3}}$	910
T	absolute temperature of ice	K	
T_m	temperature below pressure-melting point	K	
κ	heat conductivity of ice	$\mathrm{W\,m^{-1}\,K^{-1}}$	$9.828\,e^{-0.0057T}$
c	specific heat of ice	$\mathrm{J\,kg^{-1}\,K^{-1}}$	$146.3 + 7.253T$
L	latent heat of ice	$\mathrm{kJ\,kg^{-1}}$	335
β	Clausius–Clapeyron gradient	$\mathrm{K\,m^{-1}}$	8.7×10^{-4}
R	universal gas constant	$\mathrm{J\,mol^{-1}\,K^{-1}}$	8.314
κ_r	heat conductivity of the lithosphere	$\mathrm{W\,m^{-1}\,K^{-1}}$	3
$\alpha_\mathrm{ice},\ \alpha_\mathrm{snow}$	PDD factors for ice and snow	$\mathrm{mm\,d^{-1}\,^{o}C^{-1}}$	8, 3
α_std	PDD standard deviation	^{o}C	5
σ_e	effective shear stress	Pa	
σ_0	residual stress	kPa	10
$E_\mathrm{SIA},\ E_\mathrm{SSA}$	enhancement factor for the SIA and SSA		1, 0.5
A	ice rate factor	$\mathrm{s^{-1}\,Pa^{-3}}$	
n	Glen flow law exponent		3
$\vec{u}$	horizontal SIA velocity	$\mathrm{m\,s^{-1}}$	
$\vec{v}$	horizontal SStA velocity	$\mathrm{m\,s^{-1}}$	
$\vec{U}$	horizontal hybrid velocity	$\mathrm{m\,s^{-1}}$	
v_0	regularisation speed in SStA equations	$\mathrm{m\,yr^{-1}}$	0.01
$\vec{\tau}_\mathrm{b}$	basal shear stress	Pa	
N_b	effective basal pressure	Pa	
$p,\ q$	sliding law exponents		3, 2
γ	sub-melt-sliding parameter	K	3
C_0	calibrated basal sliding parameter	$\mathrm{m\,yr^{-1}\,Pa^{-1}}$	
Δt_inv	time step for inversion of C_0	yr	50
H_inv	scaling factor for calibration of C_0	m	5000
r	slip ratio of grounded ice		
r_thr	default threshold value of r		0.5
v_ref	default reference value of $|\vec{v}|$	$\mathrm{m\,yr^{-1}}$	100
w	weighting function in hybrid schemes		
h_rlx	scaling factor for relaxation procedure		0.001

acceleration, H is the modelled ice thickness, and H_{sw} is the difference between the mean sea level and the ice base topography. The parameter C_{b} depends on the basal temperature and pressure conditions:

$$C_{\mathrm{b}} = C_0 e^{T_{\mathrm{m}}/\gamma},\tag{2.4}$$

where the exponential function controls the amount of sliding, depending on the temperature below the pressure-melting point T_{m} and the sub-melt-sliding parameter γ, ensuring a smooth transition across different basal thermal regimes and, thus, prohibiting discontinuities in the velocity field (Bueler and Brown, 2009). A spatially varying factor C_0 is introduced to account for differences in the bedrock material properties affecting sliding (e.g., hard bedrock vs. soft sediments). Potential distributions of C_0 have been explored using different iterative and inverse approaches and a variety of sliding laws, aiming to find spatially varying values that minimise the discrepancy between the modelled and observed quantities such as ice thickness, ice surface velocity, and elevation change (e.g., Joughin et al., 2009; Morlighem et al., 2010; Arthern and Gudmundsson, 2010; Pralong and Gudmundsson, 2011; Pollard and DeConto, 2012b; Arthern et al., 2015). A particular iterative technique implemented in our model is described in Section 2.2.3. Other model components include evolution equations for ice temperature and ice thickness, with the latter forced by independent modules for the computation of the surface and basal mass balances (Greve and Blatter, 2009; Sato and Greve, 2012). A summary of the model parameters used in this study is provided in Table 2.1.

2.2.2 Hybrid schemes

For this study, four hybrid approaches have been implemented into the model. Each of them offers a different way to identify the fast flowing zones and combine the horizontal SIA velocity, $\vec{u}$, and the horizontal SStA velocity, $\vec{v}$. For each scheme, individual velocity solutions from the shallow approximations are calculated independently. It is important to note that SStA velocities in grounded ice regions include basal drag. This implies a major difference from SSA velocities computed in the ice shelf sectors, for which the friction at the ice–ocean interface is negligible.

For consistency, the basal drag term that enters the SStA equations is computed using

Table 2.2: Summary of the hybrid schemes implemented in this study.

Scheme	Basal sliding	Reference in text	References
HS-1	Weertman-type sliding	Eq. (2.8)	This study
HS-2a	SStA velocities	Eq. (2.10)	Bueler and Brown (2009)
HS-2b	Weertman-type sliding	Eq. (2.11)	This study
HS-3	SStA velocities	Eq. (2.12)	Winkelmann et al. (2011)

the same sliding law as described in Section 2.2.1 (Eq. 2.2), in the form

$$\vec{\tau}_{\mathrm{b}} = -\beta_{\mathrm{drag}}\vec{v}_{\mathrm{b}}, \tag{2.5}$$

where $\vec{v}_{\mathrm{b}}$ is the basal SStA velocity and the drag coefficient, β_{drag}, is computed as

$$\beta_{\mathrm{drag}} = \frac{N_{\mathrm{b}}^{\frac{q}{p}}}{C_{\mathrm{b}}^{\frac{1}{p}}} \left(\frac{1}{\sqrt{v_{\mathrm{b}_x}^2 + v_{\mathrm{b}_y}^2 + v_0^2}} \right)^{1-\frac{1}{p}}. \tag{2.6}$$

Here, v_{b_x} and v_{b_y} are the horizontal components of the SStA velocity at the ice base, and $v_0 = 0.01\,\mathrm{m\,a}^{-1}$ is a small regularisation quantity introduced to prevent singularities at the locations where there is no basal sliding (Bueler and Brown, 2009).

The first hybrid scheme (henceforth HS-1) is the original implementation in SICOPOLIS v3.2-dev (revision 619) based on the slip ratio of grounded ice, computed as

$$r = \frac{|\vec{u}_{\mathrm{b}}|}{|\vec{u}_{\mathrm{s}}|}, \tag{2.7}$$

where $\vec{u}_{\mathrm{b}}$ is the Weertman sliding velocity (Eq. 2.2) and $\vec{u}_{\mathrm{s}}$ is the surface SIA velocity. At each iteration, and for each velocity component, the local slip ratio r is compared to a prescribed threshold r_{thr} ranging from 0 to 1 (Section 2.4). If r is larger than the threshold, the grid point is flagged as streaming ice where the SStA velocities should be computed. Once SStA velocities are computed, the individual contributions of the SIA and SStA velocities at each streaming grid point are determined using the weight

$$w(r) = \frac{r - r_{\mathrm{thr}}}{1 - r_{\mathrm{thr}}}. \tag{2.8}$$

Then, for each streaming grid point, the hybrid horizontal velocity $\vec{U}$ is computed as

$$\vec{U} = w \cdot \vec{v} + (1 - w) \cdot \vec{u}, \tag{2.9}$$

recalling that $\vec{u}$ and $\vec{v}$ are the horizontal SIA and SStA velocities, respectively.

The second approach (henceforth HS-2) is based on the idea by Bueler and Brown (2009), in which SStA velocities are calculated over the entire ice sheet and used as a sliding velocity complementing a non-sliding SIA model. SIA and SStA velocities are combined as in Eq. (2.9), and the weighting function is adopted from Bueler and Brown (2009, Eq. 22):

$$w\left(|\vec{v}|\right) = \frac{2}{\pi}\arctan\left(\frac{|\vec{v}|^2}{v_{\text{ref}}^2}\right), \tag{2.10}$$

where v_{ref} is a reference ice velocity (Section 2.4). The velocity v_{ref} marks the point for which the SIA and SStA contributions are equally weighted; i.e. the resulting hybrid velocity is a standard mean of both solutions. The weighting function is smooth and monotone, and its value converges towards 0 for small velocities and towards 1 when $\vec{v}$ is large compared to the reference velocity v_{ref}. As in the HS-1, w is used to compute respective contributions from the SIA and SStA, with the difference that Eq. (2.10) uses v_{ref} as the only criterion to determine the SStA contribution. The SStA velocities are calculated over the entire ice sheet, and an a priori identification of fast flow zones is not required.

As described in Section 2.2.1, the SIA solution in SICOPOLIS is computed using the Weertman sliding law (Eq. 2.2) as a boundary condition. To assess the influence of a SIA solution including the Weertman sliding, we have split this hybrid scheme into two: a sub-scheme (HS-2a) that replicates the idea of Bueler and Brown (2009) with no basal velocity prescribed in the computation of the SIA and a sub scheme (HS-2b) that has a Weertman sliding component and uses it to compute a slightly modified weight.

$$w\left(|\vec{u}_{\text{b}}|\right) = \frac{2}{\pi}\arctan\left(\frac{|\vec{u}_{\text{b}}|^2}{v_{\text{ref}}^2}\right), \tag{2.11}$$

where $\vec{u}_{\text{b}}$ is the basal sliding velocity as in Eq. (2.2). Thus, in the HS-2b the SStA solution does not serve as a replacement of a sliding law. It is rather used to determine to what extent the computed SStA velocity should replace the basal velocity used to compute the

SIA solution. The third approach (henceforth HS-3) simply adds up the non-sliding SIA and SStA solutions:

$$\vec{U} = \vec{u} + \vec{v}. \tag{2.12}$$

This superposition of approximations has been employed in recent studies using SIA models in combination with a SStA solution as a sliding law (e.g., Winkelmann et al., 2011). It bypasses the need for additional free parameters, such as r_{thr} and v_{ref} in the HS-1 and HS-2, respectively. This approach is based on the assumption that on ice shelves the SIA contribution is negligible due to low surface gradients, and therefore the modelled ice flow is dominated by the SStA solution, whereas in the continental interior the modelled ice flow is dominated by the SIA solution (Winkelmann et al., 2011). Since the SIA and SStA solutions are computed over the entire domain, their superposition enables a smooth transition across different flow regimes, ranging from slow ice motion in the interior to a characteristic fast flow of ice shelves, thereby allowing for stress transmission across the grounding line. As in the HS-2, an identification of fast flowing zones is purely diagnostic and not required during the computation of $\vec{U}$. Table 2.2 presents a summary of the hybrid schemes applied in this study.

### 2.2.3   Calibration of basal sliding coefficients

We have implemented an iterative method following Pollard and DeConto (2012b) in order to determine the distribution of sliding coefficients C_0 that minimises the difference between the modelled and observed ice thickness. The method starts from a spatially uniform guess value for the distribution of C_0 and runs the model forward in time, as described in Section 2.4. At a given time step, Δt_{inv}, the method uses the basal temperature below the pressure-melting point, T_{m}, to identify grounded grid points where basal sliding may occur. If the absolute value of T_{m} is smaller than the parameter γ from Eq. (2.4), i.e. close to the pressure-melting point, the method computes the difference between the modelled and observed ice thickness, which is then used to locally adjust C_0 at this grid point according to

$$C_0^* = C_0 10^{\Delta H}, \tag{2.13}$$

where C_0^* is an updated sliding coefficient and $\Delta H = (H - H_{\text{obs}})/H_{\text{inv}}$. Here, ΔH is the difference between the modelled and observed ice thickness, scaled by a factor, H_{inv}, in order to prevent overshoots. For the same reason and following the implementation by Pollard and DeConto (2012b), variations in the value of the multiplicative factor $10^{\Delta H}$ are further limited by a range of ~ 0.03 to 30. In contrast to previous studies using SICOPOLIS where $\gamma = 1\,\text{K}$, here we set this parameter to a value of $3\,\text{K}$, allowing for a more frequent calibration of the sliding coefficients (Pollard and DeConto, 2012b).

Studies using this iterative technique and inversion methods have shown that potential distributions of sliding coefficients C_0 are highly heterogeneous, with values spanning several orders of magnitude (e.g., Pollard and DeConto, 2012b; Arthern et al., 2015). To ensure numerical stability, we limit our inferred values to a range of 1 to $10^5\,\text{m}\,\text{yr}^{-1}\,\text{Pa}^{-1}$ during the calibration procedure. Additionally, we have implemented the following condition: when the computed surface ice velocity reaches an ancillary speed limit at a certain grid point, the adjustment of C_0 for that point is halted. This prevents the method from over-adjusting the sliding coefficients when the velocity limit has been reached and no noticeable changes occur in response to further adjustments of C_0. This additional constraint is applied in order to ensure numerical stability and keep the modelled ice velocities within the range of observations. For the experiments presented in this study, the lower speed limit is defined as $0.1\,\text{m}\,\text{a}^{-1}$, whereas the upper limit is set to $4000\,\text{m}\,\text{a}^{-1}$. These values are based on the observed surface velocities of Rignot et al. (2011).

The iterative technique involves an additional limiting condition that prevents over-adjustments of C_0. For each individual grid point, if the difference between the modelled and observed ice thickness reduced at the previous time step, the adjustment at the current time step is deactivated. This allows previous adjustments to fully develop their effects over the following time steps and prevents the technique from adding unnecessary extra adjustments that often result in overshoots. The calibration is activated again as soon as the time derivative of the modelled ice thickness drops to zero (i.e. the difference between the modelled and observed ice thickness is not reduced anymore) or the misfit starts increasing (e.g., due to increased influx from surrounding areas). Our experiments have shown that this additional feature enables the use of a smaller Δt_{inv} (50 years used here compared to 500–10 000 years in Pollard and DeConto, 2012b) because further adjustments will only be applied when and where strictly necessary. A further benefit is that it indirectly allows non-local adjustments of C_0 to influence the local ice dynamics: if an adjustment
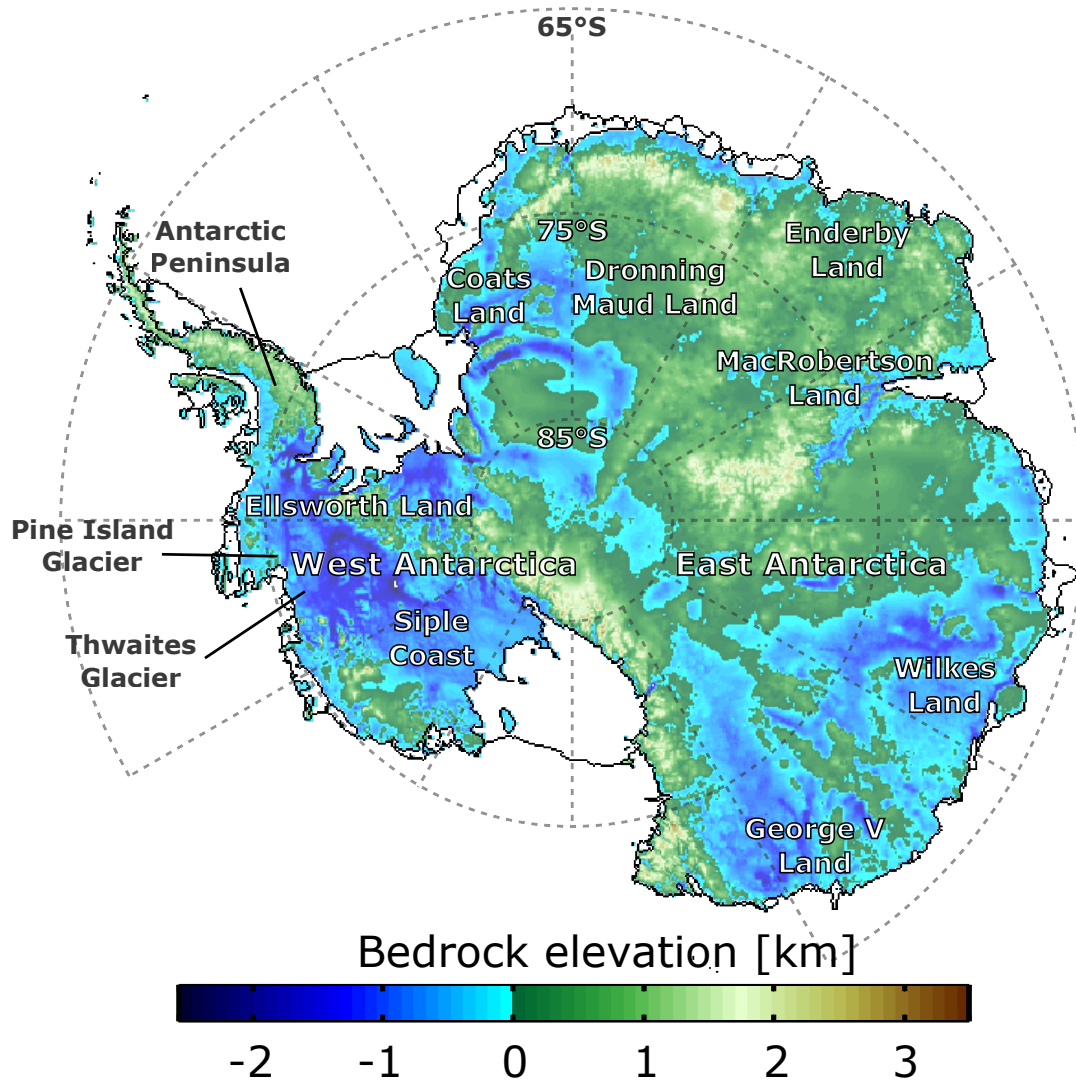
Figure 2.1: A bedrock elevation map of Antarctica obtained from the BEDMAP2 data set (Fretwell et al., 2013), including the location of the sites mentioned in the text.

applied in the vicinity of a grid point reduces the misfit, further adjustments at this grid point will still be halted.

2.3 Data sets

The calibration procedure takes advantage of the improved quality of the modern, continental-scale Antarctic data sets, such as climatic forcing (van Wessem et al., 2014) and topography (Fretwell et al., 2013). The forcing data serve as time-invariant boundary conditions for our equilibrium (steady-state) model simulations. It should be noted that the modern AIS is unlikely in a steady state and a transient simulation, e.g., of the entire

last glacial cycle, would provide a more realistic scenario for the calibration procedure. However, existing reconstructions of the Antarctic palaeoclimate and past ice-sheet configurations still contain large uncertainties, with in situ data being sparse in space and time. Keeping this in mind, we think that using modern data sets and assuming equilibrium conditions is a valuable first-order approximation to a more complex model calibration. Furthermore, such equilibrium set-up can serve as an initial guess for transient deglaciation simulations, which include time-dependent processes not considered here (Fyke et al., 2014).

Initial modern conditions for surface topography, ice shelf thickness, and bedrock elevations relative to the present-day sea level are derived from the BEDMAP2 data set (Fretwell et al., 2013). BEDMAP2 is a compilation of 24.8 million ice thickness data points obtained from a variety of sources including airborne and over-snow radar surveys, satellite altimetry, seismic sounding data, and satellite gravimetry (Fretwell et al., 2013). This compilation is complemented by surface elevation data from several digital elevation models to derive previously unknown bedrock features and allows for a detailed modelling of the AIS. Figure 2.1 shows the bedrock topography data from BEDMAP2, together with the locations mentioned in the text. The main sources of uncertainty in the ice thickness and bedrock elevation maps are the errors in surface digital elevation models and ice thickness measurements, as well as the applied regridding, which produce overall uncertainties ranging from 59 m across areas with smooth landscapes to 1000 m in regions where only gravimetric data are available (e.g., south of Coats Land).

At the base of the thermal bedrock, geothermal heat flux is prescribed according to the map of Shapiro and Ritzwoller (2004). This map is derived from a global seismic model of the upper mantle and the crust assuming a relation between seismic velocities and mantle temperatures and uses observations from regions with similar structures to infer heat-flow probability distributions where such observations are scarce or non-existent. In the inferred heat-flux map, West Antarctica is characterised by an average heat flow that is nearly three times higher than in East Antarctica. Although the resulting map depends on the accuracy of available observations as well as on the choice of the seismic model and similarity functional, the inferred distributions are robust to internal parameter changes, especially for continental areas such as Antarctica (Shapiro and Ritzwoller, 2004). However, the method cannot reproduce small-scale patterns caused by local variations in crustal heat production, which may exert an important control on the dynamics of the

Antarctic ice streams.

Boundary conditions at the surface include Antarctic precipitation rates and near-surface air temperature model output from the regional climate model RACMO2.3 (van Wessem et al., 2014), averaged over the period of 1979 to 2010. RACMO is forced at its boundaries by the reanalysis data from ERA-Interim (Dee et al., 2011). In the interior of the domain the Antarctic climate conditions are modelled with a horizontal resolution of 27 km and 40 levels in the vertical direction. RACMO contains modules that are specifically developed for glaciated regions, including a multilayer snow model. The model output from RACMO compares well with 3234 in situ observations of surface mass balance used for its validation, displaying a correlation of $r^2 = 0.77$ and a particularly good fit for the dry East Antarctic plateau (van Wessem et al., 2014).

A simple lapse-rate correction of $0.008\,°\mathrm{C}\,\mathrm{m}^{-1}$ is used to account for the discrepancies between the modelled and observed surface elevations. Surface melt is computed with a positive degree-day (PDD) scheme (Reeh, 1991; Calov and Greve, 2005) using the factors $\alpha_\mathrm{ice} = 8\,\mathrm{mm}\,\mathrm{d}^{-1}\,°\mathrm{C}^{-1}$ and $\alpha_\mathrm{snow} = 3\,\mathrm{mm}\,\mathrm{d}^{-1}\,°\mathrm{C}^{-1}$ (ice equivalent) for ice and snow, respectively (Ritz et al., 2001), and a standard deviation of $\alpha_\mathrm{std} = 5\,°\mathrm{C}$ for the statistical fluctuations in air temperature.

All input fields are projected onto a regular, rectangular, polar stereographic grid covering the entire Antarctic continent and the surrounding Southern Ocean, with a nominal horizontal resolution of 20 km, corresponding to 301×301 grid points. Our choice of resolution has been motivated by the large number of experiments presented in Section 2.5, each spanning 400 000 years, and the fact that Pollard and DeConto (2012b) have shown that the results remain essentially unchanged when the horizontal resolution is increased to 10 km (in a nested simulation), even in rapidly flowing sectors. However, our initial tests with a model resolution of 40, 20, and 10 km have identified areas where the modelled ice flow is more sensitive to the resolution used (see the Supplement). These mainly occur close to the ice-sheet margins where the grounding zone of a glacier is often represented by only one grid cell at lower resolution. In such regions the use of a finer grid allows for a more detailed treatment of the topographically constrained glacial flow. In the context of this comparison study, however, these limitations equally affect the performance of all hybrid schemes and do not impact our conclusions. In the vertical direction, ice columns consist of 91 layers (11 equidistant grid points for temperate ice and 81 grid points for "cold" ice densifying towards the base, sharing the grid point at their interface),

mapped to a $[0, 1]$ interval using a σ transformation (Greve and Blatter, 2009).

2.4 Experimental set-up

The modified version of SICOPOLIS described in Section 2.2 is applied to the entire AIS and the fringing ice shelves. The experiments performed during the calibration of the ice sheet–shelf system aim at quantifying the differences and similarities between the hybrid approaches. Default values for the parameters of the hybrid schemes are $r_{thr} = 0.5$ (HS-1) and $v_{ref} = 100 \, \mathrm{m\,yr^{-1}}$ (HS-2a and HS-2b). As mentioned in Section 2.2.2, the HS-3 does not include any free parameters. Additionally, and for comparison purposes, the same experiments are performed using a SIA-only scheme for grounded ice (henceforth SoS).

The bulk of the calibration consists of an iterative technique used to derive the distribution of sliding coefficients C_0 (Section 2.2.3) that exerts a dominant control on the resulting ice distribution and its fit to observations. The calibration procedure starts from a homogeneous guess value of $C_0 = 1 \, \mathrm{m\,yr^{-1}\,Pa^{-1}}$, which is the lower limit of the considered range (see Section 2.2.3). The time steps between adjustments and the scaling factor in Eq. (2.13) are set to $\Delta t_{inv} = 50$ years and $H_{inv} = 5000 \, \mathrm{m}$, respectively. We follow the method by Pollard and DeConto (2012b) and allow for a free evolution of both the ice sheet and ice shelf thickness, but their interface (the grounding line) is kept at its present-day observed position. Free evolution is needed because the calibration of the sliding coefficients requires an evolving ice thickness that will be routinely compared to observations. The reasons for a constrained grounding line are twofold: this approach (1) enables a comparison with observations in coastal regions during the calibration and (2) prevents artificial transitions between grounded and floating areas caused by equally artificial effects of unrealistic initial thermal regimes and C_0 distributions that evolve from initial guess values. Our tests show that such artefacts can produce feedbacks that are difficult or impossible to reverse. For the same reason, glacial isostatic adjustment is not included in the simulations, and ice shelf fronts are constrained to the observed locations. As mentioned above, the ice shelf thickness is allowed to evolve, but basal melt rates are adjusted at each time step in order to keep the modelled ice shelves as close as possible to observations. This ensures a consistent computation of mass fluxes across all flow regimes and does not overlap with the calibration of sliding coefficients, since these are not applied in floating ice sectors.

In this study, the calibration procedure is divided into four steps. In the first three steps, a relaxation scheme is applied to the evolution of the modelled ice thickness, H. Here, the difference between the current solution of the ice thickness equations, H_{new}, and the solution from the previous time step, H_{old}, is scaled at every time step by a factor h_{rlx} ranging between 0 and 1, as follows:

$$H = H_{\text{old}} + h_{\text{rlx}} \left(H_{\text{new}} - H_{\text{old}} \right). \tag{2.14}$$

For a time-invariant forcing, our tests have shown that different values of h_{rlx} will result in very similar equilibrium states. The relaxation simply delays the time point at which this state is reached. However, such relaxation procedure allows for bigger time steps at which the topography evolution is computed, without affecting the internal temperature evolution. In this way, an equilibrium with the boundary conditions will be reached faster by the temperature field than by the topography. This effectively minimises transient effects in the closely associated ice thickness and velocity fields, especially at the beginning of the calibration runs when model parameters follow the initial guess values. More importantly, it allows us to simultaneously apply the iterative calibration technique described in Section 2.2.3, in contrast to approaches in which the topography is fixed (e.g., Sato and Greve, 2012). This ensures that the modelled ice thickness distribution has the closest possible match to the initial observed distribution throughout the initial calibration stages. The value of the relaxation factor is set to $h_{\text{rlx}} = 0.001$ in the first stage of the calibration driven over a simulation time of $100\,000$ years ($100\,\text{kyr}$), using a time step of 5 years. The following second and third stages replicate the first one, but with larger scaling factors of $h_{\text{rlx}} = 0.01$ and $h_{\text{rlx}} = 0.1$, respectively, for an additional simulation time of $100\,\text{kyr}$ in each stage. In the final stage, the relaxation is deactivated and a smaller time step of 1 year is applied over an additional simulation time of $100\,\text{kyr}$, which provides a long enough time span to attain a dynamic equilibrium.

2.5   Results and discussion

In this chapter we present an ensemble of simulations of the AIS that aim to comprehensively evaluate different hybrid schemes combining the SIA and SStA. Our evaluation uses the degree of agreement between the modelled and observed ice-sheet geometries and surface velocities as a measure of their performance, allowing for a point-by-point quantification

of the model errors.

Keeping in mind that each hybrid scheme builds upon the SIA solution, partially or entirely replacing it at variable locations with the SStA solution, we have also included the results from the SIA-only scheme in our comparison. In particular, this enables a qualitative separation of relative contributions of the SIA and SStA, providing a new insight into the internal differences between the schemes and their applicability to ice-sheet areas with diverse dynamical characteristics.

By applying an automated model calibration against the observed ice thickness to each of the hybrid schemes we infer spatial distributions of poorly constrained sliding coefficients as a proxy for mechanical conditions at the ice–bedrock interface and assess their sensitivity to the choice of a particular hybrid scheme. In addition, the influence of variations in the parameters controlling relative contributions of SIA and SStA velocities in each scheme is assessed for a wide range of parameter values.

2.5.1 Comparison of equilibrium states

As described in Section 2.3, our experiments use the BEDMAP2 observational data set (Fretwell et al., 2013) as an initial ice-sheet configuration, running the model forward in time under a relaxation scheme (Eq. 2.14) until the temperature distribution within the ice sheet reaches an equilibrium state. After this initialisation, the relaxation is deactivated and the model runs until a full thermal and dynamic equilibria are attained. The equilibrium is defined as the point in time in which the variations of the total grounded ice volume over a prolonged time ($> 10\,000$ years) are smaller than $0.01\,\%$.

Starting from the initialised states after a $300\,000$-year relaxation procedure, the time required to reach an equilibrium varies from scheme to scheme (Figure 2.2). The HS-1, HS-2a, and HS-3 attain a virtually invariable state after only $20\,\mathrm{kyr}$, as opposed to the SoS and HS-2b that display significant oscillations in the total volume around a mean equilibrium value even after a period of $100\,\mathrm{kyr}$, suggesting unstable equilibrium states. Compared to the SoS, the computation of SStA velocities in the grounded ice sectors requires an extra computational effort for each iteration in the numerical solvers, with the computing time increasing by a factor of ~ 4 for the applied hybrid schemes. The characteristic computing time of the HS-1 is somewhat shorter than that of the other hybrid schemes (but still longer than for the SoS) due to the prognostic identification of ice streams that obviates the need for the computation of SStA velocities over the entire
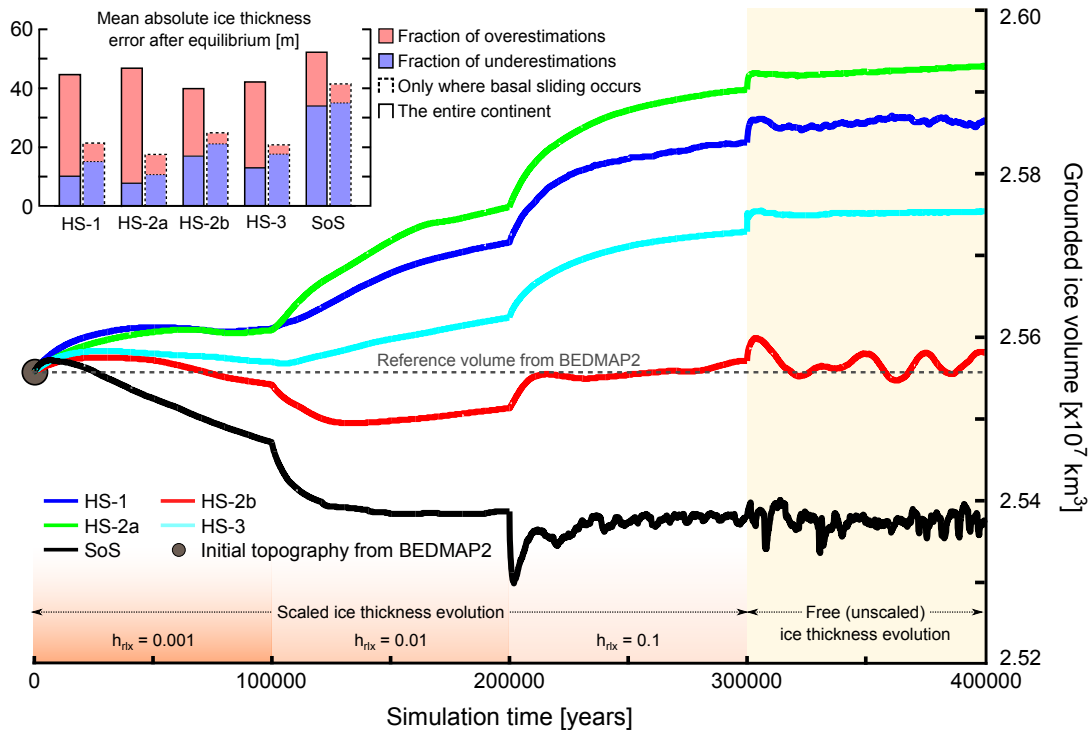
Figure 2.2: Overview of the calibration procedure. Main: the evolution of the total grounded ice volume during the calibration procedure, in $\times 10^7 \, \mathrm{km}^3$. At the end of each $100,000$-year-long stage, the relaxation coefficient h_{rlx} increases by 1 order of magnitude, from 0.001 to 1 (free evolution), until a dynamic equilibrium is attained. Inset: mean absolute differences between the modelled and observed ice thickness at the end of the simulations, in metres. For each scheme, a mean absolute error is calculated for the entire ice sheet (left bars) and separately over the areas where basal sliding is identified (right bars). Fractions of the mean absolute error arising from under- and overestimations are shown in blue and pink, respectively.

ice sheet. However, we have observed that the iterative solvers in the model require a substantially smaller number of iterations when the hybrid schemes are used, making them numerically more stable compared to the SoS.

The calibration procedure applied to all schemes yields total grounded ice volumes which are in a close agreement with the reference value of $\sim 2.56 \times 10^7 \, \mathrm{km}^3$ from the observational data (Fretwell et al., 2013), with the maximum deviation being below 1.5 %. Individual values of the modelled ice volumes and their respective deviations for most of our experiments are summarised in Table 2.3. The best fit to observations is obtained using the HS-2b, which corresponds to an overestimation of the total grounded ice volume by 0.1 %. The other schemes produce relatively larger misfits, with the HS-2a simulation yielding the greatest deviation of 1.46 % arising from an overestimation of the total ice volume. The smallest ice sheet is produced by the SoS that underestimates the total grounded ice volume by 0.72 %.
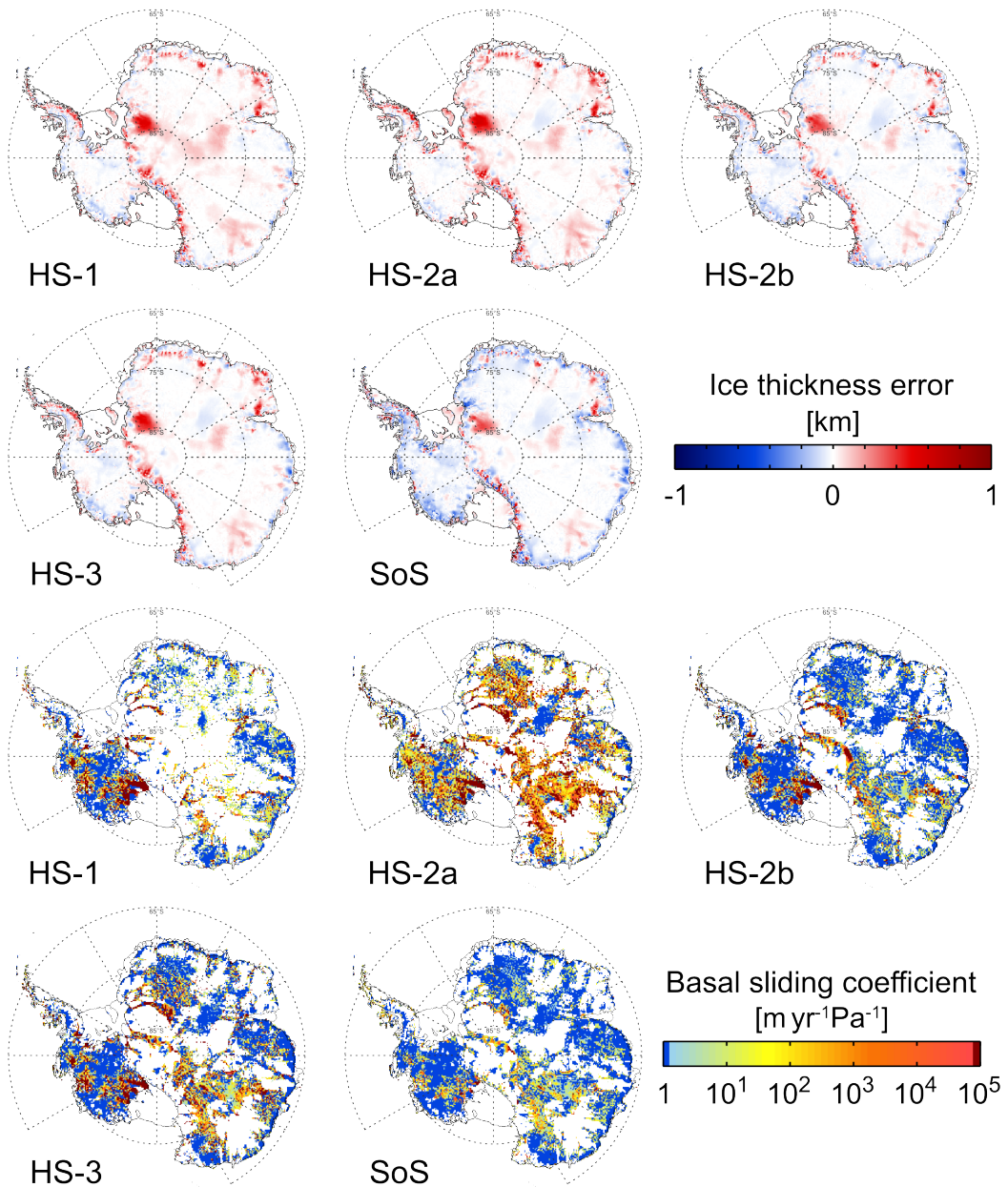
Figure 2.3: Comparison of the ice-sheet states derived from different schemes at the end of equilibrium simulations. Left column: differences between the modelled and observed ice thickness, in metres. Right column: inferred distributions of basal sliding coefficients, in $\mathrm{m\,yr^{-1}\,Pa^{-1}}$. Non-coloured areas mark the locations where basal sliding is not identified and the calibration procedure does not operate. Colour-code saturates at the upper and lower limits allowed for the calibration procedure.

The inset of Figure 2.2 shows the total ice thickness errors for all schemes. The errors are computed as an average of the absolute misfit values in all grounded grid points and remain below $50\,\mathrm{m}$ for all hybrid schemes (Table 2.3). Among these, the largest average error of $46.6\,\mathrm{m}$ is produced by the HS-2a, while the smallest error of $40.0\,\mathrm{m}$ is obtained using the HS-2b. For the former, $83\,\%$ of the misfit is due to overestimations of ice thickness, while

Table 2.3: Summary of the results at the end of the calibration procedure for each of the applied hybrid schemes (HS, see Section 2.2.2) and SIA-only scheme (SoS), including the total grounded ice volume V_{grd} (km^3); a deviation from the total grounded ice volume, ΔV_{grd} (%); a mean absolute error in the ice thickness, $\overline{\Delta H}$ (m); a fraction of the total area where basal sliding occurs, A_{sld} (%); a mean ice thickness error only where basal sliding operates, $\overline{\Delta}_{\mathrm{sld}} H$ (m); a mean surface velocity error, $\overline{\Delta} v_{\mathrm{s}}$ (m yr^{-1}); a fraction of the grounded ice area dominated by the SIA (only where $w < 0.25$), $A_{\mathrm{SIA}_{0.25}}$ (%); and a fraction of the grounded ice area dominated by the SStA (only where $w > 0.75$), $A_{\mathrm{SStA}_{0.75}}$ (%).

Scheme	V_{grd} (km^3)	ΔV_{grd} (%)	$\overline{\Delta H}$ (m)	A_{sld} (%)	$\overline{\Delta}_{\mathrm{sld}} H$ (m)	$\overline{\Delta} v_{\mathrm{s}}$ (m yr^{-1})	$A_{\mathrm{SIA}_{0.25}}$ (%)	$A_{\mathrm{SStA}_{0.75}}$ (%)
HS-1	2.58×10^7	$+1.20$	44.6	45.2	20.8	29.7	47.9	29.4
HS-2a	2.59×10^7	$+1.46$	46.6	54.2	17.6	17.6	82.0	2.4
HS-2b	2.56×10^7	$+0.10$	40.0	62.0	25.4	16.0	82.3	8.5
HS-3	2.57×10^7	$+0.77$	42.6	58.7	22.3	23.2	–	–
SoS	2.53×10^7	-0.72	52.4	58.9	41.3	55.3	100	0

the latter shows nearly even contributions from under- and overestimations. This is in accordance with the results shown in Figure 2.2, where the misfits obtained from the two schemes using the SStA as a sliding law are dominated by an excessive ice thickness. The hybrid schemes that include a Weertman basal sliding component during the computation of SIA velocities are not necessarily dominated by underestimations of the ice thickness. For example, less than a quarter of the misfit produced by the HS-1 can be attributed to areas with an ice thickness deficit. For comparison, the averaged absolute error produced by the SoS is 52.4 m, with 65 % of the misfit coming from an underestimation of the ice thickness.

The results depicted in Figure 2.2 reflect only a time-dependent, continental-scale information about the fit between the modelled and observed ice-sheet geometries, providing no insights into local model performance. In order to have a more detailed overview of the results, Figure 2.3 (left column) shows the corresponding spatial maps of ice thickness errors. All schemes provide a reasonably good fit to the observational data in the continental interior, with larger discrepancies mainly occurring at the ice-sheet margin. It can be readily observed that the modelled ice sheet is too thick over mountainous regions and across the region between the Shackleton Range and the Pensacola Mountains (south of Coats Land), which has some of the largest uncertainties in the topographic data (Fretwell et al., 2013). These are common features for all schemes, regardless of the approach chosen for the sliding component, and could originate from insufficient geothermal flux, too high precipitation rates, and/or an unrealistic smoothness of the bedrock in this area that prevents the formation of topographically driven ice streams. The distribution of
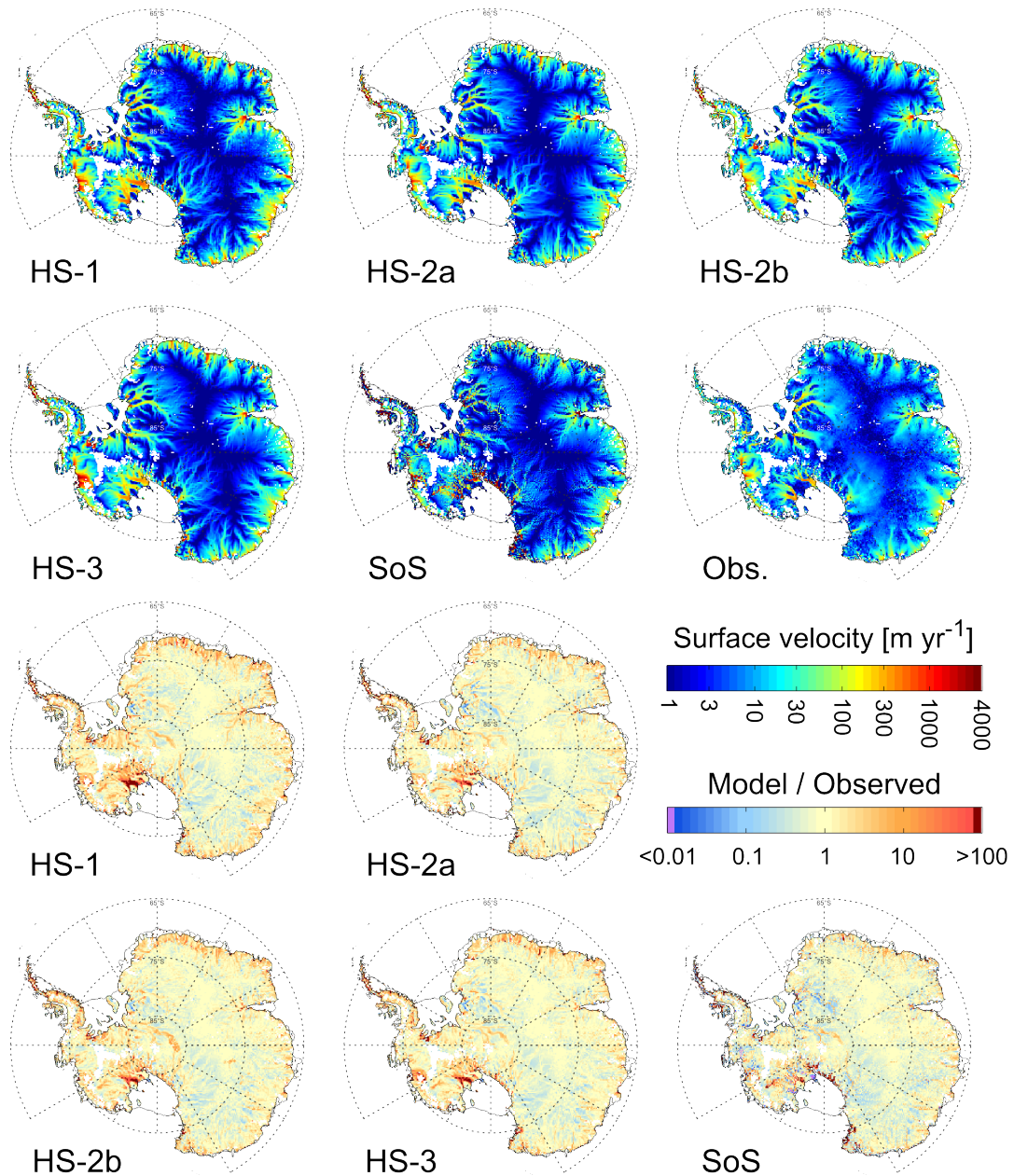
Figure 2.4: Left column: equilibrium surface velocities across the grounded ice areas derived from different schemes, in $\mathrm{m\,yr^{-1}}$, compared to the observational data set from Rignot et al. (2011) (bottom), regridded to the model resolution of $20\,\mathrm{km}$. Right column: ratios of the modelled to observed surface velocities, plotted on a logarithmic scale. Velocities smaller than $2\,\mathrm{m\,yr^{-1}}$ are excluded. Colour-code saturates at ratios larger than 100 or smaller than 0.01.

zones where the modelled basal temperatures are far below the pressure-melting point are depicted as white-coloured areas in Figure 2.3 (right column). In general, these areas coincide with the locations where the largest ice thickness errors occur. Areas where the ice thickness is underestimated are mainly located at and around the ice margins. In many of these areas, however, sliding is identified and the calibration of C_0 reaches its

lower limit, implying that the surface mass input is insufficient to minimise the misfit. The SoS produces too thin ice along most of the ice-sheet margin, which explains the high percentage of the ice thickness errors arising from underestimations (inset of Figure 2.2). In contrast, the hybrid schemes produce error patterns that differ only slightly between each other. The only exception is the HS-2b, which is closest to the SoS, albeit exhibiting smaller underestimations at the ice-sheet margins.

Furthermore, we evaluate the performance of the calibration procedure over the areas where basal sliding is identified and the calibration is applied. For this purpose we have calculated averaged absolute errors in the ice thickness across regions where basal sliding operates (inset of Figure 2.2). It should be kept in mind that the calibration procedure also affects the ice masses located in the immediate proximity to sliding areas through surface elevation gradients and/or stress transmission. Mean ice thickness errors over the sliding areas are smaller than those estimated for the whole ice sheet, although the degree of relative improvement varies from scheme to scheme (Table 2.3). For example, the misfit produced by the SoS decreases by only $\sim 20\%$ if calculated over the sliding ice-sheet sectors, while more than 60% of the errors resulting from the HS-2a occur over the areas where no sliding is identified and C_0 is not calibrated. For all hybrid schemes, the percentage of the errors associated with an underestimation of the ice thickness increases substantially when their performance is assessed across areas where basal sliding coefficients are calibrated. This supports the observation that the modelled ice is excessively thick in regions where C_0 is not calibrated.

The inferred distributions of C_0 are shown in Figure 2.3 (right column). In general, the areas where the calibration is performed are similar for all schemes (Table 2.3), although there is a significant spread in the retrieved values. The HS-1 scheme predicts a minimum corresponding to 45% of the total grounded ice area, contrasted by higher percentages for the other schemes ranging between 54 and 62%. The upper limit of $10^5\,\mathrm{m\,yr^{-1}\,Pa^{-1}}$ for the sliding coefficient is reached by all schemes across up to 18% of the ice-covered land, with their highest concentration occurring in the Siple Coast region, where ice streams flow rapidly over a smooth and deformable bed provided by strong lubrication from water saturated subglacial sediments (e.g., Blankenship et al., 1986; Alley et al., 1987; Kamb, 2001). The upper limit is also reached in Coats, MacRobertson, and Ellsworth lands (Figure 2.1). Similarly, all calibration runs estimate the C_0 value to reach its lower limit of $1\,\mathrm{m\,yr^{-1}\,Pa^{-1}}$ over ~ 10 to $\sim 32\%$ of the ice-sheet-covered area. The SoS and

HS-2b infer this value throughout most of the West AIS and over vast parts of the East AIS, particularly at the ice margins. Its incidence is relatively lower for the other hybrid schemes, especially for the HS-1 and HS-2a. Quantitatively, the good agreement between the inferred coefficient distributions is mainly restricted to the areas where C_0 reaches an upper or lower limit. In other areas the values generally vary across orders of magnitude.

Direct comparison of our results to those from Pollard and DeConto (2012b) is hindered by the differences in the sliding laws and hybrid schemes. Nevertheless, we have found a good qualitative agreement in the inferred distributions of C_0, with similar patterns of high vs. low values. For instance, both studies identify the Siple Coast and Coats Land regions as areas where the ice streaming flow is driven by basal conditions favourable for sliding. A similar agreement is found for the Thwaites and Pine Island Glacier areas, as well as in the MacRobertson Land (Figure 2.1). Low values of C_0 are predicted in the continental interior of West Antarctica and over most of the East AIS.

2.5.2   Analysis of the SIA and SStA contributions

As described in Section 2.2.2, different hybrid approaches are not expected to produce exactly the same equilibrated ice velocity fields. We demonstrate this in Figure 2.4, where the modelled steady-state surface velocities derived from the SoS and the hybrid schemes are compared to a continental-scale observational data set (Rignot et al., 2011). This high-resolution (900 m) data set contains many small-scale features that are unresolved by the model due to its lower resolution. Nevertheless, all schemes are able to reproduce the observed range of ice flow velocities, distinguishing between the ice-sheet areas with low velocities near the ice divides and fast flowing ice streams reaching the ice-sheet margins. In the transition zones between the continental interior and the ice-sheet margins, all schemes reproduce to some extent the fast flowing ice streams identified by observations. However, in contrast to the results from the hybrid schemes, surface ice velocities derived from the SoS are characterised with noise-like patterns, which are especially visible in the areas of rapid ice flow. We attribute these artefacts to a combination of lacking stress transmission in the SIA, which allows for steep gradients in the modelled velocities, and the calibration procedure, which can potentially amplify these gradients through local adjustments of C_0.

Although the overall character of the observed surface ice velocities is qualitatively well reproduced by all the hybrid schemes, modelled ice flow is clearly too fast at and around
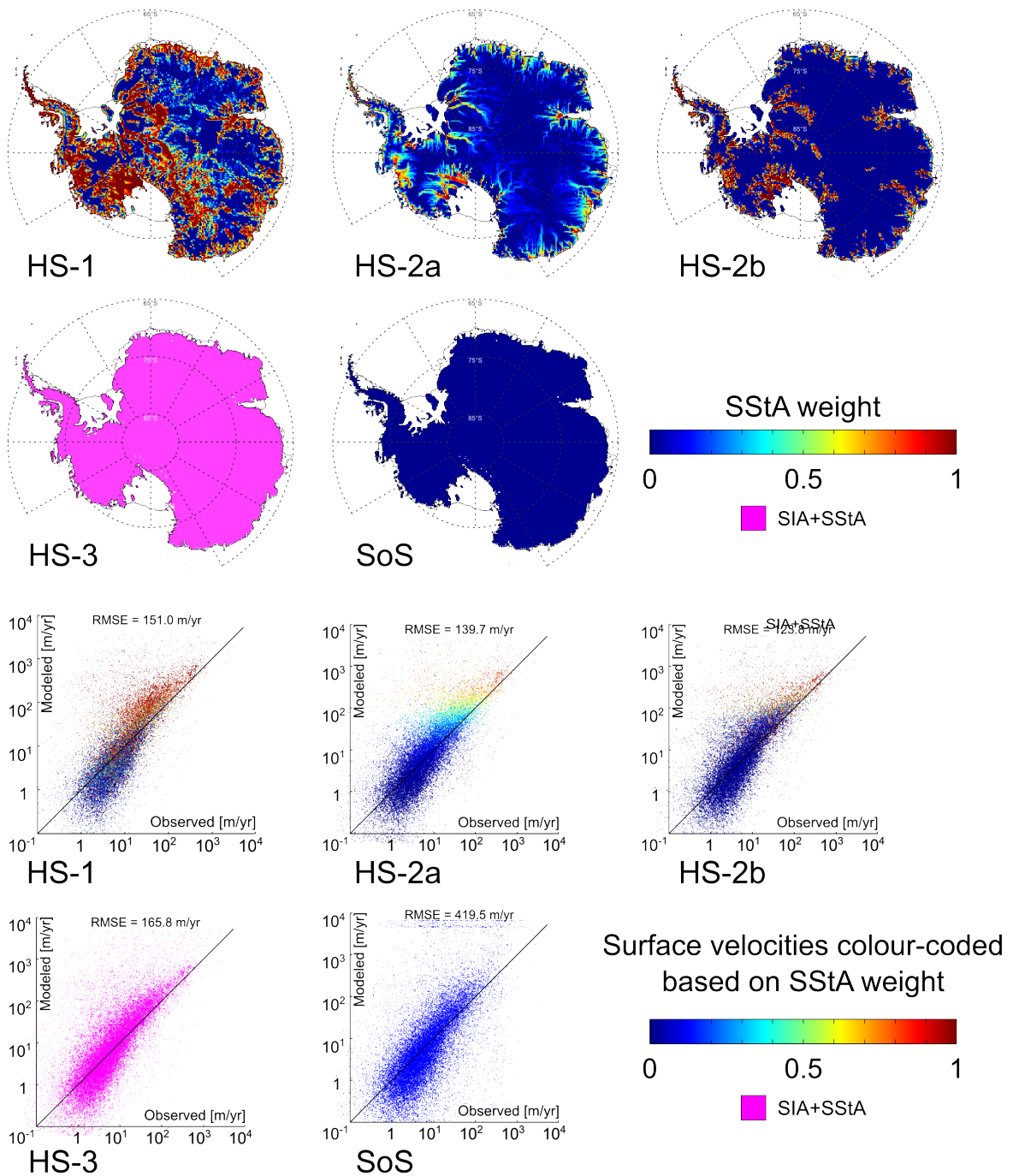
Figure 2.5: Left column: equilibrium SStA weights derived from different schemes. The HS-3 does not use a weighting function and simply adds velocities derived from both shallow approximations. Right column: scatter plots of modelled vs. observed surface velocities, in $m\,yr^{-1}$. Each point is colour-coded according to the corresponding SStA weight.

several ice stream locations, such as at the Siple Coast. Furthermore, modelled surface velocities are generally overestimated close to the grounding lines of most outlet glaciers, in particular due to the resolution-related limitations discussed in Section 2.3. These overestimations are particularly large in the SoS simulation, even though the discrepancies

between the modelled and observed ice thickness are small (Figure 2.3, left column). Overestimations of the ice flow velocity by the hybrid schemes at the grounding zone are smaller than those derived from the SoS simulation, but they cover a wider area and reach further upstream. Similar observations have been made by Pollard and DeConto (2012b) using a different hybrid ice sheet–shelf model and a different set of topographic ice observations and external forcing. They proposed that the overestimation of surface velocities in these areas may be caused by a coarse model resolution, exaggerated snowfall rates, or an excessive internal deformation compared to sliding near the ice margins.

In order to quantitatively evaluate the model fit to observations, we have calculated point-by-point ratios between the modelled and observed surface velocities (Figure 2.4, right column). As mentioned above, the modelled velocities are in a good agreement with observations in the continental interior characterised by slow ice motion. In contrast, at the margins the ice velocity simulated by the hybrid schemes sometimes reaches values that are several hundred times higher than in the observational data set. However, this mostly happens across areas where our model generates a non-existent fast flow. One of the best examples of such model artefacts is the former Ice Stream C in the Siple Coast, which is predicted by the model but has been stagnant for ~ 150 years in reality (Hulbe and Fahnestock, 2007; Engelhardt and Kamb, 2013). In some cases, the locations of the modelled ice streams are shifted relative to the observed ones, thereby generating adjacent zones of under- and overestimations of the surface velocity. In other cases, the modelled rapid ice flow follows a different route compared to observations, sometimes merging with neighbouring ice streams. These shifts may originate from local errors in the bedrock topography data accentuated by its projection onto the coarse horizontal grid we use here.

The mean errors in the absolute surface ice velocity fall within the range of ~ 16 to $\sim 55\,\mathrm{m\,yr^{-1}}$ (Table 2.3), with the HS-2b and SoS producing the minimum and maximum misfits, respectively, analogously to the results for the mean ice thickness errors discussed in Section 2.5.1. In the SoS simulation a general underestimation of the ice thickness near the ice sheet margins coincides with areas where sliding coefficients tend to reach the lower limit prescribed for the calibration. In turn, the use of such low values triggers a slowdown of the ice flow in the transition zone.

Although the results of the HS-2b simulation presented in Section 2.5.1 are in many aspects similar to those from the SoS, their abilities to reproduce the observed ice flow patterns are very different. The HS-2b uses the basal velocity from Eq. (2.2) (utilised by

the SoS) to compute the weights of relative contributions of the shallow approximations, thereby adding the SStA contribution where sliding velocities from Eq. (2.2) are high. In these rapidly flowing sectors, we attribute a better performance of the HS-2b compared to the SoS to the inclusion of the stress transmission by the SStA. It also fosters a SStA-dominated modelled ice flow in the surroundings of ice streams, particularly upstream, thereby improving the overall fit to observations. Compared to the HS-2b, the HS-2a has a similar performance with the second smallest mean velocity error of $17.6\,\mathrm{m\,yr^{-1}}$, followed by higher mean errors of 23.2 and $29.7\,\mathrm{m\,yr^{-1}}$ produced by the HS-3 and HS-1, respectively. Thus, the use of hybrid schemes allows for a two- to threefold reduction in the surface velocity misfit.

As described in Section 2.2.2, the hybrid schemes used in this study mainly differ in how the SStA weight, w, is computed. This controls not only relative contributions from the shallow approximations but also the locations where such combinations are implemented. In order to provide a deeper insight into how each hybrid scheme combines the SIA and SStA velocities, Figure 2.5 illustrates the equilibrated distributions of w. It can be immediately observed that the distributions of w produced by the hybrid schemes are very different, both in spatial coverage and inferred values. For example, the percentage of the grounded ice area where the modelled ice flow is dominated by the SStA ($w > 0.75$) is $\sim 30\,\%$ for the HS-1, but only 2.4 and $8.5\,\%$ for the HS-2a and HS-2b, respectively (Table 2.3). Furthermore, the transition between the SIA- and SStA-dominated ice-sheet sectors appears patchy in the HS-1, whereas it is smooth and collocated with the present-day ice streams in the HS-2a, thereby resembling the observed surface velocities. Such transitions are sharp in the HS-2b, implying a simple differentiation between fast and slow ice flow areas. This particular scheme exhibits a SIA-dominated ice flow regime ($w < 0.25$) over $82\,\%$ of the grounded ice area that may explain a high degree of similarity with the SoS, especially keeping in mind that it also includes basal sliding in the SIA. In contrast, the HS-2a sets basal ice velocities to zero in the computation of the SIA velocities, still producing a similar percentage of SIA-dominated area. In these sectors, differences in the ice thickness derived from the HS-2a and HS-2b (Figure 2.3, left column) can be attributed to a presence or absence of basal sliding in the computation of the SIA solution that may prevent overestimations e.g., in interior East Antarctica and cause underestimations in other sectors, such as the surroundings of Dronning Maud and MacRobertson Lands.

It is clear that the degree of agreement between the modelled and observed ice flow

is sensitive to the choice of a particular hybrid scheme and the way it measures relative SIA and SStA contributions. This can be best visualised using scatter plots of the modelled vs. observed surface velocities for each scheme, colour-coded for the values of the corresponding w distributions (Figure 2.5). In general underestimations of the modelled velocities occur across slowly flowing ($< 10\,\mathrm{m\,yr^{-1}}$) areas, which are dominated by the SIA, while the areas of fast flow dominated by the SStA are responsible for most of the overestimation. At a first glance it may seem that overestimations are caused by an excessive contribution of the SStA, but a comparison with the SoS scatter plot shows that this is not necessarily the case. The largest overestimations occur in the SoS simulation, with surface velocities reaching the upper permitted limit clustered in the upper part of the scatter plot (Figure 2.5). As mentioned above, the SoS and HS-2b share many similarities, and a comparison between their respective scatter plots shows that the use of the hybrid scheme reduces both underestimations in the lower velocity range and overestimations in the fast flowing areas.

2.5.3 Intercomparison of the inferred basal sliding coefficients

Although the performance of the hybrid schemes is quantitatively similar when evaluated against observations, the inferred values of basal sliding coefficients (C_0) vary by orders of magnitude in many regions of Antarctica (Figure 2.3, right column). It is important to keep in mind that these large differences between the inferred values of C_0 arise solely from the differences in the hybrid schemes, namely in their ways to combine the shallow approximations, since all other model components are exactly the same for all experiments.

To demonstrate the effects of prescribing a distribution of C_0 derived from one ice model (using a specific hybrid scheme) into a different ice model (using a different hybrid scheme or other level of approximation), we performed an additional set of experiments, which utilise the equilibrium states described in Section 2.5.1 as initial conditions. In these experiments, we exchange the distributions of C_0 inferred from the HS-2a and HS-2b, and then run the model over a period of 100 kyr. As described in Section 2.2.2, these schemes slightly differ in how they compute the SStA contribution, mainly due to different techniques used to account for basal sliding. Although both schemes identify similar locations of rapidly flowing ice (Section 2.5.2), their inferred distributions of basal sliding coefficients contain the highest variability among all hybrid schemes implemented in this study. At the end of these additional 100 kyr runs, the mean misfit between the modelled
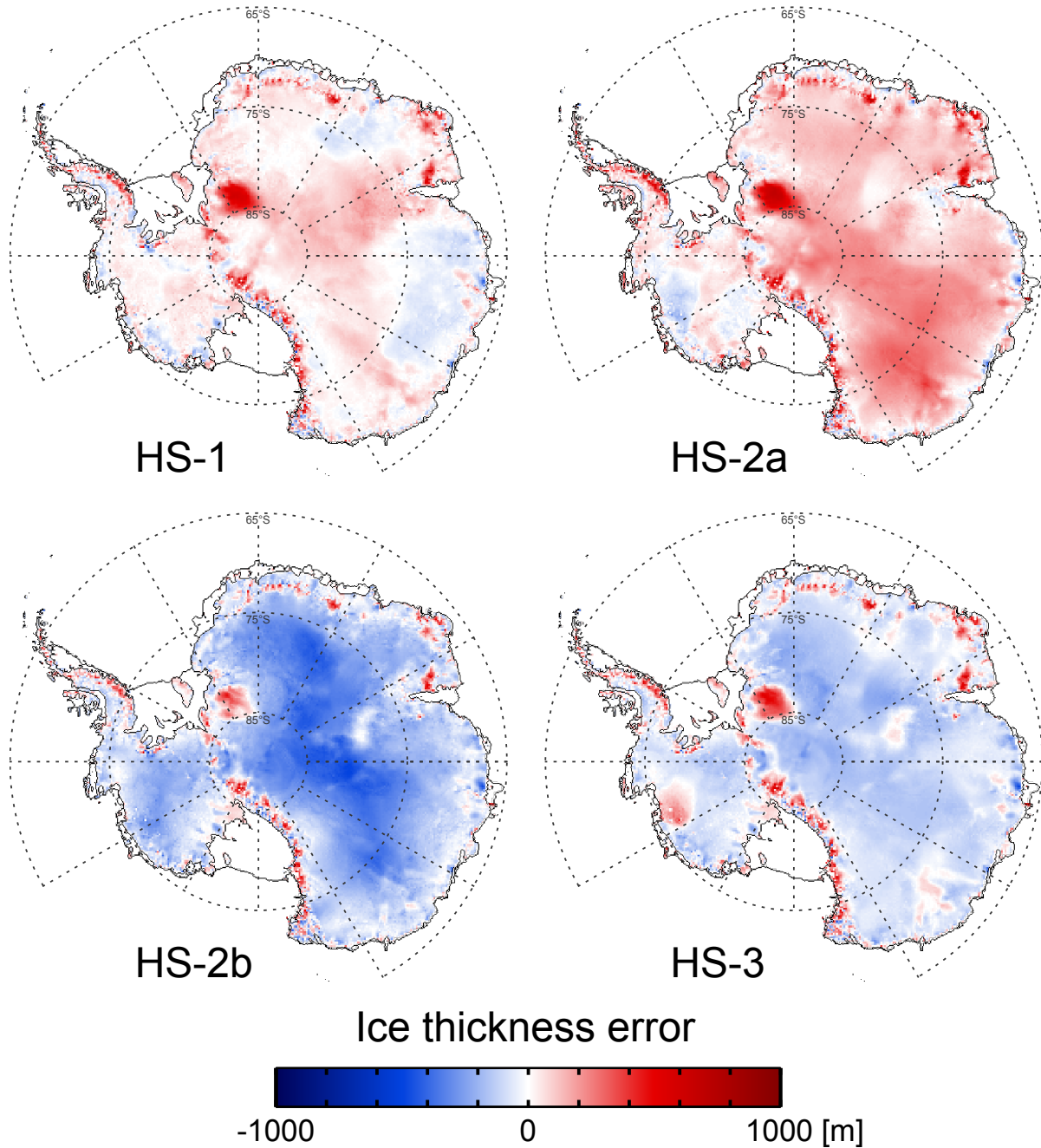
Figure 2.6: Difference between the modelled and observed ice thickness for all hybrid schemes, in metres, after additional $100\,\mathrm{kyr}$ runs in which a median of the inferred distributions of C_0 is prescribed at the ice-sheet base. The values of C_0 derived from the SoS are not included in the median distribution.

and observed ice thickness is above $200\,\mathrm{m}$ for the HS-2a and almost $350\,\mathrm{m}$ for the HS-2b (not shown). This represents increments of ~ 330 and $\sim 775\,\%$ in the deviations from observations, respectively.

To further exemplify the significance of the associated uncertainties in the retrieved basal sliding parameters, we prescribe the median of the inferred distributions of C_0, computed
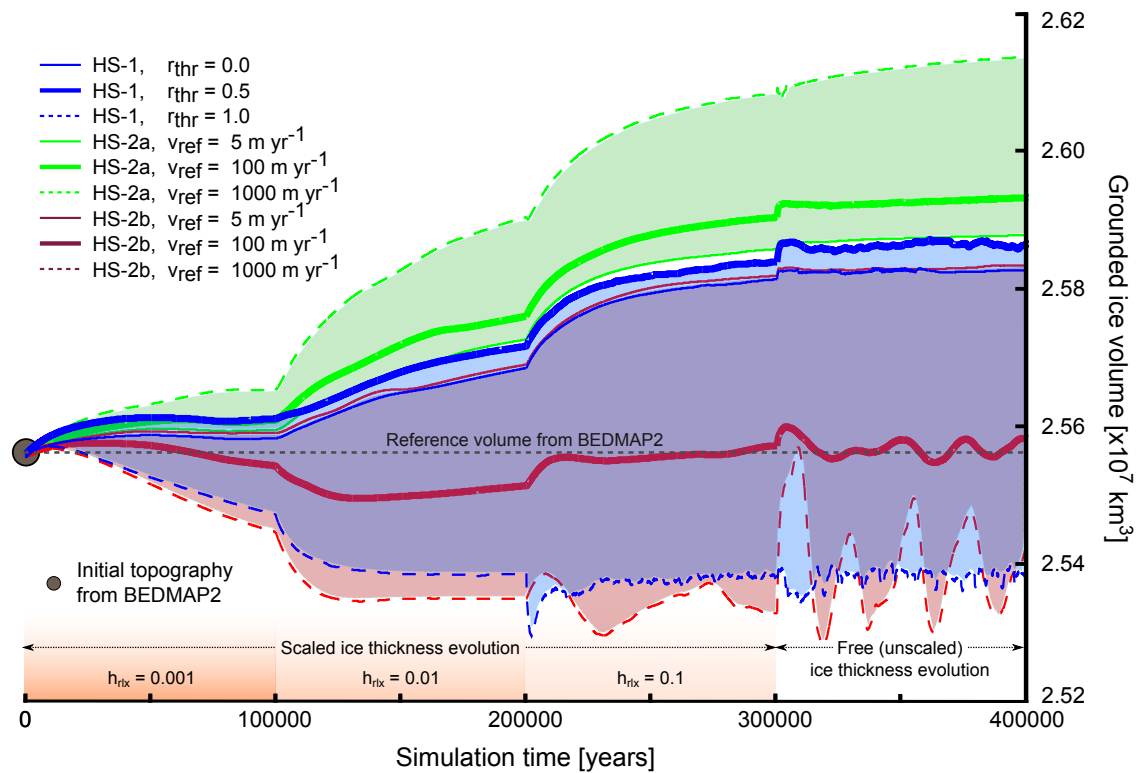
Figure 2.7: The evolution of the total grounded ice volume during the calibration procedure (as in Figure 2.2), in km^3, for different values of free parameters included in the computation of the SStA weight. The volume spread contains the reference values used for the experiments discussed in Sections 2.5.1–2.5.3 (solid thick lines) and values that are representative of the lower and upper limits of possible parameter ranges (thin solid and dashed lines, respectively).

from all hybrid schemes, at the base of the modelled ice sheet. Our choice of a median over an average is motivated by our initial tests in which generally larger values of C_0 inferred from the HS-2a tend to produce an average biased towards this particular distribution. Figure 2.6 shows differences between the modelled and observed ice thickness at the end of these additional runs. Comparison with Figure 2.3 reveals a general degradation of the fit between the model and observations. The HS-2a and HS-2b exhibit the largest sensitivity to the change in the basal sliding parameters, with a significant amplification of over- and underestimations of the ice thickness occurring across most of the ice sheet, respectively. For the HS-2a, an absolute ice thickness misfit increases by $\sim 180\%$ to a mean value of 131 m (Table 2.4), of which 95 % is due to overestimations. The misfit increases by $\sim 355\%$ to a mean value of 182 m in the HS-2b simulation, with underestimations of the ice thickness accounting for 88 % of the total difference. This degree of degradation is less pronounced when the HS-1 and HS-3 are used. The misfit for the HS-1 increases by only

$\sim 50\,\%$, displaying a mixture of areas where the modelled ice thickness is either too large or too small relative to observations. The HS-3 experiment shows an intermediate degree of sensitivity to a change in basal parameters and exhibits similar misfit patterns as the HS-2b, albeit the magnitude of the underestimation is smaller and the mean absolute error in the ice thickness remains around $100\,\mathrm{m}$. These experiments show that care is needed when using quantifications of the basal conditions obtained from external sources (e.g., Joughin et al., 2009; Morlighem et al., 2010; Arthern and Gudmundsson, 2010; Pralong and Gudmundsson, 2011; Pollard and DeConto, 2012b; Arthern et al., 2015) as input in ice flow models. This concerns not only differences between the basal sliding approaches implemented in each model, but also models using the same sliding law as part of different hybrid schemes, as shown in this study.

2.5.4 Exploration of the hybrid parameter space

The disparity in the results from the hybrid schemes presented in the previous sections showcases the impacts of slight changes in the model representation of fast flowing zones of ice sheets, even though it corresponds to a small fraction of the parameter space in ice-sheet models. In order to explore the sensitivity of the results to parameter variations within this parameter space, we perform an additional series of experiments where we vary the somewhat arbitrary threshold and reference quantities used by some of the hybrid schemes.

As described in Section 2.2.2, the hybrid schemes HS-1, HS-2a, and HS-2b use the weight w to calculate relative contributions of the SIA and the SStA. For the HS-1, the computation of w involves a prescribed threshold for the slip ratio of grounded ice (Eq. 2.8) that determines the locations where the hybrid velocity is calculated. The experiments discussed in the previous sections use a default value of $r_{\mathrm{thr}} = 0.5$, meaning that the SIA and SStA solutions are combined only in areas where the basal velocity is at least half of the surface velocity. In contrast, the HS-2a and HS-2b combine both shallow approximations everywhere, and w is computed using a prescribed reference velocity (Eqs. 2.10 and 2.11), using a default value of $v_{\mathrm{ref}} = 100\,\mathrm{m\,yr^{-1}}$. If the SStA velocity in the HS-2a or the basal velocity in the HS-2b reaches this reference value, the schemes assign equal weights to the SIA and the SStA. In general, higher values of r_{thr} or v_{ref} result in less contribution of the SStA solution, and vice versa.

The effects of variations in these parameters on the evolution of the total grounded ice
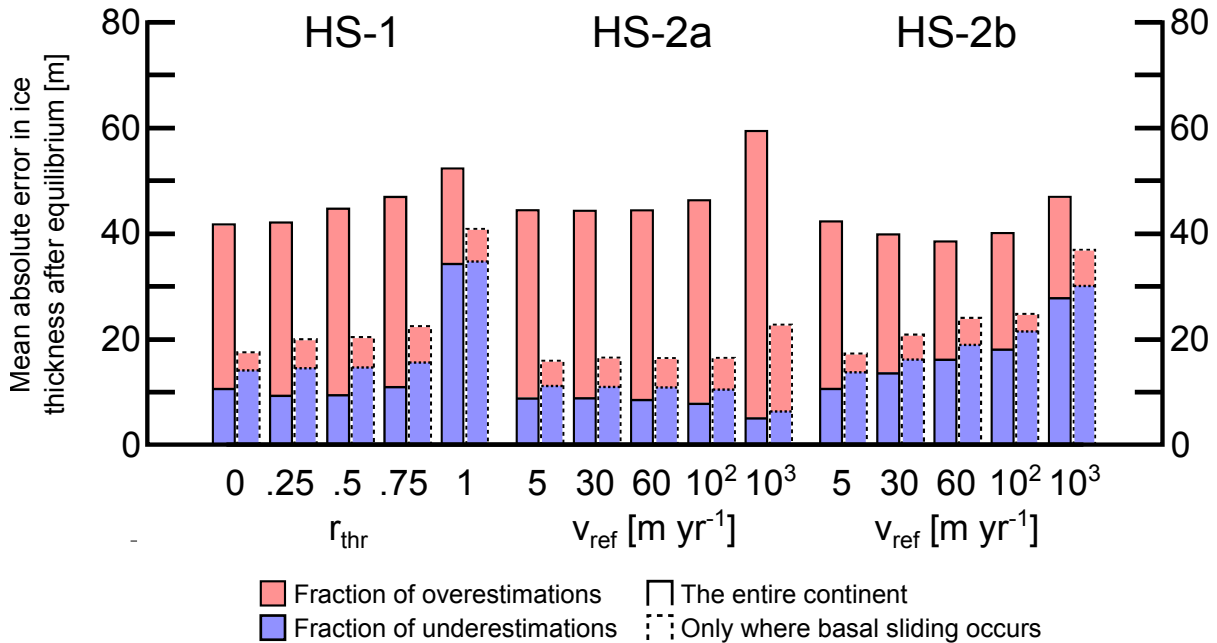
Figure 2.8: Mean absolute differences between the modelled and observed ice thickness at the end of the equilibrium simulations, in $\times 10^7 \, \text{km}^3$, for different values of free parameters included in the computation of the SStA weight. As in Figure 2.2, a mean error is calculated for the entire ice sheet (left bars) and separately over the areas where basal sliding is identified (right bars). Each bar is divided into relative errors arising from under- (blue) and overestimations (red).

volume during the calibration procedure are demonstrated in Figure 2.7. Here we test parameter values within a range that contains almost every possible scenario because values outside the range are with non-physical (HS-1) or exhibit no noticeable differences compared to the range limits (HS-2a and HS-2b).

For the HS-1, the upper limit for the slip ratio threshold, $r_{\text{thr}} = 1$, implies the use of a SIA-only solution, whereas the lower limit, $r_{\text{thr}} = 0$, implies that a combination of SIA and SStA solutions is applied everywhere, determined by the weight w computed using the slip ratio. Within the range of tested values, maximum deviations from the observed grounded ice volume are below 1.2%. Only the use of $r_{\text{thr}} = 1$ produces an ice sheet that is smaller than observed. An analysis of the mean absolute differences between the modelled and observed ice thickness (Figure 2.8) reveals that the use of larger values of r_{thr} leads to a larger misfit with observations, with the maximum error corresponding to $r_{\text{thr}} = 1$.

In the HS-2a, all tested values produce an ice sheet that is larger than observed. This is caused by a general overestimation of the ice thickness in the continental interior. Here, the modelled ice flow is slow and dominated by the SIA. Thus, the weights w are small, implying a negligible contribution of the SStA, independently of the value of v_{ref}. Values smaller than $v_{\text{ref}} = 100 \, \text{m yr}^{-1}$ are found to produce total grounded ice volumes and mean ice thickness

Table 2.4: Summary of the results for each hybrid scheme at the end of additional 100 kyr runs where the median of the inferred basal sliding coefficients from all implemented hybrid schemes is prescribed as an external forcing, including the total grounded ice volume, V_{grd} (km^3); a deviation from total grounded ice volume, ΔV_{grd} (%); a mean absolute error in the ice thickness, $\overline{\Delta H}$ (m); and a mean ice thickness error only where basal sliding operates, $\overline{\Delta_{\mathrm{sld}} H}$ (m).

Scheme	V_{grd} (km^3)	ΔV_{grd} (%)	$\overline{\Delta H}$ (m)	$\overline{\Delta_{\mathrm{sld}} H}$ (m)
HS-1	2.60×10^7	$+1.95$	67.0	45.2
HS-2a	2.70×10^7	$+5.58$	131.2	110.1
HS-2b	2.37×10^7	-7.41	182.1	167.6
HS-3	2.48×10^7	-2.97	105.0	104.8

misfits that are close to the results of the reference run ($v_{\mathrm{ref}} = 100\,\mathrm{m\,yr}^{-1}$), although with a slight improvement in the model fit to observations. Values of $v_{\mathrm{ref}} > 100\,\mathrm{m\,yr}^{-1}$ lead to a larger misfit, with the highest tested value of $v_{\mathrm{ref}} = 1000\,\mathrm{m\,yr}^{-1}$ producing a grounded ice volume that displays a deviation of $2.3\,\%$ from observations. The use of even larger values of v_{ref} asymptotically decreases the contribution of the SStA. It is important to note, however, that since the HS-2a does not include sliding in the SIA component, its solutions will never approach that of the SoS.

In contrast, the HS-2b activates the sliding law even in the regions where ice streams have not been identified by the scheme, as long as the conditions for sliding described in Section 2.2.1 are fulfilled. This may explain the similarity between the grounded ice volumes produced by the SoS and the HS-2b solutions, using a reference velocity set to the upper limit of $v_{\mathrm{ref}} = 1000\,\mathrm{m\,yr}^{-1}$. This parameter value produces a deviation of $-0.9\,\%$ from the observed ice volume, which is similar (but with opposite signs) to the misfit obtained from the simulation using the lower limit of $v_{\mathrm{ref}} = 5\,\mathrm{m\,yr}^{-1}$ tested in this study. For values higher than the default value of $v_{\mathrm{ref}} = 100\,\mathrm{m\,yr}^{-1}$, the simulations produce an ice sheet that is smaller than observed. The use of $v_{\mathrm{ref}} = 60\,\mathrm{m\,yr}^{-1}$ leads to the best fit between the modelled and observed ice thickness among all schemes and parameter values, reaching $\sim 39\,\mathrm{m}$, with a small deviation from the observed grounded ice volume of $0.27\,\%$.

However, it is important to keep in mind that the calibration procedure has a limited power to reduce the misfits between the model and observations in areas where no sliding occurs. This is why some deviations are expected from our numerical experiments, in particular due to overestimations of the ice volume over mountainous regions where the calibration procedure does not operate. Therefore, a perfect fit to the observed ice volume obtained by any of the schemes would likely involve underestimations of ice thickness in

other regions.

2.6 Summary and conclusions

We implemented and compared the performance of four hybrid schemes for the combination of the shallow ice and shelfy stream approximations as part of the ice-sheet model SICOPOLIS. The use of shallow approximations enables continental-scale, long-term palaeo-simulations of ice sheets, preventing the restrictive computational expenses of more complex models. Moreover, hybrid schemes overcome the limitations of simpler SIA-only models in regions characterised by rapid ice flow driven by basal sliding. The hybrid schemes in this study differ in the ways (1) relative contributions of the shallow approximations are computed, (2) areas where a combination of shallow approximations is applied are identified, and (3) the basal sliding is accounted for.

By adapting a simple iterative technique to infer the distribution of basal sliding parameters from observational topographic data sets (Pollard and DeConto, 2012b), we show that all the applied hybrid schemes produce dynamic equilibrium states that are in a good agreement with observations. For all the schemes, mean ice thickness misfits range from 40 to 52.4 m, and the total grounded ice volume deviations do not exceed 2.5 % for a wide range of the associated parameter uncertainties. For optimal parameter choices, mean errors in the ice thickness remain below 40 m. For comparison, present-day simulations in continental-scale ice-sheet models typically produce widespread errors in the ice thickness reaching hundreds of metres, with deviations in total grounded ice volume that can exceed 10 % (e.g., de Boer et al., 2015). A clear limitation of the calibration method presented here is the possibility of an error cancellation during the adjustment of C_0. At present there is no easy way to differentiate between the effects of an artificial compensation of, for example, the lacking model physics or errors in the input data sets through the model calibration and the model parameters that are representative of the actual conditions at the base of the ice sheet. This shortcoming will hopefully be overcome in the future once the necessary observational data sets become available and the use of more sophisticated ice models more feasible. The degree of applicability of the calibrated C_0 distributions for long-term palaeoclimate simulations is currently unclear, and its quantification requires further modelling studies of the past ice-sheet geometries. However, we believe that the retrieved variability in basal sliding coefficients is a good first-order approximation and is

certainly a better guess than commonly used spatially uniform values of C_0 over the entire domain. We believe that the method used to derive C_0 could be potentially extended to the use for other time periods or climate regimes (or even adapted for the transitions between largely dissimilar regimes), providing that the necessary topographic and climate data are available. Considering the recent efforts to reconstruct the past geometries of the AIS (Mackintosh et al., 2014; Bentley et al., 2014), this may well become possible in the upcoming decades.

We also computed a non-hybrid, SIA-only solution to allow for a qualitative separation of relative contributions of the SIA and the SStA. Such direct comparison is possible because all the hybrid schemes analysed in this study share identical model components. Although the calibration procedure applied to the SIA-only scheme also produces a reasonable fit to observations, the misfits are overall larger than those from the hybrid schemes. Moreover, the modelled surface velocities exhibit noise-like patterns at and around locations where rapid ice flow exists. Since these patterns are not present in the hybrid solutions, we attribute their occurrence to the lack of stress transmission in the SIA flow model.

We find that individual weights assigned to the SIA and SStA solutions vary significantly from scheme to scheme. For the schemes in which the SIA and SStA weights are computed, the modelled ice flow is dominated by the SIA over ~ 50 to $\sim 80\,\%$ of the AIS, with the predominant contribution of the SStA generally limited to the locations and surroundings of the observed ice streams.

Comparison of our results with an independent, observational data set of surface ice velocities reveals a reasonable agreement in the continental interior of Antarctica. However, the modelled ice flow appears to be too fast at the ice-sheet margins in all hybrid schemes, especially close to the observed ice stream locations. These misfits between the modelled and observed surface velocities are contrasted by relatively small differences between the modelled and observed ice thickness in these areas. Such misfits may originate from other factors such as uncertainties in the observational ice thickness and surface velocity data sets (Fretwell et al., 2013; Rignot et al., 2011, see Section 2.3), the limited model resolution, the assumption of an ice-sheet equilibrium with present-day climate conditions, and/or errors in the model-based geothermal heat flux and/or climatic forcing (Pollard and DeConto, 2012b).

Although all hybrid schemes produce a comparably good fit to the observational topographic data set, the inferred values of basal sliding coefficients largely differ between

different schemes. Therefore, the discrepancies in the representation of the ice dynamics by different hybrid schemes are compensated through adjustments of this poorly constrained parameter. Nevertheless, the schemes mostly agree on the areas where the ice base is at or close to the local pressure-melting point. Furthermore, there is a qualitative agreement in the patterns of low vs. high values of C_0 obtained from each calibration run. Although any attempt to quantify a local potential for sliding would require new and improved observational data sets describing basal conditions, the robustness of the inferred patterns provides an initial guess for their real distribution.

Furthermore, we have evaluated the performance of each hybrid scheme based on both its fit to observations and its numerical stability for a range of model set-ups and have found that at grid resolutions higher than $20\,\mathrm{km}$ (e.g., 15 and $10\,\mathrm{km}$) the HS-1 and HS-2b become numerically unstable and stop before the experiments are completed, owing to large gradients in basal sliding coefficients arising from the use of basal velocities as boundary conditions for the SIA solutions in conjunction with the calibration of sliding coefficients. In addition, variations in the free parameter r_{thr} of the HS-1 generate artefacts in the resulting basal temperature field. The HS-2a and HS-3, which utilise the SStA as a sliding law, are numerically more stable to variations in model parameters and changes in grid resolution. The drawback of the HS-2a is in its limited ability to improve the fit between the modelled and observed ice thickness in ice-sheet sectors where the SStA velocities are low ($<\,100\,\mathrm{m\,yr^{-1}}$), which is the case for large parts of the Antarctic interior. This limitation is independent of the choice of the parameter v_{ref} (Figure 2.7). The HS-3 overcomes this limitation by accounting for the SStA contribution everywhere. However, the HS-3 also utilises the SIA velocities over the entire ice sheet, which in certain areas are excessively high, such as the steep ice-sheet margins (Figure 2.4), leading to an increased root-mean-square error compared to HS-2a (Figure 2.5). To improve the performance of both schemes, our future work will reconcile the drawbacks of HS-2a with the advantages of HS-3, providing a very stable and flexible hybrid scheme.

Finally, we assessed the effects of differences between the calibrated sliding parameters derived from the four hybrid schemes by performing additional experiments in which the inferred distributions of C_0 were either averaged or exchanged between the schemes. Our results show that the parameter distributions are not exchangeable between the schemes, since this leads to a strong degradation of the model fit to observations. This suggests that results of a model calibration and/or initialisation cannot be straightforwardly transferred

to a model that uses a different level of approximation of the Stokes equations. Given an increasing number of studies attempting to quantify the basal conditions under ice sheets through a variety of methods including ice flow models, our experiments show that one needs to be careful when using the inferred basal sliding parameters as external boundary conditions in glaciological models.

Context

The reconstructions of subglacial sliding conditions under the Antarctic ice sheet presented in Chapter 2 shed light on largely unknown basal regimes of the grounded ice sheet sectors and potentially on the mechanical properties of the underlying Earth surface. Although the inferred distributions of basal sliding parameters strongly depend on the choice of a model formulation, they have reached a consensus across multiple areas with predominantly high or overall low sliding potentials, providing training grounds for advancement of the current observational techniques. Furthermore, the very dependence of these subglacial reconstructions on the model representation of the fast-flowing ice dynamics serves as an example of important controls of basal sliding on the development of ice streams (e.g., Winsborrow et al., 2010). However, there are other significant factors such as the ocean and atmospheric conditions that strongly impact the dynamics of the Antarctic ice streams. Even though the Antarctic continent has received an increasing attention from the scientific community over the last decades, observations of the atmospheric and especially ocean conditions in this region still remain fragmentary, and the uncertainties in these key drivers of the ice sheet dynamics are very large. Thus, the following chapters attempt to quantify the impacts of these uncertainties on the modeled dynamics of the present-day Antarctic ice sheet through a combination of a novel modelling approach and a large array of available observations as a comprehensive validation tool.

Chapter 3 focuses on the interaction between the ocean and the Antarctic ice sheet that mainly occurs through the floating ice sheet sectors, which are thought to hold important controls on the overall ice sheet dynamics. These controls are enabled through feedbacks between rapidly flowing ice streams and ice shelves, in which ice streams transport masses from the continental interior over distances of several hundreds of kilometers, while ice shelves buttress this ice flux from the grounded ice sheet. Changes in the thermal ocean state perturb the stability of this feedback system, triggering advances, retreats, or even collapses of individual ice sheet sectors. Currently, the interaction between the ocean

and ice shelves is responsible for $\sim 99\%$ of the annual mass loss from the Antarctic ice sheet through basal melting and iceberg calving (Rignot et al., 2013). Traditionally the lack of observations of ablation and accretion processes under the Antarctic ice shelves has represented a challenge for continental-scale modelling studies of the Antarctic ice flow. This is because the computation of total mass balance as well as the modelled ice geometry and flow modes depend sensitively on the accuracy of the melting and freezing rates prescribed at the ice shelf base. Although some workarounds have been suggested, they usually involve the use of oversimplified parameterisations that have not been validated against available observations. These parameterisations are commonly tuned to compensate for the erroneous ice flux across grounding lines and thus reduce the deviations between the large-scale features of the modelled and observed ice sheets such as volume and extents (e.g., de Boer et al., 2015).

Building upon the results of the previous chapter and advancing previously utilised methods, Chapter 3 presents a new model-based technique for the derivation of modern ocean-induced basal melting and refreezing rates under the entire Antarctic ice-shelf system. It shows that the reconstructed basal sliding conditions presented in the previous chapter result in realistic ice flow patterns and sub-shelf regimes, which are in a close agreement with recent observations.

Chapter 3

Melting and freezing under Antarctic ice shelves from a combination of ice-sheet modelling and observations

Chapter Abstract

Ice shelf basal melting is the largest contributor to the negative mass balance of the Antarctic Ice Sheet. However, current implementations of ice-ocean interactions in ice-sheet models disagree with the distribution of sub-shelf melt and freezing rates revealed by recent observational studies. Here we present a novel combination of a continental-scale ice-flow model and a calibration technique to derive the spatial distribution of basal melting and freezing rates for the whole Antarctic ice-shelf system. The modelled ice-sheet equilibrium state is evaluated against topographic and velocity observations. Our high-resolution (10-km spacing) simulation predicts an equilibrium ice-shelf basal mass balance of -1648.7 $\mathrm{Gt\,a^{-1}}$ that increases to -1917.0 $\mathrm{Gt\,a^{-1}}$ when the observed ice-shelf thinning rates are taken into account. Our estimates reproduce the complexity of the basal mass balance of Antarctic ice shelves, providing a reference for parameterisations of sub-shelf ocean-ice interactions in continental ice-sheet models. We perform a sensitivity analysis to assess the effects of variations in the model set-up, showing that the retrieved estimates of basal melting and freezing rates are largely insensitive to changes in the internal model parameters, but respond strongly to a reduction of model resolution and the uncertainty in the input data sets.

3.1   Introduction

Ice shelves are floating ice masses connected to and nourished by land-based ice. They are thought to exert an important control on the dynamics of the grounded ice sheet sectors (Rignot et al., 2004; Dupont and Alley, 2005; Rott et al., 2011; Gudmundsson, 2013), buttressing and buffering the ice flux where it reaches the ocean. Thus, ice shelf thinning and removal holds an indirect, albeit significant potential for a contribution to sea level variations. Recent studies have shown that changes in the ocean thermal state play a critical role in ice shelf thinning and a subsequent loss of buttressing (e.g., Pritchard et al., 2012). Present-day observations suggest that over a half of the Antarctic mass loss is due to sub-shelf basal melting (Depoorter et al., 2013; Rignot et al., 2013), with melting rates ranging from a few centimeters to tens of meters per year, and values near grounding lines exceeding area-averaged rates by one to two orders of magnitude (Rignot et al., 2002). Since basal melt rates are likely to increase in the future due to increasing ocean temperatures (e.g., Gillett et al., 2011; Yin et al., 2011; Hellmer et al., 2012), a better understanding of their magnitudes and spatial distribution is a crucial requirement for reliable projections of the ice sheet evolution and sea level rise (Joughin et al., 2012).

Net melt rates under ice shelves have been previously estimated using different techniques based on surrounding oceanographic data (Gammelsrod et al., 1994; Foldvik et al., 2001; Jenkins and Jacobs, 2008; Jacobs et al., 2011), local glaciological observations (Doake, 1984; Jacobs et al., 1992; Rignot et al., 2002; Joughin and Padman, 2003; Wen et al., 2010), and satellite data (Rignot et al., 2013; Depoorter et al., 2013). Numerical ocean modelling has provided high-resolution reconstructions of basal melt rates under a number of individual ice shelves (Gerdes et al., 1999; Jenkins and Holland, 2002; Holland et al., 2009, 2010; Schodlok et al., 2012; Padman et al., 2012; Hellmer et al., 2012), and total ice-shelf meltwater production estimates from circumpolar simulations (Hellmer, 2004; Timmermann et al., 2012). These studies have presented total ice-shelf basal mass balance (BMB) estimates ranging from ~ -500 to $\sim -1700\,\mathrm{Gt\,a^{-1}}$. Recent estimates based on satellite data (Rignot et al., 2013; Depoorter et al., 2013) have uncovered the spatial distribution of the melting and freezing zones for the entire Antarctic ice-shelf system. Although the total BMB estimates provided by these particular studies are comparable and within the above-mentioned range, they disagree in the contributions of individual ice shelf sectors (Rignot et al., 2013; Depoorter et al., 2013).

Ice flow models require an accurate quantification of the ice shelf BMB to reproduce the

dynamics of ice when it is in contact with the ocean. Due to scarcity of whole-Antarctic BMB estimates in the past and high computational costs of coupled regional ocean-ice sheet modelling experiments, stand-alone continental-scale ice models have so far mostly relied on simplified parameterisations to account for ice-ocean interactions. These approaches range from a prescription of a single-value (spatially uniform) basal melting rates over the entire domain (e.g., Bindschadler et al., 2013) to simplified parameterisations using homogeneous or modelled (extrapolated) ocean temperatures (e.g., Beckmann and Goosse, 2003; Holland et al., 2008), which are kept constant in space and time (e.g., Martin et al., 2011; de Boer et al., 2015). These parameterisations are commonly calibrated against the observed ice volumes and extents, and the resulting melting rates are not necessarily consistent with the oceanographic and glaciological BMB estimates. Furthermore, these parameterisations usually disregard sub-shelf freezing processes that have been shown by observational studies to occur under vast portions of the Antarctic ice shelves.

Here, we build upon the concepts used to interpret observations (Rignot et al., 2013; Depoorter et al., 2013) and implement a method combining stand-alone ice sheet-shelf simulations and topographic data (Bernales et al., 2017a) to quantify sub-shelf melting and freezing rates. With this novel approach, we derive total, sector- and ice shelf-specific BMB values that can be directly compared to previous glaciological and oceanographic estimates. Furthermore, the use of a numerical model allows us to explore the sensitivity of the results to changes in the model grid resolution, and uncertainties in the input data sets and model parameters.

3.2 Methods

3.2.1 Ice sheet-shelf model

We use the ice sheet-shelf model SICOPOLIS (SImulation COde for POLythermal Ice Sheets) version 3.2, revision 619 (Sato and Greve, 2012; Greve and Blatter, 2009). The model set-up closely follows that of Bernales et al. (2017a). The experiments described in this study use a one-layer enthalpy scheme recently implemented in the model (Greve and Blatter, 2016). Additional modifications to the model specifically for this study are presented below.

At its core, the model solves for the ice velocity using finite-difference implementations of the Shallow Ice and Shallow Shelf Approximations (SIA and SSA, respectively; e.g.,

Hutter, 1983; Morland, 1987). The SSA is used to compute ice velocities of ice shelves, which experience almost no friction at their interface with sea water, whereas the SIA is used across the grounded ice sheet sectors, where the mechanical properties of the bedrock and crustal heat flow create a variety of friction conditions, ranging from nearly immobile ice masses frozen to bed to fast flowing ice streams sliding over water-saturated sediments. Since basal sliding is not accounted for in the SIA, ice flow models have traditionally implemented various empirical sliding laws as an additional boundary condition. Bueler and Brown (2009) proposed to use a modified SSA including basal drag (also known as the Shelfy Stream Approximation, SStA) as a sliding law, showing that this heuristic, "hybrid" combination of the SIA and the SStA is able to reproduce most ice flow regimes. Bernales et al. (2017a) compared different implementations of this idea, and in this study we are using a modification of the approach proposed by Winkelmann et al. (2011), as follows: first, the SIA velocities are computed while setting basal velocities to zero. Then, the SStA velocities are computed using a Weertman-type sliding law (see Bernales et al., 2017a, Eq. 2–6) with a basal drag coefficient that has been calibrated to minimise the difference between the modelled and observed ice thickness data (Pollard and DeConto, 2012b; Bernales et al., 2017a). Finally, both solutions are combined over the entire ice sheet using

$$\mathbf{U} = (1 - w) \cdot \mathbf{u}_{\text{sia}} + \mathbf{u}_{\text{ssta}}, \tag{3.1}$$

where $\mathbf{u}_{\text{sia}}$ and $\mathbf{u}_{\text{ssta}}$ are the SIA and SStA horizontal velocities, respectively, and w is a weight computed following Bueler and Brown (2009):

$$w(|\mathbf{u}_{\text{ssta}}|) = \frac{2}{\pi} \arctan \left(\frac{|\mathbf{u}_{\text{ssta}}|^2}{u_{\text{ref}}^2} \right), \tag{3.2}$$

where u_{ref} is a reference velocity, set to $30 \, \text{m} \, \text{a}^{-1}$, following Bernales et al. (2017a). This particular scheme decreases the contribution of the SIA velocities in areas where high SStA velocities are detected. Such fast flowing areas are mostly located near ice sheet margins, where ice streams operate, and the assumptions behind the SIA are no longer valid. The hybrid scheme presented in this study reduces instabilities in these regions caused by artificially high SIA velocities, the absence of which is assumed but not assured by Winkelmann et al. (2011). The resulting ice velocity is used to solve the evolution equations of the ice thickness and temperature (Greve and Blatter, 2009), providing the main components for the steady-state experiments presented in this study.

3.2.2 Input data

The observed ice sheet geometry is derived from the BEDMAP2 data set (Fretwell et al., 2013), including bedrock elevation, ice surface topography, and ice sheet and shelf thickness. The original 1-km-resolution data are regridded to a horizontal resolution of 10 km, currently representing one of the highest resolutions computationally viable for long-term (hundreds of thousands of years), continental-scale forward ice-sheet modelling. BEDMAP2 is a compilation of 24.8 million ice thickness data points obtained from a variety of sources including airborne and over-snow radar surveys, satellite altimetry, seismic sounding data, and satellite gravimetry (Fretwell et al., 2013). Complemented by surface elevation data from several digital elevation models to derive previously unknown bedrock features, this compilation allows for a detailed modelling of the Antarctic ice sheet-shelf system.

The geothermal heat flux map of Fox Maule et al. (2005) is prescribed at the base of a modelled lithospheric layer, and the thermal effect at the base of the ice sheet is computed using a temperature equation that balances local temperature changes with advection and heat conduction (Greve and Blatter, 2009). Atmospheric conditions at the surface of the ice sheet and ice shelves, including near-surface (2 m) air temperatures and precipitation rates, are obtained from the regional climate model RACMO2.3 (henceforth RACMO, van Wessem et al., 2014), averaged over the period 1979–2010. RACMO is forced at its boundaries by reanalysis data from ERA-Interim over the same period (Dee et al., 2011). In the interior of the domain the Antarctic climate conditions are modelled with a horizontal resolution of 27 km and 40 levels in the vertical direction. RACMO contains modules specifically implemented for glaciated regions, including a multilayer snow model, and compares well with in situ observations (van Wessem et al., 2014).

The precipitation rates and near-surface air temperatures are used to compute the accumulation rates following the relation of Marsiat (1994). Temperatures are adjusted to changes in topography through a simple lapse-rate correction of 0.008 °C m. Surface melt is computed using a positive degree-day (PDD; Reeh, 1991; Calov and Greve, 2005) scheme with melt factors $\beta_{snow} = 3$ and $\beta_{ice} = 8$ mm i.e. day^{-1} ^{o}C^{-1} for snow and ice, respectively. All forcing data sets have been projected onto the same polar stereographic grid used for the BEDMAP2 data, with a horizontal resolution of 10 km for the main simulation, and 20 and 40-km resolutions for the sensitivity experiments presented in Section 3.3.2.

3.2.3 Experimental set-up

The initial bedrock-, sea floor-, and basal and surface ice elevations relative to the present-day sea level are defined using the 10-km-spaced topographic data from BEDMAP2 (see Section 3.2.2). The model domain embraces the entire Antarctic ice sheet-shelf system and the surrounding Southern Ocean, and contains 601×601 equidistant grid points in the horizontal direction, and 81 grid points in the vertical direction (densifying towards the base), used for the computation of the temperature and velocity fields. Below the ice sheet, additional 41 grid points form the modelled lithospheric thermal layer. The ice flow enhancement factors for the SIA and SSA are set to the values $E_{SIA} = 1$ and $E_{SSA} = 0.5$, respectively. The initial ice temperature for the entire model grid is set to a homogeneous value of $-10\,^\circ\text{C}$ (results do not depend on this initial choice). Then, external forcing data sets are prescribed at the boundaries of the system (see Section 3.2.2): the time-invariant geothermal heat flux data are prescribed as the lower boundary of the thermal bedrock model used to compute the temperatures at the ice sheet base, whereas the precipitation rates and near-surface temperature are used to compute the surface mass balance and ice surface temperatures.

From this configuration, the model is run forward in time in four main stages designed to provide a model spin-up and the calibration of two key quantities: the spatial distribution of the basal drag coefficient for the grounded ice sheet, and the basal melting/freezing rates for the ice shelves. Initial values for both quantities are $1\,\text{m}\,\text{a}^{-1}\,\text{Pa}^{-1}$ and $0\,\text{m}\,\text{a}^{-1}$, respectively, corresponding to a rough bedrock that opposes basal sliding and no melt or accretion at the base of ice shelves. Throughout the simulations, the grounding line and ice shelf fronts are kept at their modern positions in order to ensure a consistent model calibration (Bernales et al., 2017a). In the first stage, the model solves the evolution equations for temperature, velocity, and thickness every 5 model-years, during a simulation period of $50,000$ years. The distinct feature of this stage is that it scales the evolution of the ice thickness by a factor of 10^{-3}, keeping the ice thickness close to its initial (i.e. observed) value (Bernales et al., 2017a). This allows for an initialisation of the ice-sheet thermodynamics that is not contaminated by artificial changes in the ice geometry. In contrast to a fixed-topography approach (e.g., Pattyn, 2010; Sato and Greve, 2012), this procedure allows for an evolution of the ice thickness and thus for a continuous calibration of the basal sliding coefficients and basal melt rates during the entire simulation. In addition, it can be combined with a much larger time step (that would otherwise generate numerical

instabilities) and ensures that the temperature within the ice can reach an equilibrium with time-invariant boundary conditions at a normal pace, considerably speeding up the simulations.

In the grounded ice sheet, changes in the ice thickness are tracked by a calibration algorithm that adjusts the basal drag coefficient at each grid point every 50 model-years to locally minimise the difference between the modelled and observed (i.e., initial) ice thickness. This procedure is based on the idea of Pollard and DeConto (2012b), which is explored and modified by Bernales et al. (2017a). In the ice shelves, a similar algorithm adjusts the magnitude of the basal melting or freezing rates every 20 years, keeping the ice shelves close to their observed thickness, following:

$$\text{BMR}^* = \text{BMR} + F_{\text{tan}} \cdot \tan\left(\frac{H - H_0}{H_{\text{scl}}}\right), \tag{3.3}$$

where BMR^* and BMR are the current and previous basal melting rates (representing freezing if negative), respectively, H and H_0 are the current (modelled) and reference (from BEDMAP2) ice thicknesses, the parameter $F_{\text{tan}} = 1.725$ scales the adjustment, and $H_{\text{scl}} = 100\,\text{m}$ is a scaling factor introduced to prevent overshoots. For the same reason, the argument of the trigonometric function is restricted to a range of -1.5 to $+1.5$ (see Table 3.2 for experiments with different parameter choices).

The second and third stages use the same set-up (starting from the results of the previous stage), but instead scale the ice thickness evolution by factors of 10^{-2} and 10^{-1}, respectively. The final stage involves an unscaled evolution of the ice thickness, solving the thermodynamical model equations every 0.5 years until an equilibrium is reached. These four stages enable a fast, stable convergence towards an equilibrium ice-sheet state. The steady-state experiments presented in this study provide the spatial distribution of basal melting and freezing rates required to keep the Antarctic ice shelves in equilibrium for the simulated dynamical state with a fixed grounding line (see the Supplementary Materials for an analysis of the effects of this constraint). In order to allow for a direct comparison with the observation-based estimates of Rignot et al. (2013) and Depoorter et al. (2013), we add (during the post-processing) observation-based ice shelf thinning rates (Pritchard et al., 2012) to our steady-state estimates, as a proxy for the "non-steady-state" melt rates. This procedure is qualitatively equivalent to that of Rignot et al. (2013) and Depoorter et al. (2013), since these studies use the mass conservation to determine the BMB, while
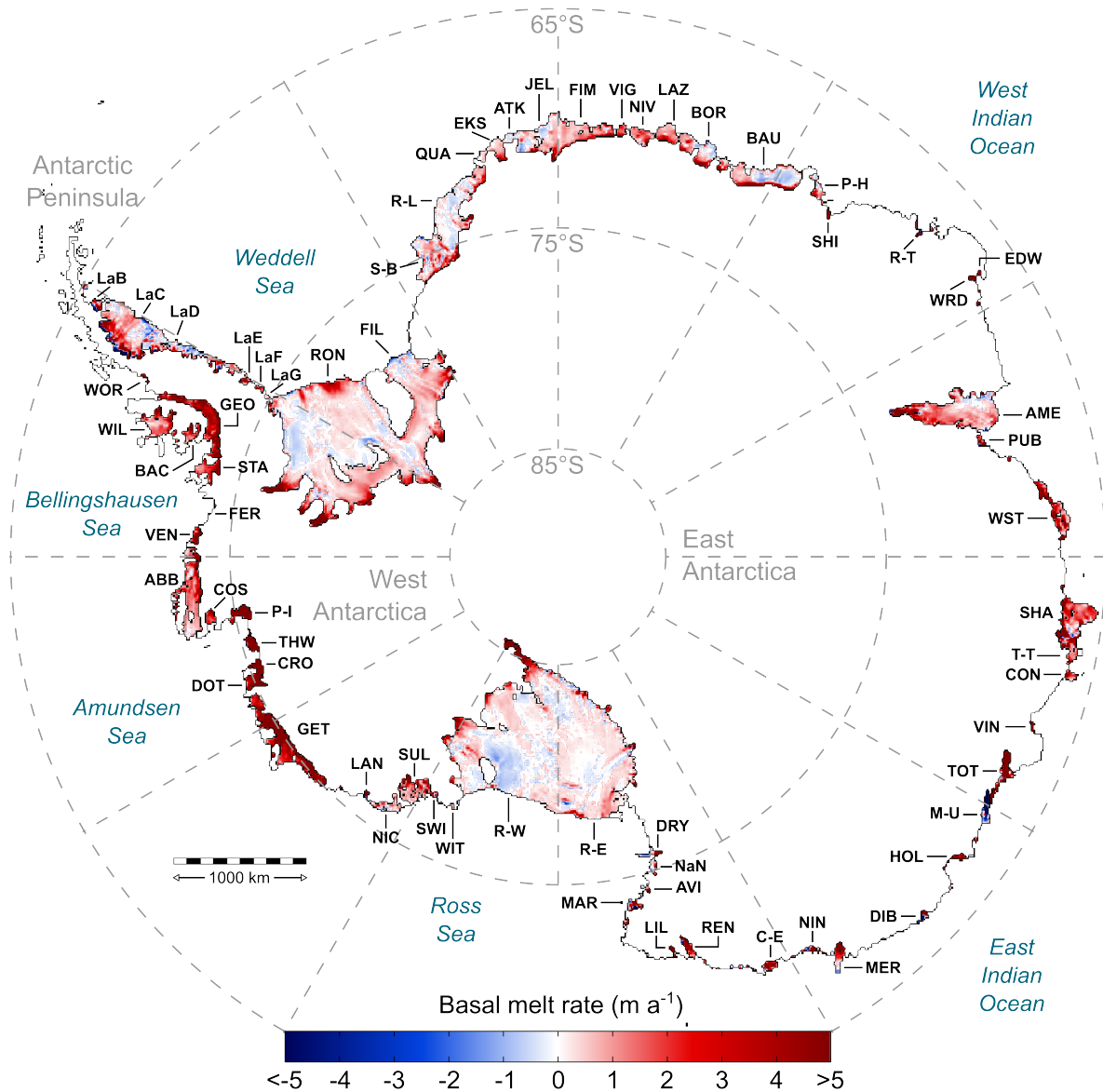
adding the ice shelf thinning rates to account for a non-equilibrium behaviour. However, the cited studies use a 2007–2008 ice surface velocities (Rignot et al., 2011), which are not necessarily in equilibrium. A comparison between our steady-state ice velocities and the velocities used in Rignot et al. (2013) and Depoorter et al. (2013) is presented as part of the results (Section 3.3.1).

3.3   Results and discussion

3.3.1   Retrieved basal thermal states of ice shelves

In this section we present the estimated ice-shelf BMB from our simulations of the present-day Antarctic ice sheet, which have been run to an equilibrium with the modern climate conditions. The retrieved distribution of basal melting and freezing rates beneath the Antarctic ice shelves (Figure 3.1) is far from being homogeneous, with alternating zones of melting and freezing. The presence of accretion zones is clearly visible under the largest ice shelves (Ronne, Filchner, Ross East, and Ross West; see Figure 3.1 for a location map and Table 3.1 for abbreviations). Noticeable accretion zones are also present along the coast of East Antarctica, from the Stancomb–Brunt to Prince Harald ice shelves. Overall, the distribution of melting and freezing zones is similar to that of Rignot et al. (2013), where melting is strongest near grounding lines and ice shelf fronts, while freezing mostly occurs under the central parts of ice shelves (see Supplementary Figure A.3). In addition, we retrieve a predominant melting under the smaller ice shelves whose grounding lines are close to the calving fronts, where the smooth basal topography and small ice shelf extents prohibit an accretion from ice-shelf-water plumes (Depoorter et al., 2013). Unexpectedly high rates of basal melting along the East Antarctic coast reported by Rignot et al. (2013) and Depoorter et al. (2013) are also reproduced by our model, particularly near grounding lines. In addition, we infer a predominant sub-shelf melting in the West and East Indian Oceans, between the Shirase and Totten ice shelves. As for individual ice shelves, our retrieved patterns closely resemble those from Rignot et al. (2013) in most areas, with striking similarities in the sub-shelf melting/freezing patterns of the large ice shelves near the ice fronts (see Supplementary Figure A.3).

Our estimate of the total ice-shelf steady-state BMB is $-1648.7\,\mathrm{Gt\,a^{-1}}$, which increases to $-1917\,\mathrm{Gt\,a^{-1}}$ when the observational ice-shelf thinning rates of Pritchard et al. (2012) are taken into account. The latter value is larger than the estimates of Rignot et al.

Figure 3.1: Predicted basal melting (freezing if negative) rates of Antarctic ice shelves, in metres of ice per year. Modern ice-shelf thinning rates (Pritchard et al., 2012) are added to account for a non-steady-state behaviour. See Table 3.1 for details.

(2013) $(-1500 \pm 237\,\mathrm{Gt\,a^{-1}})$ and Depoorter et al. (2013) $(-1454 \pm 174\,\mathrm{Gt\,a^{-1}})$. The degree of agreement, however, varies for different Antarctic sectors. Our estimates in both the Antarctic Peninsula and West Antarctica are relatively closer to the observation-based studies than in East Antarctica, where our values are considerably higher. This difference reflects generally higher rates of basal melting for many ice shelves, especially near grounding lines required by the model to replicate the observed ice shelf thickness. These are the areas where the model calibration of the ice shelf BMB compensates for

any excess of influx – relative to an equilibrium – from the grounded ice sheet. We partly attribute our higher estimates to a combination of the following effects:

1. Compared to Rignot et al. (2013) and Depoorter et al. (2013), our numerical simulations of the Antarctic ice sheet-shelf system make use of the near-surface temperature and precipitation rate model output from a more recent version of the regional atmospheric model RACMO (van Wessem et al., 2014). The two versions (RACMO2.3 here and RACMO2.1 in the cited studies) differ in their representation of the atmospheric conditions over East Antarctica, with RACMO2.3 generating considerably wetter conditions dominated by higher snowfall rates (van Wessem et al., 2014), and therefore a higher ice flux of $1061.7\,\mathrm{Gt\,a^{-1}}$ into the ice shelves, compared to $782 \pm 80\,\mathrm{Gt\,a^{-1}}$ used by Rignot et al. (2013).

2. Our calibration of basal melt rates requires a steady influx of ice mass from the grounded glaciers, which is achieved through the calibration of the ice sheet model using an assumption of an equilibrium with the present-day climate conditions, as described in Section 3.2. An inclusion of the observed ice sheet elevation changes during the calibration of continental-scale forward models is, at present, a very challenging task, due to orders-of-magnitude differences between the length of the observational record and the time scales over which these models operate. Thus, recent observations of the ice sheet thickening in East Antarctica (e.g., Davis et al., 2005; Shepherd et al., 2012; Pritchard et al., 2012) are not included; instead, the observation-inferred positive change in the ice mass is driven towards the ice shelves, where our calibration of basal melting rates accounts for it, thus producing higher estimates. The opposite can be observed in our results for the West Antarctic ice shelves, where the BMB estimates in areas where the ice sheet is thinning (e.g., the Amundsen Sea sector) are lower than those of Rignot et al. (2013).

3. In contrast to the observation-based studies, our method does not employ an external data set of the observed ice surface velocities, but instead uses the ice velocity computed by the ice model. We compare the resulting ice surface velocities to the observational data set of Rignot et al. (2011) (Figure 3.2). General characteristics of the observed Antarctic ice flow are well reproduced by the model, particularly in areas of rapid ice flow and across the transition zones between slow- and fast-flowing ice sectors. The mean absolute difference between the observed and modelled surface

Table 3.1: Description of individual characteristics of the Antarctic ice shelves, including modelled surface mass balance (SMB), grounding-line flux (GL), ice-front flux (IF), basal mass balance (BMB), and basal melting rate (BMR, with positive values representing melting). BMB and BMR values include equilibrium (left) and non-steady-state (right) values. BMR values are in water equivalent, computed using a reference ice density of $910\,\mathrm{kg\,m^{-3}}$. All values are corrected for area distortions caused by the polar stereographic projection following Snyder (1987)

Name	Code	Area (km²)	Area (km²)	GL (Gt a⁻¹)	SMB (Gt a⁻¹)	BMB (Gt a⁻¹)	BMR (m a⁻¹)
Larsen B	LaB	3568	-0.4	20.7	-13.3	-7.1 / -8.3	2.0 / 2.3
Larsen C	LaC	47903	19.1	49.1	-29.6	-39.6 / -40.8	0.8 / 0.9
Larsen D	LaD	23584	9.6	29.8	-3.6	-36.5 / -20.0	1.5 / 0.8
Larsen E	LaE	1520	0.7	3.6	-0.9	-3.5 / -3.4	2.3 / 2.2
Larsen F	LaF	712	0.3	1.0	-0.4	-0.9 / -1.4	1.2 / 2.0
Larsen G	LaG	510	0.2	0.5	-0.3	-0.3 / -0.3	0.5 / 0.5
Wordie	WOR	594	0.6	18.4	-7.2	-11.9 / -11.2	20.1 / 18.8
George VI	GEO	24276	11.7	70.6	-6.7	-77.2 / -92.1	3.2 / 3.8
Wilkins	WIL	14256	10.1	14.9	-1.7	-23.8 / -27.4	1.7 / 1.9
Bach	BAC	3924	1.3	7.7	-1.1	-7.9 / -10.5	2.0 / 2.7
Stange	STA	7794	6.2	15.4	-2.7	-19.1 / -24.7	2.5 / 3.1
Antarctic Peninsula		**128640**	**58.9**	**232.1**	**-66.9**	**-228.8 / -241.0**	**1.8 / 1.9**
Ronne	RON	336834	62.7	215.1	-88.1	-184.4 / -229.0	0.5 / 0.7
Ferrigno	FER	102	0.1	3.3	-2.0	-1.2 / -4.7	11.8 / 46.5
Venable	VEN	3136	3.6	12.7	-8.4	-8.0 / -14.9	2.6 / 4.8
Abbot	ABB	31808	28.0	33.6	-7.6	-54.9 / -51.5	1.7 / 1.6
Cosgrove	COS	2940	1.7	4.5	-1.9	-4.4 / -7.0	1.5 / 2.4
Pine Island	P-I	5920	5.0	77.1	-27.8	-55.1 / -82.2	9.3 / 13.9
Thwaites	THW	4494	4.0	71.9	-34.9	-42.0 / -63.0	9.3 / 14.0
Crosson	CRO	3165	3.3	18.3	-4.5	-17.4 / -34.4	5.5 / 10.9
Dotson	DOT	5402	5.5	19.7	-2.7	-22.8 / -37.5	4.2 / 6.9
Getz	GET	34211	33.4	76.0	-27.2	-84.0 / -147.5	2.5 / 4.3
Land	LAN	717	0.7	11.2	-4.6	-7.0 / -6.6	9.7 / 9.3
Nickerson	NIC	6455	4.4	6.1	-3.8	-6.9 / -3.9	1.1 / 0.6
Sulzberger	SUL	13392	7.9	21.5	-1.7	-28.2 / -25.7	2.1 / 1.9
Swinburne	SWI	928	0.8	3.1	-1.5	-2.3 / -2.2	2.5 / 2.4
Withrow	WIT	412	0.2	0.6	-0.6	-0.2 / -0.2	0.6 / 0.5
Ross West	R-W	303621	29.7	98.5	-67.7	-57.8 / -51.9	0.2 / 0.2
Other		615	0.4	12.2	-5.7	-7.0 / -	11.3 / -
West Antarctica		**754152**	**192.2**	**690.4**	**-288.1**	**-592.0 / -788.8**	**0.8 / 1.0**
Filchner	FIL	101237	12.3	92.8	-29.9	-72.4 / -84.9	0.7 / 0.8
Stancomb–Brunt	S-B	37666	13.8	22.4	- 8.4	-28.3 / -24.3	0.8 / 0.6
Riiser–Larsen	R-L	43199	14.8	21.0	-9.8	-26.4 / -15.4	0.6 / 0.4
Quar	QUA	2103	0.6	0.9	-1.3	-0.2 / -0.6	0.1 / 0.3
Ekstroem	EKS	6502	3.1	5.5	-1.8	-6.9 / -7.0	1.1 / 1.1
Atka	ATK	2195	1.1	0.6	-0.7	-1.0 / -0.3	0.5 / 0.1
Jelbart	JEL	35539	17.1	25.8	-10.2	-33.0 / -27.8	0.9 / 0.8
Fimbul	FIM	16346	6.2	20.4	-6.5	-20.1 / -23.1	1.2 / 1.4
Vigrid	VIG	2488	1.0	3.5	-1.8	-2.8 / -4.7	1.1 / 1.9
Nivl	NIV	7369	3.1	10.1	-3.8	-9.5 / -8.9	1.3 / 1.2
Lazarev	LAZ	8645	3.4	7.5	-3.4	-7.6 / -10.9	0.9 / 1.3
Borchgrevnik	BOR	20609	8.5	26.6	-15.0	-20.3 / -20.0	1.0 / 1.0
Baudouin	BAU	32912	10.6	34.9	-14.8	-31.2 / -22.8	0.9 / 0.7
Prince Harald	P-H	5543	4.8	7.9	-5.2	-7.9 / -5.0	1.4 / 0.9
Shirase	SHI	696	0.2	24.0	-5.2	-18.2 / -17.1	26.2 / 24.7
Rayner–Thyer	R-T	881	0.4	11.0	-1.4	-9.4 / -9.7	10.7 / 11.0
Edward VIII	EDW	389	0.4	2.9	-1.3	-2.1 / -2.6	5.4 / 6.7
Wilma–Robert–Downer	WRD	780	0.5	13.0	-0.6	-13.1 / -13.1	16.8 / 16.8
Amery	AME	60970	11.9	87.8	-17.5	-80.7 / -100.1	1.3 / 1.6
Publications	PUB	1588	0.1	9.3	-3.7	-5.6 / -5.5	3.5 / 3.5
West	WST	15098	8.1	48.5	-21.5	-35.5 / -47.1	2.4 / 3.1
Shackleton	SHA	29307	20.1	60.4	-24.0	-57.3 / -88.7	2.0 / 3.0
Tracy–Tremenchus	T-T	2319	1.1	1.6	-0.3	-2.6 / -3.6	1.1 / 1.5
Conger	CON	2510	1.6	1.9	-1.1	-2.5 / -3.9	1.0 / 1.6
Vincennes	VIN	875	0.5	23.3	-10.8	-13.5 / -13.5	15.5 / 15.5
Totten	TOT	8286	9.1	115.2	-34.8	-92.1 / -103.3	11.1 / 12.5
Moscow University	M-U	4286	2.8	30.5	-19.3	18.1 / 18.2	-4.2 /-4.2
Holmes	HOL	1654	2.7	22.3	-16.8	-8.7 / -9.6	5.3 / 5.8
Dibble	DIB	1551	1.7	15.8	-13.2	-4.4 / -5.9	2.8 / 3.8
Mertz	MER	5761	4.1	25.4	-8.5	-21.1 / -18.2	3.7 / 3.2
Ninnis	NIN	1868	1.2	29.6	-18.6	-12.5 / -10.8	6.7 / 5.8
Cook East	C-E	2954	1.6	21.8	-11.9	-12.0 / -8.5	4.1 / 2.9
Rennick	REN	3295	0.8	11.7	-0.8	-11.7 / -13.7	3.6 / 4.2
Lillie	LIL	799	0.3	10.8	-1.0	-10.1 / -10.1	12.6 / 12.6
Mariner	MAR	2836	1.4	6.6	-4.4	-3.9 / -3.6	1.4 / 1.3
Aviator	AVI	914	0.2	2.9	-0.9	-2.3 / -2.5	2.5 / 2.6
Nansen	NaN	2041	0.3	3.2	-0.8	-2.8 / -2.7	1.4 / 1.4
Drygalsky	DRY	2864	0.3	9.1	-4.2	-5.5 / -5.9	1.9 / 2.0
Ross East	R-E	193692	32.9	71.2	-26.0	-78.2 / -88.7	0.4 / 0.4
Other		7208	3.1	73.9	-44.8	-32.1 / -	4.4 / -
East Antarctica		**677775**	**202.7**	**1061.7**	**-407.3**	**-823.8 / -893.1**	**1.2 / 1.3**
Total Antarctica		**1560567**	**453.7**	**1986.5**	**-760.4**	**-1648.7 / -1917.0**	**1.1 / 1.2**
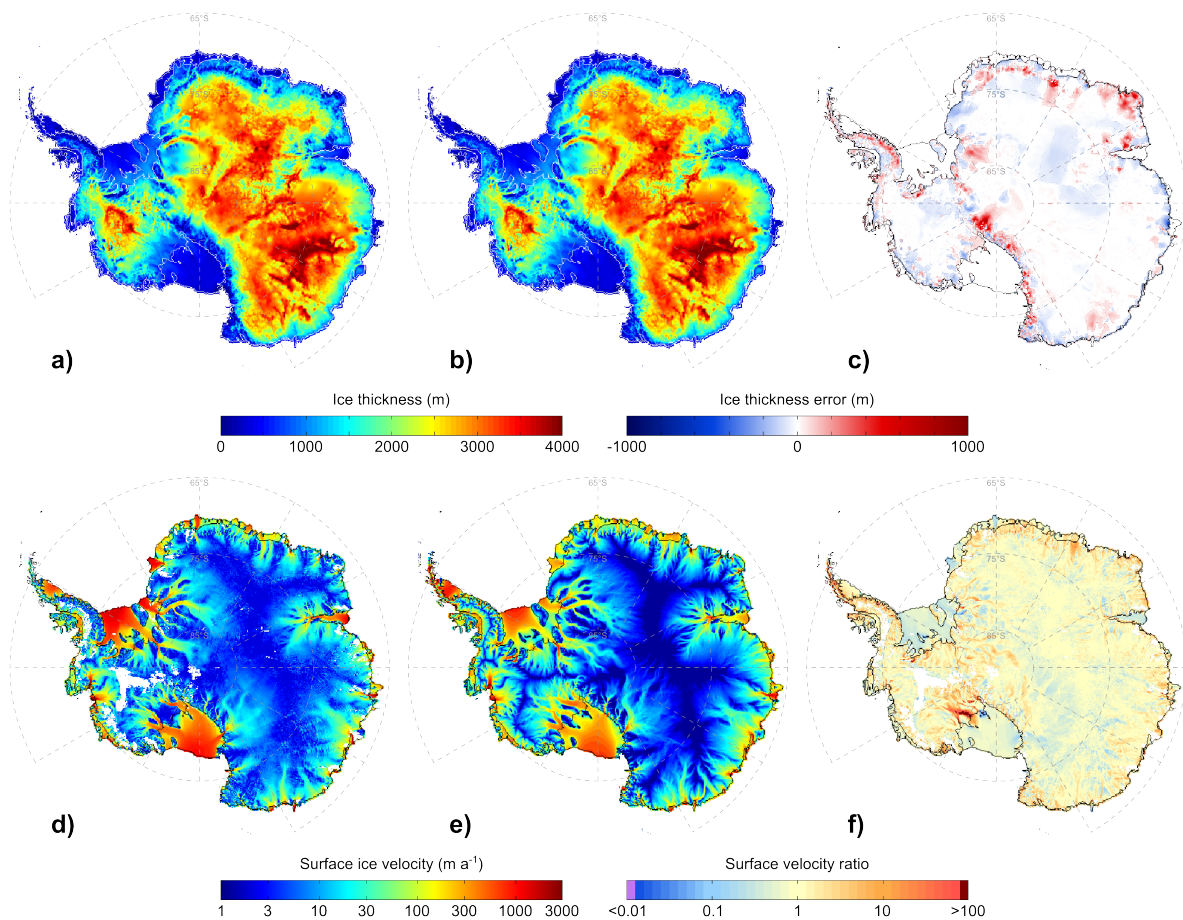
Figure 3.2: Top row: Comparison between the observed (a) and the modelled (b) Antarctic ice thickness distribution, in metres, together with the corresponding ice thickness error (c), in metres. Observational ice thickness data are taken from Fretwell et al. (2013). Bottom row: Comparison between the observed (d) and the modelled (e) Antarctic ice surface velocities, in $\mathrm{m\,a^{-1}}$, together with the ratio between the two (f), excluding very low velocities ($< 1\,\mathrm{m\,a^{-1}}$). Observational ice velocity data are taken from Rignot et al. (2011).

ice velocities is $40.1\,\mathrm{m\,a^{-1}}$. The largest error occurs at the location of the former Ice Stream C (Figure 3.2f), the existence of which is predicted by the model regardless of its stagnant behaviour over the last ~ 150 years (Hulbe and Fahnestock, 2007). Furthermore, ice velocities in some ice shelves (e.g., Ronne/Filchner, Amery, and Stancomb–Brunt) are somewhat underestimated by the model, which we partly attribute to our choice of the ice flow enhancement factor in the computation of the SSA velocities (see Section 3.3.2). The computed ice velocities can also be affected by the assumption of an ice sheet equilibrium with the present-day climate conditions, among other potential sources of uncertainty as discussed below. This may result in too-fast flow at the ice sheet margins, especially near the observed ice stream locations (Bernales et al., 2017a), requiring higher melting rates to account for the

increased ice influx relative to observations. Figure 3.2 also shows the misfit between the modelled and observed ice thickness (Fretwell et al., 2013), with a mean absolute ice thickness error being equal to 31.7 m. This misfit is significantly below the values that are usually found in modelling studies of the Antarctic ice sheet (Pollard and DeConto, 2012b), mainly due to the calibration of the basal sliding coefficients in the grounded ice sheet and of basal melting and freezing rates under the floating ice sectors. The largest ice thickness errors occur in mountainous regions, where basal thermal conditions do not favour ice sliding and the calibration is not performed (Bernales et al., 2017a).

In addition to the effects of the neglected non-steady-state behavior mentioned above, deviations from the observation-based estimates may be partly explained by other limitations of our method. These include a relatively coarse resolution of the model (10 km) when compared to that of Rignot et al. (2013) and Depoorter et al. (2013) (1 km for ice thickness and 450 m for ice velocities) that also influences the location of the grounding line and ice-front flux gates. As described in Section 3.2, our model employs a hybrid combination of the SIA and SStA to compute the ice-sheet velocities, which could be affected by the lack of the higher-order dynamics (e.g., Gagliardini et al., 2013), especially across the transition zones near grounding lines. The magnitude of such influences will be hopefully assessed, as soon as similar experiments become feasible using higher-order models. Additional limitations arise from the uncertainties in the input data sets required by our model (e.g., the geothermal heat flux, climate forcing, and bedrock topography) that influence the modelled ice-sheet dynamics and thus the estimates of the ice-shelf BMB, although the observational methods are also affected by the uncertainties in the topographic and climate data. Another limitation of both our model-based and observational methods is that they only provide estimates of basal melting and freezing rates for the present-day ice-shelf configuration, and the direct applicability of the retrieved values for scenarios with grounding-line migration driven by, for example, climate variations is not ensured (see Supplementary Materials). In the following sections, we present additional experiments that explore the influence of some of these limitations and uncertainties on the estimated ice shelf BMB.

The large accretion zones retrieved along the Antarctic Peninsula, under big ice shelves (Ronne, Filchner, Ross East, and Ross West), and at the East Antarctic coasts (mainly between the Stancomb–Brunt and Prince Harald ice shelves) are found to contribute

$+214\,\mathrm{Gt\,a^{-1}}$ to our total BMB estimate, covering more than a quarter of the total ice shelf area. This significant contribution to the total BMB is commonly disregarded by existing parameterisations of ice-ocean interactions (e.g., Beckmann and Goosse, 2003; Holland et al., 2008). A potential workaround to compensate for the disregarded freezing would be to reduce the basal melt rates elsewhere to obtain an area-average value in agreement with observations. However, such option must ensure that the melt rates in key areas, such as grounding zones, are not significantly affected, to prevent artificial changes in the ice shelf geometry.

Table 3.1 summarises our estimates of the ice-shelf BMB and the corresponding area-averaged melting rates. Major characteristics of the retrieved BMB are presented in the form of sector– and ice-shelf–averaged estimates, which allow for a direct comparison with previous estimates from other methods. Although the horizontal grid resolution used in this study is at the limit of what is currently feasible for whole-Antarctica forward modelling experiments, deviations from the ice shelf areal extents presented in previous studies are inevitable, due to their higher resolution (~ 100 times). For many applications of ice sheet models the grid resolution is very important, and we discuss it in a greater detail in the following section, where we present an analysis of potential sources of uncertainty on the reconstructed BMB of ice shelves.

Table 3.1 also presents the retrieved BMB for individual ice shelves, including the corresponding area-averaged basal melting rates. Average melt rates range from -4.2 (indicating freezing conditions under the Moscow University ice shelf, East Antarctica) to $46.5\,\mathrm{m\,a^{-1}}$ (indicating melting conditions under the Ferrigno ice shelf, West Antarctica), showing a similar variability to that found by Rignot et al. (2013). Our model predicts local ice-shelf basal melting rates ranging from ~ -28 to $\sim 103\,\mathrm{m\,a^{-1}}$. The minimum value marks the accretion under the Moscow University ice shelf, whereas the maximum value is detected at the grounding line of the Pine Island ice shelf. Freezing rates similar to those predicted at the base of the Moscow University ice shelf can be found elsewhere but only in isolated points, which most likely originate from an insufficient ice influx from the grounded ice sheet caused by the low model grid resolution (relative to the observation-based studies). To keep the ice shelf thickness close to observed, the calibration scheme compensates for the lack of resolution through unrealistic basal freezing rates near the grounding line. Other potential model deficiencies arising from its limited resolution are discussed in a greater detail in Section 3.3.2. Numerous areas with very high melting rates ($> 25\,\mathrm{m\,a^{-1}}$)
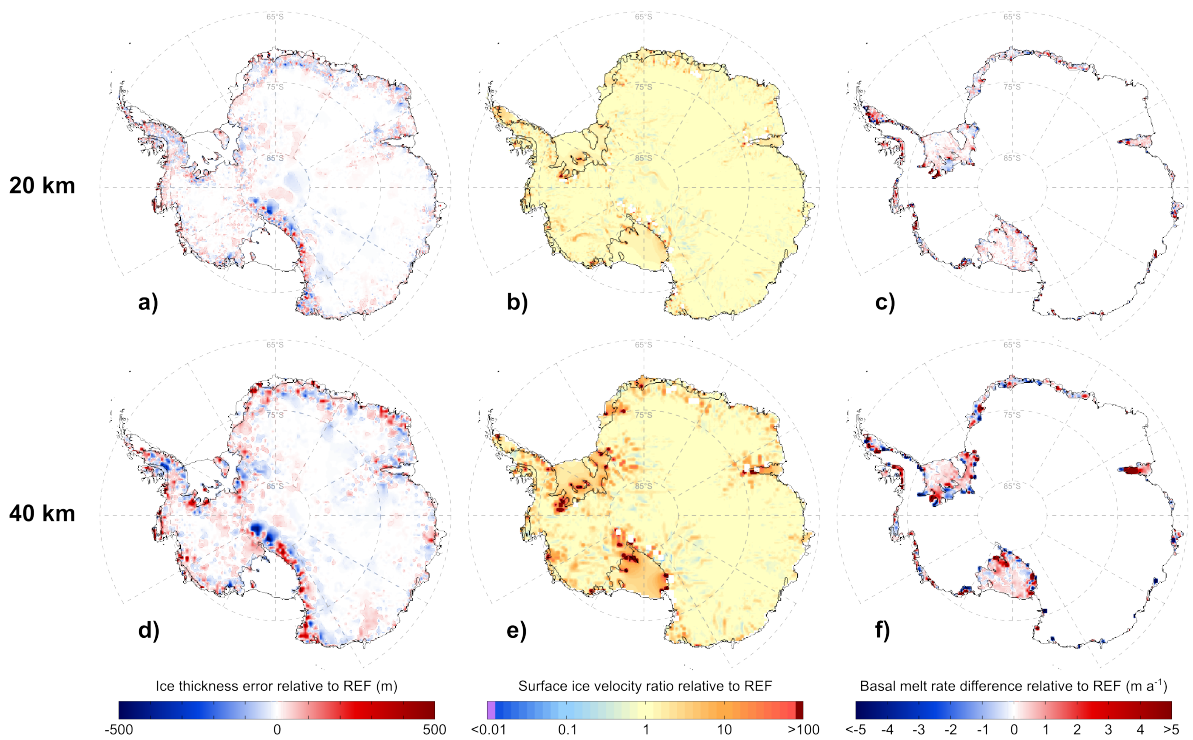
Figure 3.3: Results of experiments that employ different horizontal grid resolutions, including 10 km (top row), 20 km (mid row), and 40 km (bottom row). Ice thickness errors (left column) and surface ice velocity ratios (mid column) as in Figure 3.2, although relative to REF. Estimated basal melting and freezing rates (right column) computed as the difference relative to REF (see Figure 3.1)

are found along the grounding lines of the Wordie, Ferrigno, Thwaites, Totten, Shackleton, Amery, and Shirase ice shelves.

Grounding lines are known to exhibit melting rates that for many ice shelves are one-to-two orders of magnitude higher than area-average values (Rignot et al., 2002). Although some modelling studies have suggested sub-shelf melting rates with similar magnitudes (e.g., Payne et al., 2007), the implementation of such high rates is not commonplace in large-scale, long-term ice-sheet modelling experiments. Our model-based results support the idea that ice flow models developed to study the dynamics of ice sheet-shelf systems may over-simplify and underestimate the influence of the ocean thermal forcing when parameterisations (e.g., Beckmann and Goosse, 2003; Holland et al., 2008) are used. Although neither present-day observational data nor our estimates of melting and freezing rates can provide the necessary transient ice shelf BMB for long-term simulations, our methodology and results can be used to aid the development of new parameterisations which will be designed to fit the magnitudes and spatial patterns necessary to simulate the observed or hypothetical ice-sheet dynamical states under a variety of climate conditions.

Table 3.2: Summary of the sensitivity experiments performed in this study, including: experiment name-code adopted in text, short description of the difference with respect to the reference experiment REF, number of figure(s) in text, horizontal grid resolution ($\Delta x, y$), mean absolute error in the ice thickness after equilibrium ($\overline{\Delta H}$), total basal mass balance (BMB), and area-averaged basal melting rate (BMR). BMB and BMR values include equilibrium (left) and non-steady-state (right) values. BMR values are in water equivalent, computed using a reference ice density of $910 \, \mathrm{kg \, m^{-3}}$. All values are corrected for area distortions caused by the polar stereographic projection, following Snyder (1987).

Experiment	Short description	Figure	$\Delta x, y$ (km)	$\overline{\Delta H}$ (m)	BMB ($\mathrm{Gt \, a^{-1}}$)	BMR ($\mathrm{m \, a^{-1}}$)
REF	Reference simulation	3.1 and 3.2	10	31.7	-1648.7 / -1917.0	1.1 / 1.2
GR20	Horizontal grid resolution of 20 km	3.3d–f	20	33.8	-1907.9 / -2180.8	1.2 / 1.4
GR40	Horizontal grid resolution of 40 km	3.3g–i	40	41.2	-2215.8 / -2470.4	1.4 / 1.6
BED	Perturbation of bed topography	3.4a–c	20	29.2	-2282.6 / -2555.7	1.5 / 1.7
GHF	Two-valued geothermal heat flux	3.4d–f	20	34.0	-1468.8 / -1742.0	0.9 / 1.1
ERA	ERA-Interim climate forcing	3.4g–i	20	44.3	-1687.5 / -1960.7	1.1 / 1.3
HS-B	Hybrid scheme based on Bueler and Brown (2009)	—	20	34.0	-2094.2 / -2367.4	1.3 / 1.5
SoS	SIA-only scheme	—	20	48.8	-2843.9 / -3117.0	1.8 / 2.0
SLD	Sliding law with $n = 2$	—	20	32.8	-2074.9 / -2348.0	1.3 / 1.5
ENHa	Ice-shelf enhancement factor set to $E_{\mathrm{SSA}} = 1$	—	10	31.6	-1565.1 / -1833.4	1.0 / 1.1
ENHb	Ice-shelf enhancement factor set to $E_{\mathrm{SSA}} = 2$	—	10	31.6	-1465.1 / -1733.5	0.9 / 1.0
ENHc	Ice-shelf enhancement factor set to $E_{\mathrm{SSA}} = 3$	—	10	31.7	-1391.3 / -1659.6	0.9 / 1.0
CAL1a	Calibration factor set to $F_{\mathrm{tan}} = 1 \, \mathrm{m}$	—	10	31.7	-1631.7 / -1900.0	1.1 / 1.2
CAL1b	Calibration factor set to $F_{\mathrm{tan}} = 2 \, \mathrm{m}$	—	10	31.7	-1631.9 / -1900.3	1.1 / 1.2
CAL2a	Calibration time step set to 5 years	—	10	31.7	-1630.8 / -1899.1	1.0 / 1.2
CAL2b	Calibration time step set to 10 years	—	10	31.7	-1631.0 / -1899.3	1.1 / 1.2
CAL2c	Calibration time step set to 50 years	—	10	31.7	-1631.5 / -1899.8	1.1 / 1.2
CAL3a	Calibration scaling factor set to $H_{\mathrm{scl}} = 50 \, \mathrm{m}$	—	10	31.7	-1632.3 / -1900.6	1.1 / 1.2
CAL3b	Calibration scaling factor set to $H_{\mathrm{scl}} = 200 \, \mathrm{m}$	—	10	31.7	-1631.8 / -1900.1	1.1 / 1.2
CAL3c	Calibration scaling factor set to $H_{\mathrm{scl}} = 500 \, \mathrm{m}$	—	10	31.7	-1630.9 / -1899.2	1.0 / 1.2
PDDa	PDD factors set to $\beta_{\mathrm{snow,ice}} = 3 \, \mathrm{mm \, day^{-1} \, {}^\circ C^{-1}}$	—	20	33.8	-1904.4 / -2177.6	1.2 / 1.4
PDDb	PDD factors set to $\beta_{\mathrm{snow,ice}} = 5 \, \mathrm{mm \, day^{-1} \, {}^\circ C^{-1}}$	—	20	33.8	-1911.3 / -2184.5	1.2 / 1.4
PDDc	PDD factors set to $\beta_{\mathrm{snow,ice}} = 11 \, \mathrm{mm \, day^{-1} \, {}^\circ C^{-1}}$	—	20	33.8	-1892.7 / -2165.8	1.2 / 1.4
PDDd	PDD factors set to $\beta_{\mathrm{snow,ice}} = 15 \, \mathrm{mm \, day^{-1} \, {}^\circ C^{-1}}$	—	20	33.7	-1901.4 / -2174.5	1.2 / 1.4
LRCa	Lapse-rate correction set to $6 \, {}^\circ \mathrm{C \, km^{-1}}$	—	20	33.7	-1895.9 / -2169.0	1.2 / 1.4
LRCb	Lapse-rate correction set to $7 \, {}^\circ \mathrm{C \, km^{-1}}$	—	20	33.8	-1906.0 / -2179.1	1.2 / 1.4
LRCc	Lapse-rate correction set to $9 \, {}^\circ \mathrm{C \, km^{-1}}$	—	20	33.9	-1908.4 / -2181.6	1.2 / 1.4
LRCd	Lapse-rate correction set to $10 \, {}^\circ \mathrm{C \, km^{-1}}$	—	20	33.9	-1891.1 / -2164.2	1.2 / 1.4

3.3.2 Exploration of uncertainties

In this section, we present the results of modelling experiments that explore the influence of potential uncertainties in the input data sets and model formulation. We first analyse the sensitivity of the model results to a reduction of the model resolution in order to justify the use of a two-fold lower resolution in our sensitivity tests relative to REF. Other than that, all presented experiments share identical model set-ups with the REF experiment (Section 3.2) presented in Figs 3.1 and 3.2, except for a change in the bedrock elevation boundary condition (BED simulation), geothermal forcing (GHF simulation), and climate forcing (ERA simulation). Furthermore, another set of simulations is carried out to assess the influence of a different basal sliding model, the use of a different hybrid scheme and a

SIA-only model, and uncertainties in other model parameters on the modelled ice shelf BMB and ice-sheet geometry. A summary of these sensitivity experiments is provided in Table 3.2.

Influence of horizontal grid resolution

The computational expenses of the long-term, continental-scale simulation presented in Section 3.3.1 remain very high due to its relatively high horizontal resolution, and thus it is of interest to assess the influence of using a coarser, more viable model grid on the BMB estimates.

Figure 3.3 shows a comparison of the retrieved basal melting and freezing rates at grid resolutions of 10 (REF experiment), 20, and 40 km (henceforth GR20 and GR40, respectively). On the one hand, GR20 shows a strong similarity to REF, displaying only minor discrepancies mostly occurring in the proximity of grounding lines due to the smoothing effects of a coarser grid, which locally amplify melting and freezing beneath ice shelves (e.g., in the Larsen D and Amery ice shelves). On the other hand, GR40 exhibits the pronounced effects of a much coarser grid resolution in the form of considerably larger zones of melting and freezing zones. Although in some areas the retrieved BMB of ice shelves seems to be nearly insensitive to a 4-fold decrease in resolution to each horizontal direction (e.g., the Bellingshausen and Amundsen Sea sectors), there are areas where melting predicted by the reference run REF is alternated by freezing in GR40 and vice versa. An example of such resolution-induced artefacts is the Amery ice shelf, where the area of high basal melting predicted near the grounding line by REF and GR20 has extended towards the ice shelf front in GR40, overtaking the freezing zone detected at higher resolutions. In addition, new spots of strong accretion are retrieved, especially under big ice shelves and to the north of the Antarctic Peninsula. Interestingly, a few ice sheet sectors in GR40 display inverted patterns relative to those predicted by higher-resolution simulations. For example, the Moscow University ice shelf shows a predominant melting, whereas an accretion prevails beneath the Cook East ice shelf, showcasing the strong effects of a very coarse grid resolution.

The use of a finer model grid improves the agreement between our BMB estimates and those of Rignot et al. (2013) and Depoorter et al. (2013) (Table 3.2 and Supplementary Materials), which we attribute to a more localised (i.e. smaller area per grid cell) adjustment of basal melt rates and thus a reduced amplification of their estimated values near

grounding lines, together with a more accurate representation of small-scale features in the modelled ice influx from the grounded ice sheet. Consequently, we expect that the use of grid resolutions higher than our reference resolution (10 km) will further reduce these discrepancies. Our analysis suggests that the use of grid resolutions coarser than 20 km produces melting/freezing patterns and magnitudes that disagree with the results of higher resolution experiments and observation-based estimates, potentially leading to strong biases in ice-sheet simulations. Based on the good agreement between GR20 and REF, a resolution of 20 km is used in some of the numerous sensitivity tests presented in the next sections to reduce the computation time (see Table 3.2).

Influence of the input data sets

As described in Section 3.2, the experiments presented in this paper use the BEDMAP2 data set as a reference topography against which the basal ice-shelf melting and freezing rates are calibrated. Here, we run a 20-km resolution experiment (henceforth BED) where the bed topography is perturbed within the estimated uncertainty bounds (Fretwell et al., 2013) to assess potential impacts of such uncertainties on the retrieved BMB estimates. The perturbed bedrock is obtained by adding a randomly computed fraction of the uncertainty in the BEDMAP2 data set to the reference topography (independently for each data grid point). The perturbation map has been smoothed in order to eliminate small-scale perturbations (below 100 km) that tend to introduce numerical instabilities due to artificially strong horizontal gradients. Differences between the reference and the resulting perturbed bedrock topography (Figure 3.4a) reach up to ~ 500 m, with the largest discrepancies occurring mostly in the areas of East Antarctica where the BEDMAP2 data set is based on gravimetric data only (Fretwell et al., 2013). Compared to the experiment GR20, which is used here as a reference, the resulting ice-sheet equilibrium state has a smaller average absolute ice thickness error of 29.2 m (Table 3.2). This is due to a reduced overestimation of the modelled ice thickness over mountain ranges that we attribute to an enhanced ice drainage by new ice streams forming in areas where the bedrock topography has been lowered. This increment in the ice flow near the ice-sheet margins is also reflected in the new areas of ice-thickness underestimation (relative to GR20) surrounding the mountain ranges. An additional ice transport towards ice shelves increases the total ice-shelf BMB to a steady-state value of $-2282 \, \text{Gt} \, \text{a}^{-1}$, comparable to that of the GR40 simulation (Table 3.2), further demonstrating the strong impacts of the uncertainties in
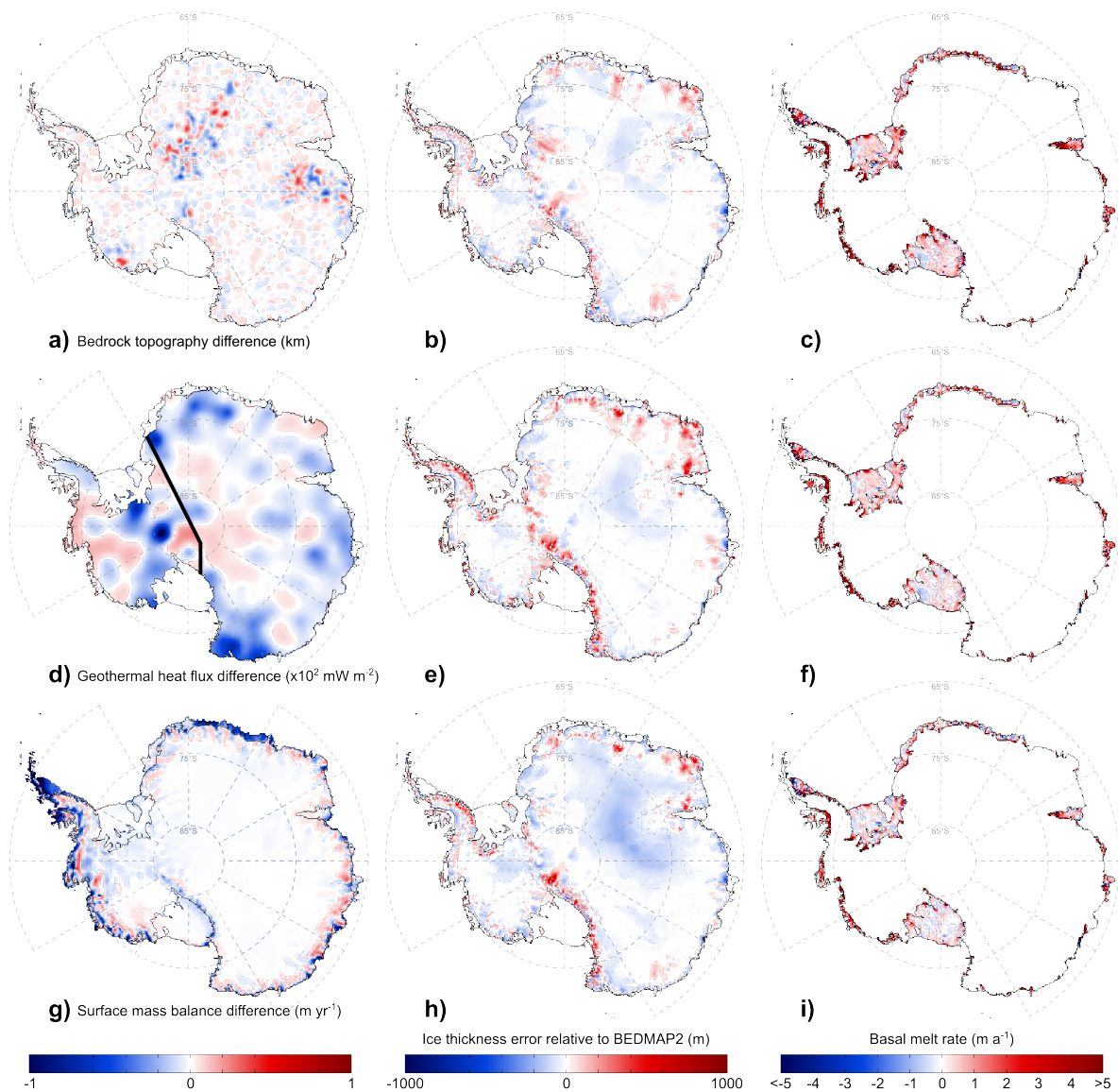
Figure 3.4: Results of experiments utilising a perturbed BEDMAP2 bedrock topography based on the uncertainty estimates of Fretwell et al. (2013) (top row), a two-valued geothermal heat flow distribution of Pollard and DeConto (2012b) (mid row), and the climate forcing from the ERA-Interim reanalysis (bottom row; Dee et al., 2011). Thick black line in d) represents the assumed division between East and West Antarctica. Left column shows the differences between the fields implemented in the above sensitivity tests and the REF experiment. Ice thickness errors relative to BEDMAP2 (mid column) and estimated basal melting and freezing rates (right column) as in Figs 3.2 and 3.1, respectively.

the topographic data on the estimated ice-shelf basal melting and freezing rates.

To test the influence of the uncertainties in the geothermal heat flux forcing, we perform a 20-km resolution experiment (henceforth GHF) featuring one of the simplest distributions commonly used in Antarctic ice-sheet simulations (e.g., Pollard and DeConto, 2012b). In this simulation we adopt two different values for West and East Antarctica, a lower value of $54.6\,\mathrm{mW\,m^{-2}}$ under the East Antarctic ice sheet, and a higher value of $70.0\,\mathrm{mW\,m^{-2}}$ across

West Antarctica. In contrast to the BED simulation, the GHF experiment produces an average absolute ice thickness error of 34 m, which is close to that of GR20. Interestingly, the predicted total ice-shelf equilibrium BMB amounts to $-1468\,\mathrm{Gt\,a^{-1}}$ and increases to $-1742\,\mathrm{Gt\,a^{-1}}$ when the observed ice-thinning rates are considered, which falls within the error bounds estimated by Rignot et al. (2013). Such decrease in the total BMB is explained by a comparatively lower geothermal heat flux (relative to Fox Maule et al. (2005) in REF) in such areas as those located upstream of the Ross West and Ronne ice shelves in West Antarctica, and most of the ice-stream locations along the East Antarctic coast (Figure 3.4d). In these areas, the use of lower values of geothermal heat flux decreases the sliding potential of ice streams feeding the ice shelves, thereby reducing ice velocities and generating lower ice-shelf basal melting rates near the grounding lines. Similar to the bedrock topography, uncertainties in the geothermal heat flux forcing strongly impact the retrieved basal melting and freezing rates under ice shelves, which compensate for the differences in the predicted mass flux across the grounding line.

Finally, the climate forcing from the ERA-Interim reanalysis (Dee et al., 2011) is used in a 20-km resolution experiment (henceforth ERA) to test the influence of the uncertainties in the surface mass balance on the retrieved sub-shelf melting and freezing rates. The averaged precipitation rates and near-surface temperatures are computed over the same period as the RACMO data (1979–2010) used in the REF experiment. A generally lower ice-sheet surface mass balance in the ERA-Interim data set relative to RACMO (Figure 3.4g) generates vast areas of an ice thickness underestimation, particularly in East Antarctica (Figure 3.4h), producing a mean absolute ice thickness error of 44.3 m. In addition, the reduced ice accumulation generates lower ice-shelf basal melting rates, which are similar to the estimates from the higher-resolution REF experiment. Thus, in ERA more wide-spread accretion zones decrease the total ice-shelf steady-state BMB to a value of $-1687.5\,\mathrm{Gt\,a^{-1}}$. As described in Section 3.2.2, the RACMO model is forced at its boundaries by the ERA-Interim reanalysis, and therefore the discrepancies between the ERA and GR20 experiments can be largely attributed to the regional, polar-oriented features implemented in RACMO. The higher resolution of RACMO allows for better resolved topographic gradients and circulation patterns, which may be critical for the simulation of such processes as, e.g., the drifting snow transport (Lenaerts et al., 2012). Despite these discrepancies, the differences between the ERA-Interim and RACMO data sets are small compared to the outputs of general circulation models (e.g., Agosta et al.,

2015). Based on our results, we expect that model initialisation procedures driven by climate forcing from a variety of general circulation models would produce essentially different results in order to compensate for the discrepancies between the model-based climate data sets. An analysis of the differences between the resulting ice sheet model initialisations may provide insights into potential internal biases of these climate forcing data sets. However, such analysis is beyond the scope of this study and is therefore deferred to future work.

Influence of the model formulation and parameters

As a complement to the simulations exploring the uncertainties in the input data sets, we present the results of experiments that aim to assess the influence of model complexity and model parameter choices on the inferred ice shelf BMB. The hybrid combination of the SIA and SStA velocities presented in Section 3.2 (Eq. 1) is a result of an original scheme formulation guided by our previous study (Bernales et al., 2017a), where we compared the performance of different hybrid schemes during the calibration of an Antarctic ice sheet model. Among the tested hybrid combinations, the scheme based on the idea of Bueler and Brown (2009) (henceforth HS-B) performed well in terms of the model fit to the observed ice-sheet thickness and ice velocities. However, HS-B showed a somewhat reduced ability to minimise the ice thickness errors in the continental interior of East Antarctica, because in this scheme the computation of the SStA velocities is mainly limited to the fast-flowing ice-sheet margins. We test the influence of the differences between our original scheme used in GR20 and HS-B by running a 20-km simulation using the latter. Our results show that these different hybrid schemes exhibit a similar performance in terms of ice thickness and ice velocities. The estimated ice-shelf basal melting and freezing rates from GR20 and HS-B are also in a good agreement, with some minor differences due to small discrepancies induced by the formation of isolated ice streams that produce a higher ice-shelf BMB of $-2094.2\,\mathrm{Gt\,a^{-1}}$ for HS-B. As shown by Bernales et al. (2017a), the differences between hybrid schemes are masked by the calibration of the basal sliding coefficients. Since our computation of the ice-shelf BMB depends on the ice flux from the grounded ice sheet sectors (and not on specific values of basal sliding coefficients), the results are only affected by the discrepancies between the modelled ice thickness and velocity fields from both schemes.

In (Bernales et al., 2017a) we also compared the performance of different hybrid schemes

versus a scheme that uses only the SIA to model the grounded ice sectors (i.e. the SSA is used exclusively for the ice shelves) during the calibration of an Antarctic ice sheet model, showing that the latter approach produces larger misfits between the observed and modelled ice-sheet thickness and ice surface velocities, especially near ice-sheet margins. Here we complement our sensitivity analysis by a comparison with this simpler approximation of the force balance equations, by performing an additional 20-km resolution experiment (henceforth SoS) using the above-mentioned SIA-only scheme. The increased mean absolute ice thickness error of $48.8\,m$ (Table 3.2) obtained from this experiment is accompanied by an even larger degradation of the estimated melting and freezing rates beneath ice shelves, producing a total steady-state BMB of $-2843.9\,\mathrm{Gt\,a^{-1}}$. Among all the experiments carried out in this study, the use of a SIA-only scheme for the grounded ice sectors has the largest impact on the retrieved ice-shelf BMB, stressing the need for a realistic treatment of the rapidly flowing ice sheet sectors, where the SIA is no longer valid.

In this study, we ensure a good agreement between the modelled and observed ice-sheet thickness through the calibration of basal sliding coefficients that enter our reference sliding law. In this sliding model (see Bernales et al., 2017a, Eq.2–6), basal velocities are assumed to be proportional to the third power of the basal shear stress ($n = 3$), but in principle other choices are possible. For example, the sliding model of Pollard and DeConto (2012b) uses a weaker non-linear relation ($n = 2$) during the calibration of the basal sliding coefficients. Here we test the influence of such change in the sliding law on our results by performing a 20-km resolution simulation (henceforth SLD) using the set-up of Pollard and DeConto (2012b), i.e. $n = 2$. The resulting ice-sheet thickness distribution is very similar to that from the GR20 experiment, with a slightly smaller mean absolute error of $32.8\,m$ (Table 3.2) due to reduced ice thickness underestimations near ice sheet margins. Similarly, the estimated ice-shelf steady-state BMB of $-2074\,\mathrm{Gt\,a^{-1}}$ in the SLD simulation is slightly higher by absolute value, due to locally higher ice-stream velocities in certain areas such as those found upstream of the Crosson and Dotson ice shelves. The similarity between our SLD and GR20 experiments suggests that a calibration of basal sliding coefficients can be, in principle, applied to any smoothly varying relation between the basal shear stress and the sliding velocities (Pollard and DeConto, 2012b).

Finally, our REF experiment uses a default value of $E_{\mathrm{SSA}} = 0.5$ for the ice flow enhancement factor for ice shelves, which falls within the range of values commonly used in Antarctic ice-sheet simulations (0.3–1.0, e.g., de Boer et al., 2015). The use of

this value results in ice-shelf velocities that are locally underestimated compared to the observational data set of Rignot et al. (2011), as shown in Figure 3.2. Here, we test larger enhancement factors to assess their impacts on the modelled ice-shelf velocities and basal melt rates, including $E_{\mathrm{SSA}} = 1$, $E_{\mathrm{SSA}} = 2$, and $E_{\mathrm{SSA}} = 3$ (Table 3.2). Compared to the REF experiment, the use of larger values of E_{SSA} increases the internal ice-shelf flow, thereby reducing the basal melt (particularly near grounding lines) needed to compensate for the accumulation in areas where the ice shelves receive a high ice flux from the grounded ice sheet sectors. Furthermore, an increasingly faster ice-shelf flow in this series of simulations reduces the misfit between the modelled and observed ice surface velocities, from $40\,\mathrm{m\,a^{-1}}$ in the REF simulation, to $37\,\mathrm{m\,a^{-1}}$ ($E_{\mathrm{SSA}} = 1$), $34\,\mathrm{m\,a^{-1}}$ ($E_{\mathrm{SSA}} = 2$), and $32\,\mathrm{m\,a^{-1}}$ ($E_{\mathrm{SSA}} = 3$). Overall, the use of larger ice-shelf enhancement factors generates smaller total BMB estimates that are closer to those of Rignot et al. (2013) and Depoorter et al. (2013). Following the assumption that the ice flow enhancement factor for ice shelves should be ≤ 1 (Ma et al., 2010), no special treatment of ice anisotropy in ice shelves ($E_{\mathrm{SSA}} = 1$) provides the best fit between our results and the cited studies. Since the same value is used across the grounded ice sheet sectors ($E_{\mathrm{SIA}} = 1$, following the sensitivity analyses of Pollard and DeConto (2012b) and Bernales et al. (2017a)), we have concluded that this tuning parameter can be excluded from our particular model set-up.

We have also performed a series of experiments testing the influence of other model parameters (Table 3.2), such as: 1) degree-day and lapse-rate correction factors in the surface mass balance model, ranging from 3 to $15\,\mathrm{mm\,day^{-1}\,^\circ C^{-1}}$ for the former, and 6 to $10\,^{o}C$ for the latter, and 2) the parameters related to the iterative adjustment of the ice-shelf basal melting and freezing rates (Eq. 3). For our particular model set-up driven by the present-day climate forcing, these experiments have not shown any significant sensitivity to the tested parameter variations.

3.4 Summary and conclusions

This study presents equilibrium estimates of basal melting and freezing rates for the entire Antarctic ice-shelf system derived from an ice sheet-shelf model and present-day observations of the ice sheet geometry. Our method is a model-based extension of the techniques presented in recent studies using the observed ice velocities and ice thickness to infer the ice shelf BMB. In contrast, we derive the ice flow directly from an ice-sheet

model calibrated against the ice thickness observations and validated against the observed surface velocity field (Bernales et al., 2017a). This approach allows for a detailed analysis of the BMB of ice shelves that are required by continental-scale, long-term ice-sheet models to reproduce the present-day geometry of the floating ice sheet sectors. Our estimates complement previous glaciological and oceanographic reconstructions of the BMB of the Antarctic ice shelves.

The retrieved distribution of basal melting and freezing rates represents a total BMB steady-state estimate of -1648.7 Gt a^{-1}, that increases to -1917.0 Gt a^{-1} when the observational ice-shelf thinning data from Pritchard et al. (2012) are included. Our results exhibit similar patterns to those found by the observation-based study of Rignot et al. (2013). In agreement with their reconstruction, we identify the highest ice-shelf basal melting rates near grounding lines and ice shelf fronts, extensive accretion zones in-between under the biggest ice shelves, and high melting rates along the East Antarctic coasts suggesting that ocean thermal conditions there are similar to those detected in the Amundsen and Bellingshausen Sea sectors.

Additional experiments reveal that the use of a lower horizontal grid resolution tends to amplify the retrieved basal melting, thereby causing a significantly larger ice mass loss from the Antarctic ice shelves. Since the misfit between our BMB estimates and those from the observational studies is reduced when an increasingly higher model resolution is employed, we anticipate that the use of even higher grid resolutions would further improve the agreement between the model-based estimates and the observational data.

Our estimates are insensitive to variations in the parameters controlling the iterative adjustment of the ice-shelf basal melting and freezing rates, and to changes in the degree-day and lapse-rate correction factors in the implemented surface mass balance model. Similarly, variations in the basal sliding law and hybrid scheme formulation used to compute the grounded-ice velocities do not impose any significant changes in the predicted BMB of ice shelves. A choice of a flow enhancement factor larger than our reference value of 0.5 decreases the estimated basal melt rates near grounding lines and the misfit between the observed and modelled ice surface velocities of large ice shelves, showing that a value of $E_{\mathrm{SSA}} = 1$ (i.e. no scaling of the ice-shelf flow) produces a total BMB estimate that is closer to the values obtained by Rignot et al. (2013) and Depoorter et al. (2013). Our experiments also show that uncertainties in the input data sets (topography, geothermal heat flux, and climate forcing) hold the potential to strongly impact the retrieved ice-shelf

basal melting and freezing rates by, for example, altering the ice flow patterns from the ice sheet interior to its margins, and thus modifying the amount of ice mass that is routed towards the ice shelves across the grounding line.

Our model-based estimates reproduce well the complexity of the BMB of the Antarctic ice shelves, suggesting a strongly heterogeneous distribution of sub-shelf melting and freezing rates required by our model to fit the observed Antarctic ice shelf geometry. Although these results cannot be directly implemented in freely evolving simulations with varying boundary conditions, they can be used as a first-order approximation to guide the development of effective parameterisations of the ice-ocean interaction for large-scale, long-term, prognostic modelling experiments.

Context

Subglacial sliding conditions under the grounded ice sheet sectors and basal regimes under ice shelves reconstructed in Chapters 2 and 3 provide two boundary conditions which are essential for modelling experiments of the Antarctic ice sheet-shelf system. Due to large uncertainties in these conditions linked to the lack of direct observational constraints, ice sheet models have traditionally relied on over-simplified parameterisations of subglacial processes that introduced biases and compensation of errors in modelling experiments in order to fit a range of observed ice sheet characteristics. Even with the approaches discussed in previous chapters, the inferences of subglacial conditions are still susceptible to this problem due to the assumed negligible influence of the uncertainties and errors in other components on the ice sheet model. For example, the present-day climate forcing is assumed to be perfectly representative of the internal state and surface mass balance of the present-day Antarctic ice sheet. Yet, it is well established that the thermal and dynamical states of the ice sheet are still affected by the cold conditions of the last glacial cycle, the subsequent continuous climate warming and the ice marginal retreat since the Last Glacial Maximum. Leaving aside the non-equilibrium ice sheet state, even the assumption of a perfectly resolved present-day climate conditions across Antarctica is not well justified, since the forcing used in the ice sheet simulations presented above is obtained from either a regional climate model or a climate reanalysis, which locally disagree with in situ measurements from automated weather stations.

Regardless of the growing number of available observations, climate conditions in polar regions are still subject to large uncertainties, which impact model-based reconstructions of the subglacial regimes. These uncertainties increase exponentially when ice sheet modelling experiments concern past or future periods, for which observational data are scarce or non-existent. As a result, such ice sheet modelling experiments often take advantage of the outputs of global circulation models. It is however known that global circulation models struggle while trying to reproduce the present-day climate conditions across Antarctica

and often suffer from a very low spatial resolution (Agosta et al., 2015). In this context, the following chapter —built upon the methods and results presented in the two previous chapters— investigates and quantifies the impacts of biases in the atmospheric forcing from global circulation models on the modelled dynamics of the Antarctic ice sheet-shelf system. The performance of ten global circulation models is assessed using ice sheet modelling experiments, which are simultaneously validated against observations of the ice sheet geometry, ice flow velocity, and basal regimes of ice shelves.

Chapter 4

Evaluating climate models over Antarctica using an ice sheet model

Chapter Abstract

Model-based reconstructions and predictions of past and future ice sheet changes require the use of large-scale climatological data sets that are commonly obtained from coupled atmosphere-ocean global circulation models. However, the suitability of different global circulation models for providing such input has not yet been evaluated. In particular, it remains unclear whether these models are capable of simulating polar climate conditions in a realistic fashion and to which extent dissimilarities in climate model outputs affect the modelled ice sheet dynamics. In this context, we test the performance of 10 climate data sets from different global circulation models against the equivalent fields from the ERA-Interim reanalysis and the regional climate model RACMO. We use the forcing data sets to drive ensemble steady-state simulations of the Antarctic ice sheet under present-day conditions. Using an iterative technique to infer largely unknown basal conditions under the ice sheet, we demonstrate that large biases in the climate forcing can be erroneously compensated by the calibration of internal ice-sheet model parameters. These biases cannot be identified when the ice-sheet model performance is evaluated only in terms of total ice volume and ice distribution. In contrast, a simultaneous evaluation of the modelled fields against observation-based ice thickness, velocity and basal mass balance data helps to detect these biases before they leak into reconstructions of past ice sheet states and projections of the future climate variability.

4.1 Introduction

Ice sheets are among the most uncertain factors in projections of future climate variability, despite of their largest potential contribution to sea-level rise (Church et al., 2013) and their important role in triggering local and global feedback processes within the atmosphere-ocean system across a wide range of temporal scales (Vizcaíno, 2014). Previous international initiatives aiming to improve the understanding of the past, present, and future climate changes, such as the Coupled Model Intercomparison Project (CMIP) and the Paleoclimate Modelling Intercomparison Project (PMIP), have excluded the use of dedicated ice-sheet models due to lack of confidence in their ability to represent key processes affecting the ice dynamics over short (sub-centennial) timescales (e.g. Meehl et al., 2007). Recent advances in ice-sheet modelling and the results of model intercomparison studies within the glaciological community (e.g. Pattyn et al., 2012, 2013) have prompted an inclusion of such models in the experimental design of the latest phase of the CMIP (CMIP6, Eyring et al., 2016), in the form of the Ice Sheet Model Intercomparison Project (ISMIP6, Nowicki et al., 2016). The primary goal of the ISMIP6 is to better understand the evolution of polar ice sheets under changing climate conditions.

Predicting the responses of ice sheets to potential future climate variations is challenging, in particular due to large uncertainties in the internal model parameters and the need for the use of external forcing obtained from too coarse model-based data sets (e.g. precipitation rates, near-surface air temperatures, and ocean temperatures). This is because such input data are typically generated by low-resolution atmosphere-ocean global climate models (AOGCMs), which are known to differ significantly and often disagree with observations, reanalysis data, and regional climate models, especially in polar regions (e.g. Agosta et al., 2015). Thus, there is a pressing need for assessing the suitability of AOGCM outputs for applications in ice sheet model experiments, and quantifying the significance of dissimilarities between these models and higher resolution data sets validated versus present-day observations. Such assessment would eventually allow for an identification of biases in both climate and ice sheet models, representing a critical step towards an inclusion of ice-sheet–climate feedbacks in Earth-System models.

Here, we present an evaluation of the CMIP5 climate model outputs from 10 AOGCMs (Taylor et al., 2012) using numerical simulations of the Antarctic ice sheet. This evaluation builds upon a one-to-one comparison of ice sheet simulations driven by reanalysis data, the results of polar-oriented high-resolution regional climate simulations, and AOGCM

outputs. Our experiments focus on the initialisation phase of an ice-sheet model under the present-day conditions, including the calibration of the model parameters related to basal conditions (Bernales et al., 2017a,b). By providing insights into the sensitivity of the ice-sheet configuration to differences between climate model products, this study aims to answer the following questions:

- How different is the performance of AOGCMs across Antarctica compared to reanalyses and RCMs?

- To what extent can the uncertainty in the ice-sheet model parameters compensate for inaccuracies in the model-based climate forcing?

- How do different model-based climate forcings impact the fit between ice-sheet model and observational data?

First, we describe the ice-sheet model set-up and climate forcing (Sect. 4.2). Then we present the simulations driven by the reference forcing (reanalysis and RCM) and the AOGCMs outputs (Sect. 4.3), the results of which are discussed in Sect. 4.4 and summarised in 4.5 together with their implications for future work.

4.2 Methods

4.2.1 Experimental set-up

Our numerical experiments are performed using the ice sheet-shelf model SICOPOLIS (SImulation COde for POLythermal Ice Sheets, Sato and Greve, 2012) with the modifications described by Bernales et al. (2017a,b). The model implements a new hybrid approach to compute the ice velocity within the ice sheet (Bernales et al., 2017b) that allows for a smooth transition between the slow-moving ice in the continental interior, the fast-flowing ice streams at the ice sheet margins, and even faster moving ice shelves building upon the ideas of Bueler and Brown (2009) and Winkelmann et al. (2011). Thermodynamic conditions in the ice sheet are computed using a one-layer enthalpy scheme (Greve and Blatter, 2016).

Starting from the initial ice sheet geometry derived from BEDMAP2 (Sect. 4.2.2), the model is run forward in time over a period of 400,000 years (400 kyr). This is done with time-invariant boundary conditions until the thermal and dynamic equilibria are reached.

Our steady-state experiments do not account for the glacial isostatic rebound. Initial ice temperatures are homogeneously set to a value of $-10\,^{\circ}\mathrm{C}$, and evolve in response to the geothermal heat flux and air temperature forcing. The latter is modified to account for the differences between the modelled and reference surface topographies prescribed in AOGCMs using a homogeneous lapse rate correction of $-8\,^{\circ}\mathrm{C}\,\mathrm{km}^{-1}$. The corrected near-surface air temperatures are used in a positive degree-day model (Calov and Greve, 2005) to compute surface melting, with degree-day factors of 8 and $3\,\mathrm{mm}\,\mathrm{day}^{-1}\,^{\circ}\mathrm{C}^{-1}$ for ice and snow, respectively, and a standard deviation of the air temperature of $5\,^{\circ}\mathrm{C}$.

Each 400-kyr-long simulation use three previously documented methods to calibrate the modelled ice sheet (Bernales et al., 2017a,b), namely a) a relaxation technique for the evolution of the ice thickness in the entire domain in order to prevent artificial drifts due to spin-up of the ice temperatures within the ice sheet, b) an iterative adjustment of basal sliding coefficients to account for potential variations in the mechanical properties of the bedrock (e.g. rough rock vs. soft sediments) based on the idea of Pollard and DeConto (2012b), and c) an iterative estimation of the ice-shelf basal melting and freezing rates needed to maintain the ice shelves in equilibrium. The grounding line and ice-shelf fronts are kept at their modern observed positions to ensure a consistent calibration and evaluation against observational data (Bernales et al., 2017a,b).

4.2.2 Input data

The initial ice sheet geometry is based on the BEDMAP2 data set (Fretwell et al., 2013), including the present-day Antarctic ice thickness and bedrock topography derived from a compilation of millions of remote-sensed and in situ point measurements combined with digital elevation models. At the base of the modelled bedrock layer, the geothermal heat flux is prescribed based on the map of Fox Maule et al. (2005) derived from satellite magnetic data.

The climate forcing driving our reference experiments includes monthly precipitation rates and near-surface air temperatures from the ERA-Interim reanalysis (Dee et al., 2011) and the regional model RACMO2.3 (van Wessem et al., 2014), averaged over the period of 1979 to 2005 (Fig. 1). ERA-Interim is considered to be among the most accurate global reanalyses over the Antarctic continent (Bromwich et al., 2011; Bracegirdle and Marshall, 2012), and it is also used to force RACMO2.3 at its boundaries, which is specifically adapted for polar regions and has been validated against in situ observations of the Antarctic
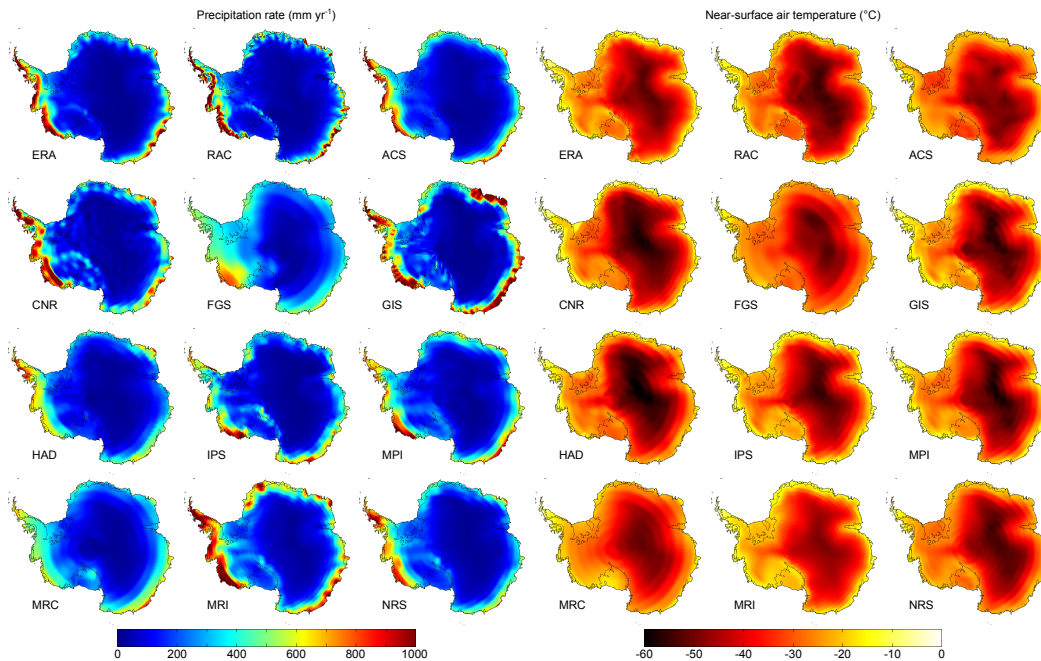
Figure 4.1: Mean-annual precipitation rates (left) and near-surface temperatures (right) from each forcing data set, in $\mathrm{mm\,yr^{-1}}$ and °C, respectively. Codenames as in Table 4.1.

surface mass balance (van Wessem et al., 2014). These data sets are used as a reference forcing against which the performance of the atmospheric fields from AOGCMs is evaluated. This study utilises outputs from 10 AOGCMs that participated in the first realisation of the CMIP5 historical experiment including ACCESS1-3, CNRM-CM5, FGOALS-g2, GISS-E2-R, HadCM3, IPSL-CM5A-LR, MIROC-ESM, MPI-ESM-P, MRI-ESM1, and NorESM1-M (Figure 4.2).

All data sets have been projected onto a common polar stereographic horizontal grid with a resolution of 20 km, containing 601×601 equidistant grid points and covering the entire Antarctic continent. The vertical grid includes 81 points within the ice sheet densifying towards its base and 41 points within the lithospheric thermal layer. The choice of this resolution is a compromise between computational expenses and model performance (Bernales et al., 2017a,b).

4.3 Results

As described in Sect. 4.2, the two reference forcings from ERA-Interim and RACMO2.3 (henceforth ERA and RAC), and the forcings from 10 AOGCMs are used to drive equilibrium simulations of the Antarctic ice sheet under the present-day conditions. At the end

Table 4.1: Summary of the equilibrium results for each forcing, including the total grounded and floating ice volumes, V_{grd} and V_{flt}, respectively, the mean absolute ice thickness error for grounded and floating areas, $\overline{\Delta H}_{\text{grd}}$ and $\overline{\Delta H}_{\text{flt}}$, respectively, the mean surface velocity error, $\overline{\Delta v}_{\text{s}}$, and the basal mass balance and area-averaged basal melt rates of ice shelves, BMB_{flt} and $\overline{\text{BMR}}_{\text{flt}}$, respectively, in water equivalent.

Forcing	Code	V_{grd} (km^3)	V_{flt} (km^3)	$\overline{\Delta H}_{\text{grd}}$ (m)	$\overline{\Delta H}_{\text{flt}}$ (m)	$\overline{\Delta v}_{\text{s}}$ (m yr^{-1})	BMB_{flt} (Gt yr^{-1})	$\overline{\text{BMR}}_{\text{flt}}$ (m yr^{-1})
ERA-Interim	ERA	2.53×10^7	7.06×10^5	49.7	1.2	47.5	-1687.5	1.1
RACMO2.3	RAC	2.56×10^7	7.06×10^5	37.9	1.3	49.1	-1907.9	1.2
ACCESS1-3	ACS	2.56×10^7	7.06×10^5	40.2	0.8	47.0	-2099.7	1.4
CNRM-CM5	CNR	2.57×10^7	7.06×10^5	46.2	1.3	53.3	-1019.6	0.7
FGOALS-g2	FGS	2.59×10^7	7.07×10^5	42.3	0.7	60.2	-2668.5	1.7
GISS-E2-R	GIS	2.55×10^7	7.07×10^5	47.8	1.6	60.8	-2250.0	1.5
HadCM3	HAD	2.57×10^7	7.06×10^5	42.4	1.1	47.6	-1719.9	1.1
IPSL-CM5A-LR	IPS	2.53×10^7	7.06×10^5	51.5	1.2	48.5	-1669.1	1.1
MIROC-ESM	MRC	2.35×10^7	7.05×10^5	211.6	2.0	52.9	-949.7	0.6
MPI-ESM-P	MPI	2.57×10^7	7.06×10^5	36.8	1.1	53.6	-2127.8	1.4
MRI-EMS1	MRI	2.56×10^7	7.06×10^5	36.7	1.6	63.8	-1796.6	1.2
NorESM1-M	NRS	2.56×10^7	7.06×10^5	49.8	0.8	47.5	-2174.8	1.4

of each 400-kyr-long experiment, iteratively adjusted basal conditions under the ice sheet (sliding coefficients) and ice shelves (melting/freezing rates) produce an equilibrium ice sheet-shelf configuration that minimises the misfit between the modelled and observed ice thickness. In addition, we compare the resulting surface ice velocity fields to the observational data set of Rignot et al. (2011). Table 4.1 presents a summary of the results for each experiment, including the codenames used henceforth for each AOGCM and the corresponding ice sheet simulation. Here, we first present the results of the simulations driven by the reference forcing from ERA and RAC (Sect. 4.3.1), followed by the results from the experiments driven by the AOGCM forcing (Sect. 4.3.2).

4.3.1   Reference experiments

The total equilibrium grounded ice volumes from the ERA and RAC experiments equal to 2.53×10^7 and $2.56 \times 10^7 \, \text{km}^3$, respectively, with the latter deviating from the reference BEDMAP2 value by only 0.1%. Total floating ice volumes from both experiments deviate from the reference value of $7.07 \times 10^5 \, \text{km}^3$ by less than 0.2% (Table 4.1). When evaluating the resulting ice distribution against the ice thickness from BEDMAP2, the differences between the modelled and observed grounded ice thickness (Fig 4.2) yield mean absolute errors of $\sim 50 \, \text{m}$ for ERA and $\sim 38 \, \text{m}$ for RAC. A larger error in the ERA simulation can be mostly attributed to an underestimation of the ice thickness in East Antarctica which is caused by lower precipitation rates than in the RACMO2.3 data set (Fig. 4.1), since
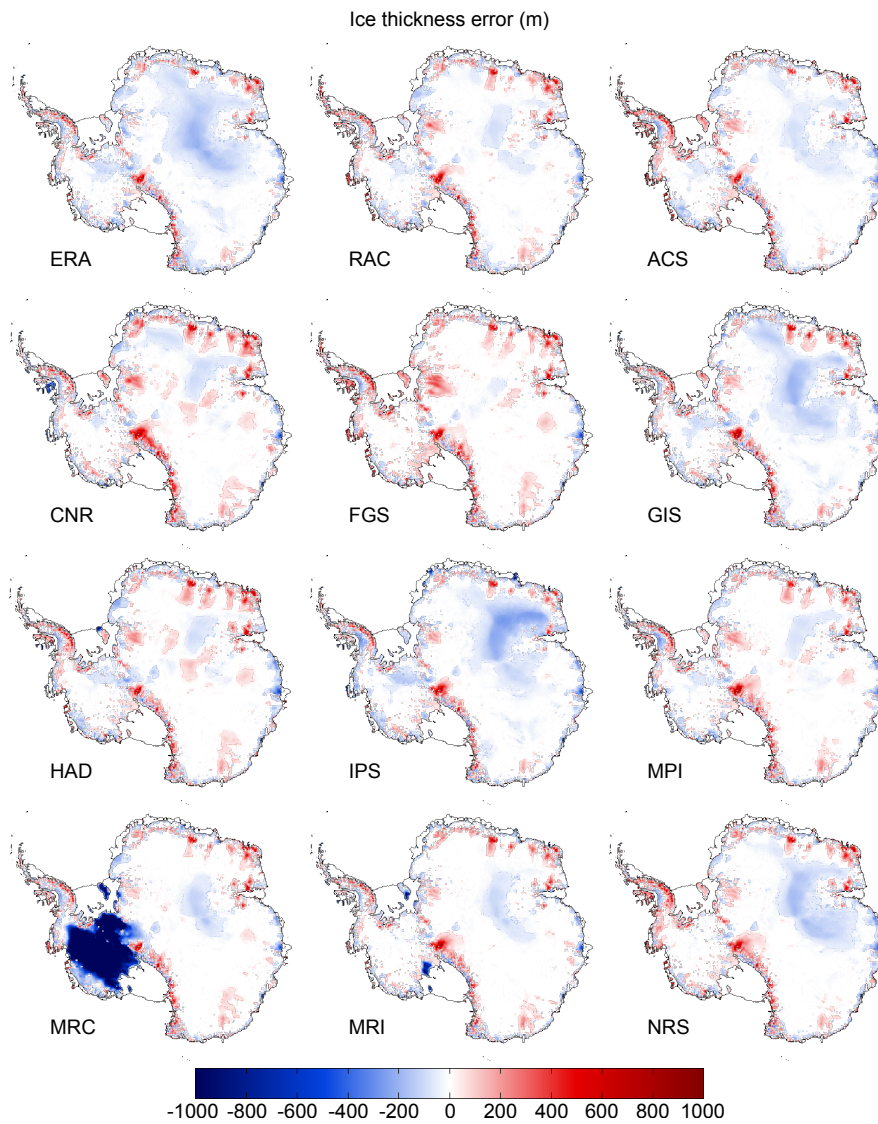
Figure 4.2: Ice thickness error for each experiment, in metres. Codenames as in Table 4.1.

both experiments exhibit similar results elsewhere. The thickness of the floating ice sectors is in a close agreement with observations in both simulations as a result of the iterative adjustment of basal melting and freezing rates (Sect. 4.2). Here the mean absolute errors in both ERA and RAC experiments drop to $\sim 1\,\mathrm{m}$. The estimates of the ice-shelf basal mass balance (BMB) retrieved from the model calibration amount to $-1687.5\,\mathrm{Gt\,yr^{-1}}$ for ERA and $-1907.9\,\mathrm{Gt\,yr^{-1}}$ for RAC. This difference is caused by a combination of generally lower precipitation rates and higher air temperatures in the ERA-Interim data set (Fig. 4.1), that tend to generate lower basal melting rates and larger accretion zones beneath the ice shelves, especially around East Antarctica and the Antarctic Peninsula (Figure 4.3).
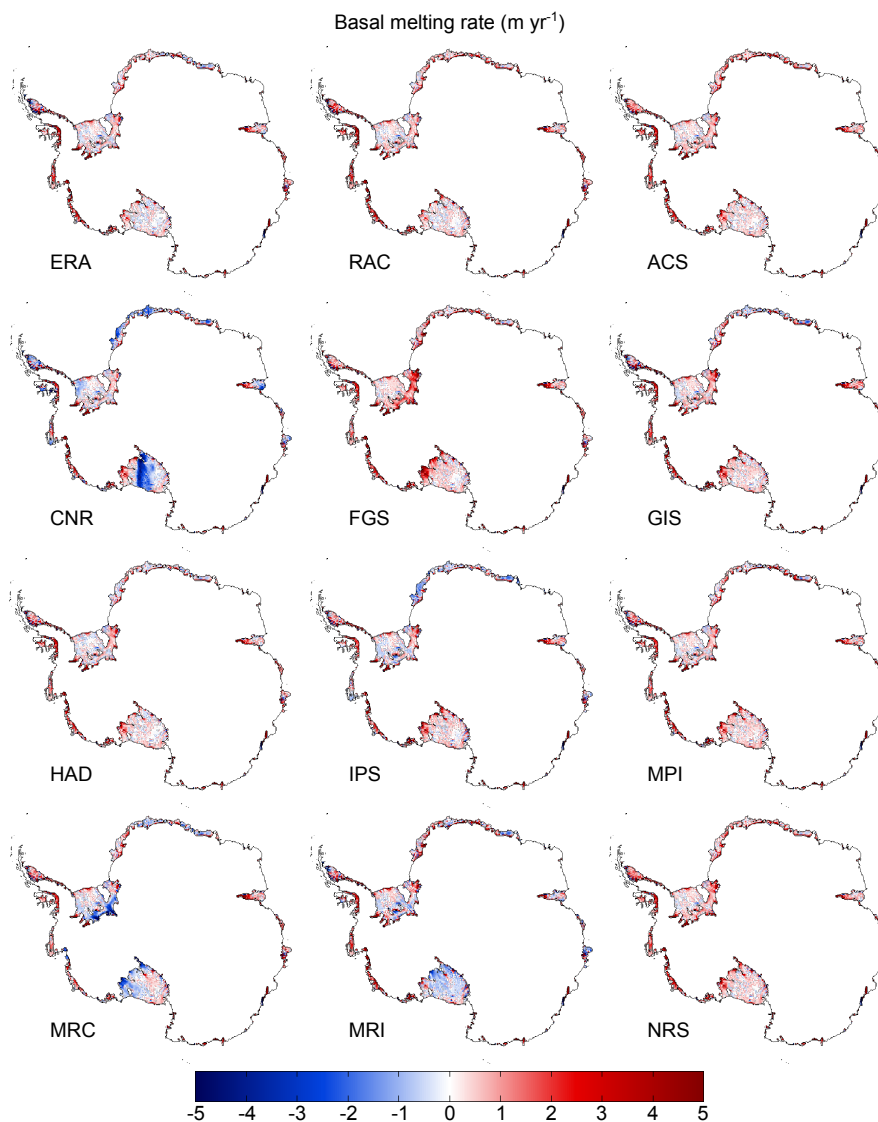
Figure 4.3: Basal melting and freezing rates for each experiment, in metres per year of ice equivalent. Codenames as in Table 4.1.

On the other hand, a good agreement between the modelled and observed grounded ice thickness is enabled by the iterative adjustment of the basal sliding coefficients (Sect. 4.2). The retrieved distributions of this parameter in the ERA and RAC experiments are similar in the Antarctic Peninsula and West Antarctic sectors, but diverge across East Antarctica (Fig. 4.4). Here, the ERA simulation predicts more extensive melting areas below the grounded ice sheet sectors (where sliding regimes can be calibrated). This is likely due to overall higher air temperatures and lower precipitation rates indicated by ERA-Interim as compared to RACMO2.3, increasing internal ice sheet temperatures and decreasing thermal insulation in the ice sheet sectors that feature underestimations of ice thickness.

Basal sliding coefficient (m Pa⁻¹ yr⁻¹)
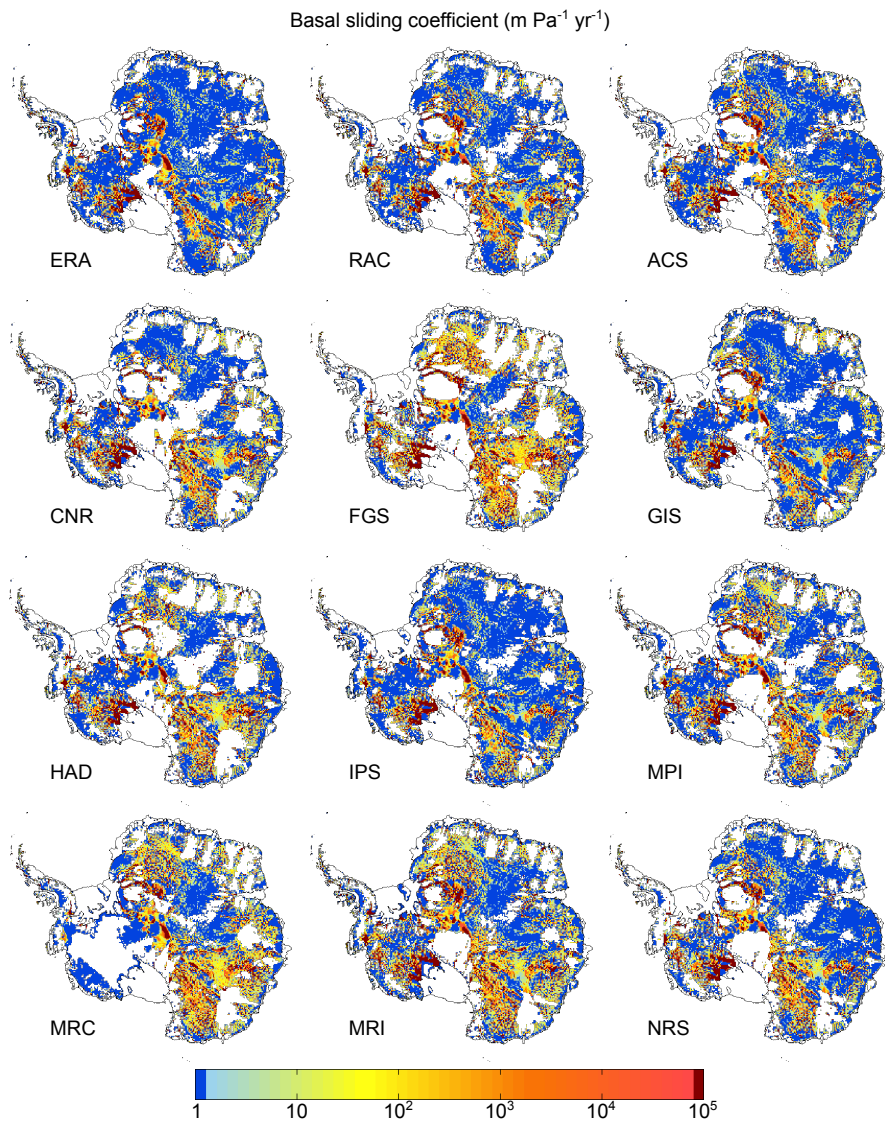
Figure 4.4: Basal sliding coefficients for each experiment, in $\mathrm{m\,Pa^{-1}\,yr^{-1}}$. Codenames as in Table 4.1.

Interestingly, in most of such areas predicted sliding coefficients reach the lower limit allowed by the calibration method, in an attempt to prevent a further underestimation of the ice thickness. The reduced potential for sliding in the ERA simulation has a direct impact on the modelled ice surface velocities (Fig. 4.5), which are noticeably lower across East Antarctica than in the RAC experiment, in contrast to very similar patterns reconstructed across West Antarctica and the Antarctic Peninsula. Although the fit between the modelled and observed ice thickness is better in the RAC experiment, the mean absolute velocity error (Table 4.1) is slightly lower in ERA, amounting to $47.5\,\mathrm{m\,yr^{-1}}$ vs. $49.1\,\mathrm{m\,yr^{-1}}$ produced by the RAC experiment. This can be attributed to the higher precipitation rates across the East Antarctic interior in the RACMO2.3 data set compared

Surface ice velocity ratios
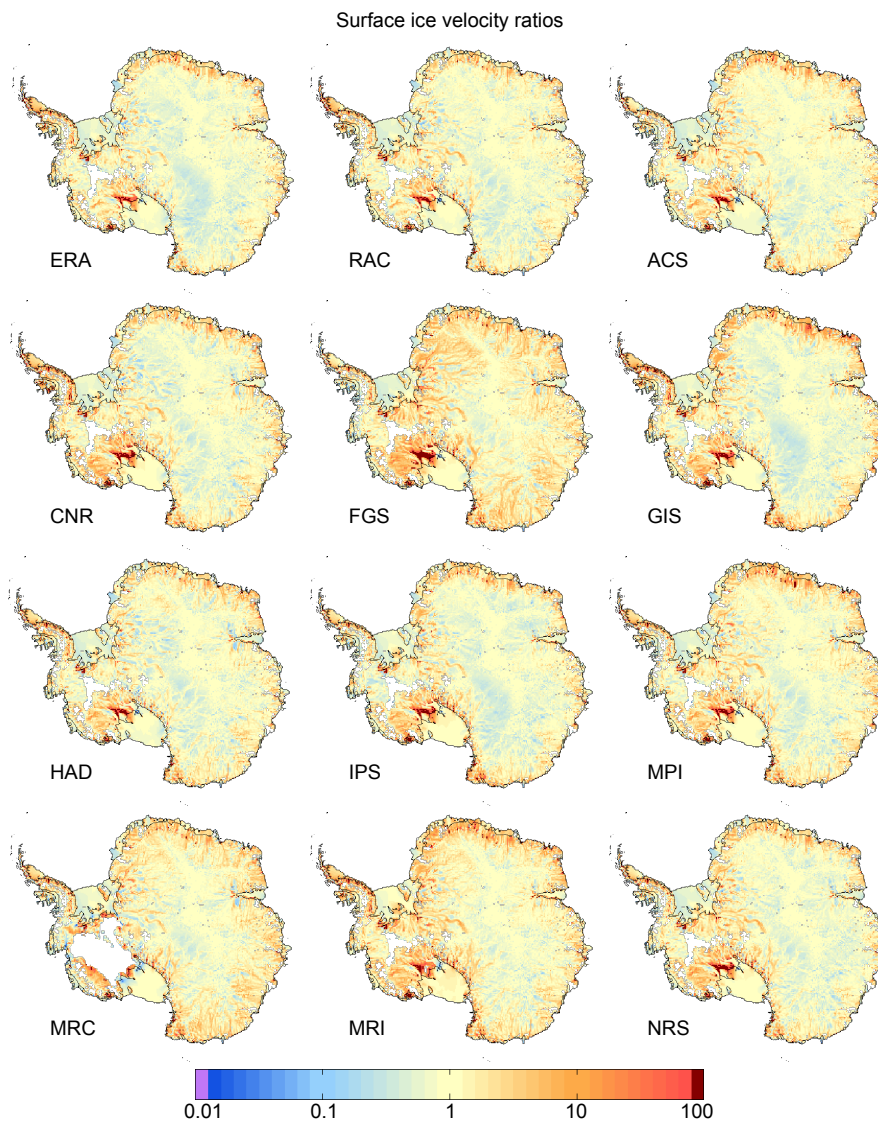
Figure 4.5: Surface ice velocity ratios for each experiment. Codenames as in Table 4.1.

to ERA-Interim, that causes faster ice flow velocities in order to remove the excess of ice accumulation.

4.3.2   Experiments driven by AOGCM forcing

Most AOGCM-driven experiments produce grounded ice volumes that deviate from the reference BEDMAP2 volume of $2.56 \times 10^7 \, \mathrm{km}^3$ by less than 1% (Table 4.1). Similarly, in most simulations the final ice shelf volumes are very close to the reference value of $7.07 \times 10^5 \, \mathrm{km}^3$. Such goodness of the model fit to observations can be attributed to the efficiency of the iterative adjustment of the basal sliding coefficients and BMB of ice shelves. The only exception is the MRC experiment that underestimates the grounded ice volume

by 8% and produces the largest deviation of 0.3% from the observed volume of floating ice. The latter can be however considered negligibly small when looking at the cause of the poor model performance. This cause becomes apparent when looking at the map featuring the differences between the modelled and observed ice thickness (Fig. 4.2) that shows that most of the West Antarctic ice sheet is gone in the MRC experiment, due to a combination of high near-surface air temperatures and low precipitation rates near the margins of the ice sheet (Fig. 4.1). This is regardless of a complete deactivation of basal sliding by the calibration method (Fig. 4.4). This simulation represents an especially interesting case, since the modelled ice geometries in East Antarctica and the Antarctic Peninsula closely resemble observations, with the model performance there being comparable to that of the reference runs. Furthermore, the MRC simulation manages to maintain observed-like ice shelves in West Antarctica, due to abundant ice flux from the East Antarctic ice streams, locally elevated precipitation rates, and the adjustment of the basal melting and freezing under the ice shelves (Sect. 4.2). However, the predicted expansion of the accretion zones and the magnitudes of freezing rates are highly unrealistic, especially close to the grounding lines and under smaller ice shelves that are observed melt rapidly from below (Rignot et al., 2013).

The equilibrium distributions of the grounded ice thickness from experiments driven by the AOGCM outputs (with the exception of the MRC experiment) agree well with the reference simulations, resulting in mean absolute errors that are below $\sim 50\,\mathrm{m}$ (Table 4.1). On the one hand, the GIS, IPS, and NRS experiments exhibit an underestimation of the ice thickness in East Antarctica resulting in the largest mean ice thickness errors, similar to the ERA simulation. On the other hand, the modelled ice geometries in the ACS, MPI, and MRI experiments resemble the results of RAC, producing the lowest total ice thickness errors. In contrast, the ice thickness distributions in the CNR, FGS, and HAD simulations represent a different case. Here, isolated zones of strong ice thickness overestimation tend to increase the misfit between the modelled and observed ice thickness, due to lower interior air temperatures (e.g. HAD) and/or higher precipitation rates (e.g. FGS). These overestimations of the ice thickness mostly occur in areas where low basal ice sheet temperatures do not allow for the calibration of the basal sliding coefficients (Fig. 4.4), whereas in the surrounding areas the calibration inflates the basal sliding to compensate for the excessive ice accumulation. The effects of the increased basal sliding clearly feature in the modelled surface ice velocities, especially in the FGS and MRI

experiments, that produce relatively low ice thickness errors at the expense of the higher velocity errors (Table 4.1).

The retrieved distributions of the sub-shelf melting and freezing rates derived from simulations driven by different AOGCM atmospheric forcings (Fig. 4.3) vary considerably depending on the chosen data set, regardless of the low mean absolute ice thickness errors (Table 4.1). On the one hand, notorious accretion zones which are mainly found beneath big ice shelves and along the coasts of East Antarctica feature in the CNR, MRC, and MRI experiments. In addition, the CNR simulation predicts additional accretion zones along the Antarctic Peninsula and under some smaller ice shelves. On the other hand, relative to the RAC experiment, we observe an overall increase in the estimated basal melting when the outputs from the FGOALS-g2 and GISS-E2-R models are used. However, this mostly occurs near the grounding lines of big ice shelves, whereas most other sectors are characterised by relatively lower melting rates. Total values of BMB range from $\sim -950\,\mathrm{Gt\,yr^{-1}}$ for MRC to $\sim -2668\,\mathrm{Gt\,yr^{-1}}$ for FGS, compared to $-1500 \pm 237\,\mathrm{Gt\,yr^{-1}}$ estimated by Rignot et al. (2013). Their respective area-averaged melting rates differ by a factor of 3, with 0.6 (MRC) and $1.7\,\mathrm{m\,yr^{-1}}$ (FGS), compared to $0.8\,\mathrm{m\,yr^{-1}}$ estimated by the cited study.

4.4   Discussion

Despite significant dissimilarities between the atmospheric fields provided by different AOGCMs, our experiments reveal an unexpectedly good performance overall for some of the key ice sheet quantities relative to observational data sets. One of such quantities is the total grounded ice volume, which is often used as a measure of the ice-sheet model performance (e.g. de Boer et al., 2015). In this study, deviations between our results and the reference grounded ice volume from the BEDMAP2 data set are minimised through adjustments of basal sliding coefficients. However, our results show that a good fit between the model and observations is enabled by the model calibration through a multitude of error cancellations. The adjustment of the sliding coefficients compensates for large biases in the forcing data sets, while enormous uncertainties in subglacial conditions prevent us from direct quantification of these cancelling errors. This result contradicts the conclusions of Pollard and DeConto (2012b), who attempted to quantify the robustness of the retrieved sliding coefficients to changes in a variety of model inputs, including

observation-based surface accumulation data, and found that regional-scale features were mostly insensitive to such changes. Although our experiments driven by two reference data sets from ERA Interim and RACMO2.3 show overall similar distributions of sliding coefficients, the estimated values locally differ by several orders of magnitude.

Relative to the RAC experiment, a larger mean ice thickness error produced by the ERA simulation is somewhat independent of the calibration of sliding coefficients, because it is induced by the precipitation deficit over continental East Antarctica, similarly to the GIS, IPS, and NRS experiments. Here the model calibration cannot compensate for such deficit, regardless of a minimal sliding allowed across these areas. Although generally smaller mean ice thickness errors in other experiments (e.g. MRI) seem to suggest a better model performance, in reality this is the result of the error cancellations mentioned above. Provided that the near-surface air temperature from a given AOGCM is high enough to allow for the basal thermal conditions which are favourable for sliding, moderate increments in precipitation rates can be compensated through excessive adjustments of sliding coefficients. Pronounced overestimations of ice thickness occur in the experiments that are driven by too low air temperatures, leaving large portions of the ice sheet frozen to bed (Fig. 4.4, e.g. CNR, FGS, and HAD). In this context, the evaluation of each particular forcing data set cannot be based on the resulting ice distribution alone, requiring an assessment of other modelled ice sheet quantities for which observational data are available. Such opportunity is provided by the observational data set of Rignot et al. (2011) that can be compared to our modelled surface ice velocity. Due to mutual reliance between the snow accumulation, ice thickness, and ice flow velocity, it is expected that differences in the modelled surface mass balance are reflected in the equilibrium velocity, when the ice thickness is kept constant. The results of the MRI experiment serve as an example of such bias transfer. Here, higher precipitation rates relative to the reference forcings (Fig. 4.1) are compensated by enhanced basal sliding (Fig. 4.4) that in turn generates higher ice velocities (Fig. 4.5) to keep the lowest mean ice thickness error among all experiments (Table 4.1). However, the MRI experiment exhibits a larger mean ice velocity error when compared to observations. The FGS experiment represents a similar case, although in many regions its relatively lower near-surface air temperature (Fig. 4.1) prevents the calibration of sliding coefficients, leading to widespread overestimations of the ice thickness and higher mean ice thickness errors. Even though the performance of the MRI and FGS experiments appears to be similar in terms of modelled ice sheet geometries and dynamics,

the former simulation could be erroneously considered a better fit when evaluated against the observed total ice volume and ice thickness distribution only.

Also, the fit between our estimated ice-shelf basal melting and freezing rates and recent observation-based equilibrium estimates of Rignot et al. (2013) (Fig. 4.3) can be used as an additional criterion for validation of the modelled ice-sheet states. The estimates from the reference experiments ERA and RAC reveal only minor differences expressed in the lower melting rates in the former, with a total BMB of $-1687.5\,\text{Gt}\,\text{yr}^{-1}$ for ERA and $-1907.9\,\text{Gt}\,\text{yr}^{-1}$ for RAC. The spatial patterns of melting and accretion zones from the RAC and ERA experiments compare well with observations, although our model-based BMB is in excess of $-1500 \pm 237\,\text{Gt}\,\text{yr}^{-1}$ estimated by Rignot et al. (2013), partly due to the lower resolution of our simulations and the use of a different atmospheric forcing (Bernales et al., 2017b). Compared to the reference experiments, higher melting rates in the FGS experiment are caused by overall higher precipitation rates suggested by FGOALS-g2 that result in an increased accumulation over ice shelves and a larger ice flux from the grounded ice sheet sectors (Fig. 4.1). Larger accretion zones predicted by the CNR, MRC, and MRI experiments have dissimilar origins. The reference topography used by the CNRM-CM5 model is generally higher than that suggested by the BEDMAP2 data set. This fact necessitates large lapse-rate corrections at the stage of an air temperature remapping for its use in the ice sheet model, resulting in too warm near-surface conditions. In attempt to maintain the ice shelf thickness close to observations, the model calibration is forced to generate artificial accretion patterns. In the MRC experiment, the removal of large portions of the West Antarctic ice sheet (see Sect. 4.3) leads to an insufficient ice flux from the grounded ice sheet, the lack of which is compensated by the calibration of the melting and freezing rates. Finally, too high near-surface air temperatures over the ice shelves in MRI decrease their mass balance in response to excessive surface melting, that has to be compensated for through an enhanced basal freezing. These results suggest that both the accumulation over the grounded ice sheet and the style of ice routing towards the ice sheet margins have equally important impacts on the resulting distribution and magnitudes of sub-shelf melting and freezing.

The aim of this study is to showcase the sensitivity of the retrieved sub-shelf melting and freezing to the choice of climate forcing data sets, and to evaluate the applicability of AOGCMs outputs for AIS modelling studies. The current analysis demonstrates that differences between the estimates of the BMB of ice shelves derived using different forcing

data sets are unlikely to be reconciled through the use of a higher ice sheet model resolution or a non-steady-state set-up. Furthermore, our analysis emphasises high sensitivity of the modelled sub-shelf melting and freezing in terms of both magnitude and occurrence and suggests that the choice of atmospheric forcing in numerical ice sheet simulations deserves an extra care, in particular in studies of marine ice sheets. We show that basal melt estimates from observations or modelling studies will unlikely produce realistic ice configurations if prescribed as boundary conditions in an independent modelling experiment. The success of such exercise will depend on the degree of consistency between the estimates of the ice shelf BMB, the prescribed ice sheet surface mass balance, and the model physics (Bernales et al., 2017b, in press). For example, the use of sub-shelf melting and freezing estimates from the calibration of the FGS experiment would trigger a disintegration of big ice shelves in a simulation driven by the atmospheric forcing from the MIROC-ESM model. In this sense, the results of our simulations provide a reference for the computation of an ice-shelf basal regime that is consistent with the applied atmospheric forcing, while the degree of agreement between the model-based and observed ice shelf BMB helps to identify potential biases in the climate forcing that can significantly impact the results of ice-sheet simulations.

4.5 Conclusions

The experiments carried out in this study have been designed to analyse the sensitivity of the modelled present-day Antarctic ice sheet to the choice of atmospheric forcing. The near-surface air temperatures and precipitation rates from the ERA-Interim reanalysis and the regional climate model RACMO2.3 have been used as a reference forcing against which the products of 10 different AOGCMs are evaluated.

Our results reveal that the use of most climate data sets may result in ice-sheet configurations that are close to observations, despite significant dissimilarities between the AOGCMs, if an extensive calibration of largely unconstrained internal model parameters is used. In this study, we have demonstrated that this can be accomplished through the calibration of basal sliding coefficients that have been originally introduced in the model to mimic unknown mechanical conditions at the base of the ice sheet. The adjustment of this parameter tends to compensate for the excessive precipitation through an increase in the ice flow velocity where basal sliding is identified, but cannot compensate for the

precipitation deficit. Based on the ice sheet model set-up implemented in this study, we conclude that an analysis relying exclusively on the fit between the observed and modelled total ice volumes and ice thickness would likely result in the preference of climate data sets that suggest wetter conditions and larger areas of basal melting. However, we show that potential error cancellations can be detected by evaluating the modelled ice surface velocities against observational data.

Furthermore, we have estimated the ice-shelf basal melting and freezing rates for each AOGCM that are consistent with their atmospheric fields. These estimates can be used as an independent criterion for the identification of biases in climate models through the comparison of the resulting distributions of melting and freezing areas with recent continental-scale observation-based estimates.

Chapter 5

Summary and outlook

This thesis centers around the interactions of the Antarctic ice sheet with the underlying bedrock, the surrounding ocean, and the atmosphere, zooming in on poorly constrained subglacial processes that strongly influence the dynamics of the ice sheet-shelf system. Such processes include ice sliding at the bedrock-ice interface and ocean-induced melting and freezing at the base of ice shelves. This work presents reconstructions of the present-day subglacial regimes of the grounded and floating ice sheet sectors, investigates their sensitivity to the model formulation and uncertainties in the external forcing, and evaluates the quality of climate fields derived from a large array of general circulation models using a continental-scale ice sheet model of the Antarctic ice sheet. The results are summarised in the form of three manuscripts that aim to answer main research questions of the present Ph.D. study (see Section 1.4).

The underlying methodology builds upon advancing the well-established model SICOPO-LIS (SImulation COde for POLythermal Ice Sheets; Sato and Greve, 2012), an open source, three-dimensional, thermomechanical ice sheet-shelf model that uses finite differences to solve for the ice flow using shallow approximations of the Stokes equations (Section 1.2), applied separately for the grounded and floating ice. The original version of the model included a simplified treatment of basal sliding under the grounded ice sheet and basal melting under the ice shelves (Sato and Greve, 2012). To evaluate the skill of the initial implementation of this model for the Antarctic region, the first collaborative study within this Ph.D. used it to investigate the uncertainties in the reconstruction of the mid-Pliocene and present-day configurations of the Antarctic ice sheet arising from different model formulations (de Boer et al., 2015) as a contribution to the international project PlioMIP (Pliocene Modelling Intercomparison Project; Haywood et al., 2010). Analysis

of experiments with this initial version of SICOPOLIS and other models indicated that simplifications in the model representation of the ice flow, basal sliding, and sub-shelf melt strongly contaminate the modelled dynamics and geometries of the ice sheet and ice shelves. Thus, the investigation of the questions central to this study required a further development of the modelling tools ranging from an implementation of new schemes to enable a better agreement between the observed and modelled ice sheet flow patterns to novel techniques designed to quantify subglacial processes under the grounded and floating ice sectors. The present chapter summarises key results of this Ph.D. study in an attempt to answer each of the research questions posed at the beginning of this thesis. It also presents an outlook of future improvements required to make these conclusions more robust and less model-dependent and of the studies which will become possible through such improvements.

Can uncertainties in subglacial sliding conditions and ocean-induced sub-shelf melting explain large deviations between the model-based and observed geometries and flow regimes of the present-day Antarctic ice sheet?

Rapidly flowing ice streams play a crucial role in the mass balance of the Antarctic ice sheet, channeling the ice discharge from the interior of the ice sheet to its margins. In most cases, ice streams are thought to be largely supported by subglacial sliding under the grounded ice sheet, which depends on highly heterogeneous conditions at the ice-bedrock interface. These subglacial conditions are currently poorly constrained due to a lack of observational techniques with the ability to penetrate the kilometers-thick ice sheet at a sufficiently large scale. Chapter 2 presents an implementation of new and existing model formulations that aim to replicate the flow patterns of ice streams. These different model formulations are combined with an iterative technique to infer the spatial distribution of the present-day basal sliding conditions under the grounded Antarctic ice sheet sectors. Analysis of the model performance and its sensitivity to variations in parameters that underpin each model formulation has enabled the development of a new approach for the modelling of the ice stream flow presented in Chapter 3. This approach is combined with a novel calibration technique to derive a quantification of basal melting and freezing rates under the entire Antarctic ice-shelf system.

Along the Antarctic coasts, most of the ice mass transported by ice streams is received and buttressed by ice shelves before reaching the Southern Ocean. Ice shelves tend to decelerate the mass loss from outlet glaciers and thus exert an important control on the

dynamics of the grounded ice sectors. However, ice shelves and their effects on the ice streams are sensitive to the thermal state of the underlying sea water. Ocean-induced basal melting is currently the largest contributor to the total mass loss of the ice sheet. Yet, future projections of the ice sheet changes have mostly relied on simplified parameterisations of this process that are not necessarily consistent with observations (Bernales et al., 2017b, in press). In contrast to previous studies, here an approach based on ice sheet modelling experiments is used to reconstruct complex patterns of the basal mass balance of ice shelves and explore the sensitivity of the sub-shelf regimes to the uncertainties in the external forcing (strong response) and model parameters (mostly a weak to negligible response).

This thesis reveals that the complementary use of the reconstructed subglacial sliding conditions and sub-shelf melting rates can significantly reduce the discrepancies between the modelled and observed ice geometries and flow patterns over large tracts of the grounded and floating Antarctic ice. With this method, widespread ice thickness errors that traditionally reach hundreds of meters (Pollard and DeConto, 2012b) can effectively reduced to an absolute mean value of ~ 30 m. However, this simultaneous calibration of basal regimes cannot completely eliminate the common errors in large-scale numerical simulations of the Antarctic ice sheet. An iterative adjustment of basal sliding parameters fails to resolve the topographic errors over mountainous regions and other ice sheet sectors where basal sliding is not predicted by the model. Together with unresolved flow patterns in highly dynamic regions (e.g., West Antarctica), such remanent discrepancies are shown to lead to erroneous displacements of the grounding line positions and thus enhanced deviations from the observed ice sheet geometry, if a free evolution of the grounding line and calving fronts is allowed (Bernales et al., 2017b, in press). These errors in the simulated ice sheet dynamical state may be related to the assumption of a steady state, uncertainties in the external climate forcing and other boundary conditions, and simplified treatment of the material properties of ice, such as anisotropy.

Are model-based reconstructions of the subglacial regimes below grounded and floating ice sheet sectors in agreement with available observations?

Although observations of subglacial sliding regimes and mechanical properties of the subglacial bed are rather limited, they indicate a locally high variability in the bedrock material properties, including the influence of subglacial hydrology (e.g., Ashmore and Bingham, 2014), *sticky spots* (e.g., Sergienko and Hulbe, 2011), the presence of obstacles (e.g., Salamon, 2015), and other external agents. In this thesis, the joint effect of these

variable factors on the basal sliding regimes is approximated by sliding coefficients that show a high heterogeneity across Antarctica, in agreement with direct evidence. Similarly high spatial variabilities have been inferred by independent modelling studies that employ sophisticated inversion methods constrained by the observed surface flow velocities in Antarctica and Greenland (e.g., Arthern et al., 2015; Brinkerhoff and Johnson, 2013). These previous modelling studies differ in their levels of model complexity, which is shown here to strongly impact the inferred basal sliding regimes. However, all of these studies predict variations of several orders of magnitude in the basal sliding coefficients. Despite the lack of sufficiently detailed observations of subglacial sliding regimes, a high degree of agreement between the observed and modelled surface ice velocities can serve as an independent validation of the model-based reconstruction of basal sliding parameters. In contrast to many published reconstructions of basal sliding conditions (e.g., Joughin et al., 2009; Morlighem et al., 2010; Arthern and Gudmundsson, 2010; Pralong and Gudmundsson, 2011; Arthern et al., 2015), this thesis adopts a methodology that is independent of the surface ice velocity observations, focusing on reproducing the observed ice sheet geometry instead (Pollard and DeConto, 2012b). As a result, the degree of agreement between the modelled and observed ice velocities is impacted by other model choices, such as model formulation and external forcing.

As opposed to the subglacial sliding conditions, model-based reconstructions of the sub-shelf melting and freezing rates presented in this thesis can be directly evaluated against two existing Antarctic-wide, observation-based data sets of Rignot et al. (2013) and Depoorter et al. (2013). Such comparison reveals that the method described in this study is able to reproduce the complex and highly heterogeneous melting and freezing patterns observed at the base of ice shelves. The model-based reconstruction contains large-scale features which are rarely taken into account in modelling experiments of the Antarctic ice sheet, including very high ice-shelf basal melting rates near grounding lines and ice shelf fronts, extensive accretion zones under many ice shelves, and high melting rates along the East Antarctic coast. At a local scale, the model-based sub-shelf melting regimes deviate from the observational data sets. However, the studies by Rignot et al. (2013), Depoorter et al. (2013), and previous estimates (e.g., Timmermann et al., 2012) present non-negligible differences between their retrieved ice-shelf basal mass balances, indicating that there are significant uncertainties in the sub-shelf melting regimes. This work offers a quantification of melting and freezing rates under the Antarctic ice shelves that is well within the current uncertainty range. Among the causes of local discrepancies

between our estimates and observations, errors in the modelled ice flow due to inaccurate ice sheet thickness predictions and low model resolution may be responsible for a higher-than-observed negative basal mass balance of ice shelves. Overall, the reconstruction of sub-shelf regimes presented here demonstrates that the basal mass balance of ice shelves required by ice sheet models is similar to that inferred from observational studies, and far from the values suggested by commonly utilised parameterisations.

Can ice-sheet modelling experiments reveal biases and errors in the external model forcing and other boundary conditions?

Studies of the rapid ice flow dynamics, subglacial sliding, and ice-shelf basal mass balance presented in Chapters 2 and 3 represent the bulk of the ice model-sourced uncertainties and are brought together in this thesis to assess the impacts of inaccuracies in the climate forcing, geothermal heat flux, and bedrock topography on the modelled dynamical state of the present-day Antarctic ice sheet. The model-based reconstructions of the sub-shelf melting regimes and total ice-shelf basal mass balance presented in this work reveal their high sensitivity to such inaccuracies. Thus, a joint analysis of the model results and available observations help quantifying the accuracy of external data sets. The study presented in Chapter 4 exemplifies this model skill by providing a detailed analysis of the biases in the present-day climate conditions inferred from general circulation models. A comparison of the performance of these data sets reveals that significant biases in the climate forcing generate widespread fingerprints in the retrieved subglacial sliding coefficients and sub-shelf melting and freezing patterns. These biases cannot be identified in the modelled ice sheet states when the results of simulations are evaluated solely against the observed total ice volume and ice thickness. However, we show that potential error cancellations can be detected by evaluating the modelled ice velocities and reconstructed sub-shelf regimes against observational data.

In contrast, the model response to the uncertainties in the geothermal heat flux forcing and bedrock elevation is comparable to the errors in the modelled ice thickness and surface velocities from simulations using reference data sets. This suggests that a joint evaluation of the model-based and observed fields described in this study may not give a definitive answer to which data set is more realistic. Yet, this does not obviate the possibility that imposing larger changes in the geothermal heat flux forcing (Schroeder et al., 2014) and involving other observational data sets (Rogozhina et al., 2016), such as ice layering and subglacial melting from ice penetrating radar and ice core measurements,

may lead to a successful separation of realistic from biased data sets. This, however, is left to future studies. Finally, it is important to keep in mind that the results summarised above depend on the methodological limitations in the experimental setup. From the assessment of how different approaches represent ice flow in streaming zones (Chapter 2), it is evident that the retrieved distributions of subglacial sliding conditions depend on the degree of the ice flow model complexity. As described in Section 1.2, SICOPOLIS utilises shallow approximations of the Stokes equations in order to enable an efficient use of computational resources. As shown by Pattyn et al. (2013), this type of models cannot be used in experiments that require higher-order dynamics, for example, those that involve a migration of the grounding line over short time scales. The use of more complex models for the applications described in this thesis is still a challenging task, mainly due to their significantly higher computational expenses. Once this becomes feasible, the methodology developed in this work can be transferred to higher-order models.

Another challenging task is the development of more specific model representations of subglacial sliding and sub-shelf basal melting. Due to lack of observational data, these processes are often over-simplified in an attempt to exclude a large number of unknown parameters. The problem is even more complicated when these parameterisations are employed by studies focusing on time periods outside of the satellite-era window for which observational data are scarce or absent. Following the growing data set of observations and reconstructions of the present and past states of the Antarctic ice sheet, the existing representations of these processes will be continuously tested and improved. A natural extension of the work presented in this thesis is the application of the developed techniques to infer subglacial sliding conditions in transient simulations over glacial cycles, which would require an inclusion of additional processes such as glacial isostatic rebound. For example, the methodologies described in Chapters 2 and 3 could be potentially adapted for modelling of Antarctic ice sheet-shelf configurations during the last deglaciation period in order to investigate the role of subglacial sliding and ocean thermal regimes on the retreat of the ice sheet towards its modern configuration. In the future, a likely arrival of improved polar data sets and new observational techniques will allow for a steady reduction of the uncertainties in these and other processes occurring at the interfaces between the ice and other Earth sub-systems. This will hopefully lead to a widespread inclusion of a dynamic cryosphere in Earth-System models, increasing the confidence in our ability to understand and predict the captivating dynamics of this planet.

Appendix A

Supplementary Materials

A.1   Supplementary Materials for Chapter 2

A.1.1   Ice sheet model resolution

This document describes a model resolution sensitivity study carried out prior to the experiments presented in the main text.

As part of this study we have tested model horizontal grid resolutions of 40, 20, and 10 km, which encompass a range of model resolutions often used for continental-scale numerical simulations of the Antarctic Ice Sheet (e.g., Pollard and DeConto, 2012b; de Boer et al., 2015; Pollard et al., 2015). This sensitivity analysis is motivated by a large number of simulations required for the comparison study of the four hybrid schemes, and the fact that forward ice sheet modelling at a resolution of 10 km is computationally expensive. As a result, we have decided to test a 10-km resolution only for one hybrid scheme (namely HS-3), merely as a proof-of-concept, and to confirm the low sensitivity of the model results to changes in the grid size discussed by Pollard and DeConto (2012b) and Pollard et al. (2015).

The experimental set-up closely follows that of the main experiments (Section 2.4), except for a shorter time span for each relaxation/free-evolution stage (50,000 model-years per stage here vs. 100,000 model-years per stage in the main experiments) to allow for the use of a model resolution of 10 km, over a total time span of 200,000 model-years for each model resolution tested.

As shown in Figure A.1 (top row), the ice sheet thickness distribution resulting from the use of different model resolutions is very similar at the end of the simulations, with

only minor differences which are mostly confined to the areas near the ice sheet margins.
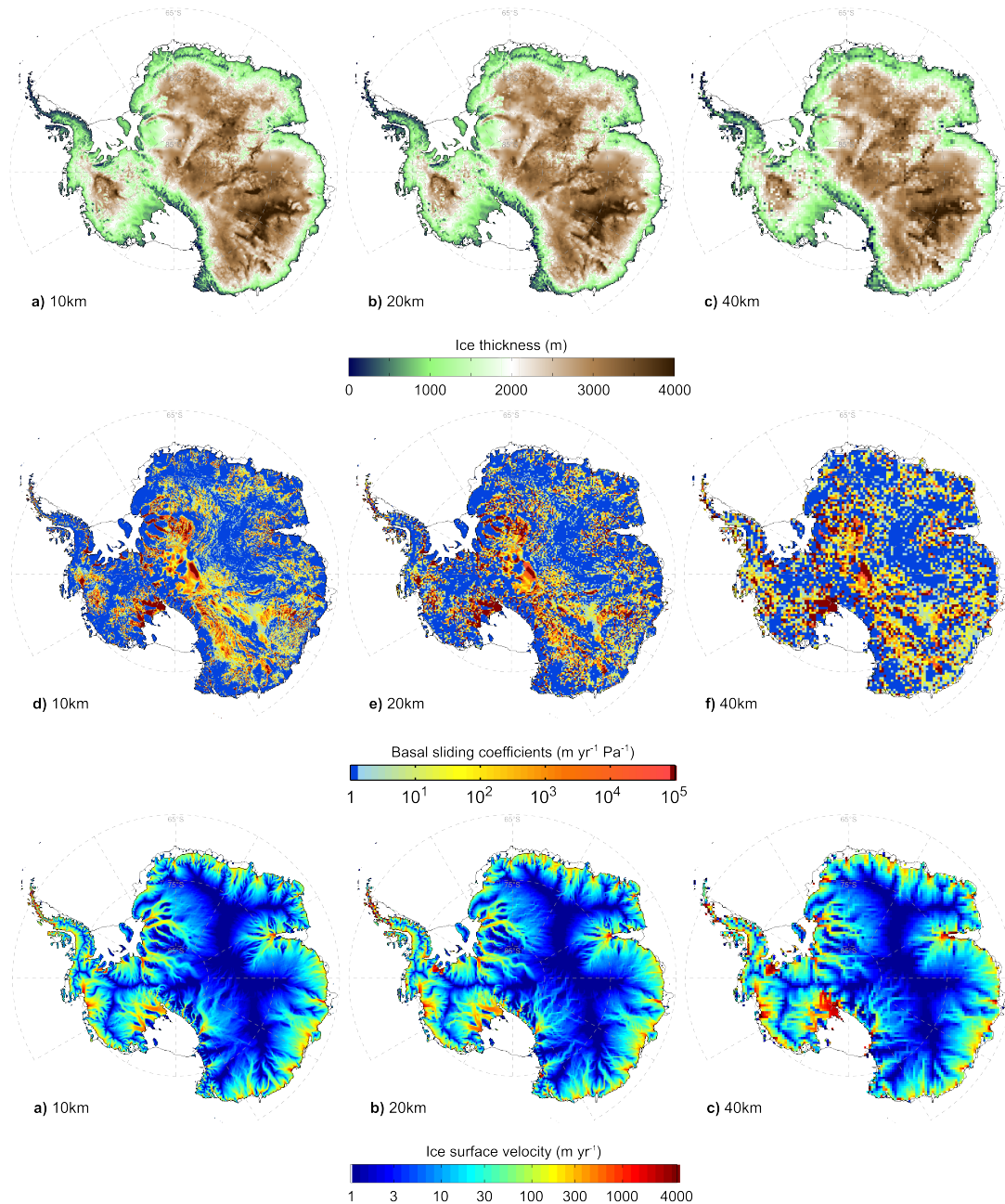
Figure A.1: Modeled ice sheet thickness (in m, top row), calibrated basal sliding coefficients (in m/yr/Pa, middle row), and modeled surface ice velocities (in m/yr, bottom row) at the end of 200,000-years-long steady-state simulations using model resolutions of 10 km (left column), 20 km (middle column), and 40 km (right column). See Chapter 2 for further details.

The calibrated basal sliding coefficients (Figure A.1, middle row) exhibit a relatively higher sensitivity to a change in model resolution, with discrepancies mainly caused by larger gradients in the lower model resolution runs. This is particularly visible in the simulation that uses a model resolution of 40 km, where a single calibrated value of the

basal sliding coefficient is used for a larger ice sheet area. This effect is less pronounced in the 20-km resolution simulation. However, overall the estimated basal sliding coefficients are robust over the ice sheet-covered area.

Modeled ice surface velocities (Figure A.1, bottom row) showcase a good ability of the model to reproduce observations (Section 2.5.2), even at the lowest model resolution of 40 km tested here. However, it is readily visible that changes in the grid size do affect the resulting ice velocities close to the ice sheet margins, where small outlet glaciers are often poorly resolved in simulations using a 40-km resolution. On the contrary, the modeled ice velocities in the 20-km resolution run closely follow the flow patterns produced by the 10-km simulation with only small-scale, isolated discrepancies.

Based on a high degree of similarity between our results of the simulations using model resolutions of 10 and 20 km, we have decided to use the latter for the comparison of the four hybrid schemes presented in the main text.

A.2 Supplementary Materials for Chapter 3

A.2.1 Experiments with freely evolving grounding lines and calving fronts

This document presents three additional experiments run for 500 model-years, starting from the equilibrium dynamical state of the Antarctic ice sheet and ice shelves from the REF experiment presented in the main text (Figures 3.1 and 3.2 in the manuscript). In these experiments, the grounding line and ice-shelf calving fronts are no longer fixed, and different boundary conditions are applied at the base of ice shelves. The grounding line position is now computed using a floatation condition (Sato and Greve, 2012), while calving at the ice-shelf front is parameterised using a simple threshold: if ice-shelf thickness at the front drops below 50 metres, ice within this grid cell is automatically removed (Sato and Greve, 2012). In the first simulation (henceforth PRG), the retrieved basal mass balance (BMB; Figure 3.1 in main text) is directly applied at the base of ice shelves in order to test whether the equilibrium state is maintained when the grounding line is released. The second simulation (henceforth MLT) uses the same set-up as PRG, but the inferred basal freezing across the ice-shelf accretion areas are neglected (set to a value of $0 \, \mathrm{m \, a^{-1}}$), to demonstrate the effects of disregarding the basal accretion processes. The third simulation (henceforth BnG) replaces the retrieved BMB for an existing parameterisation of the
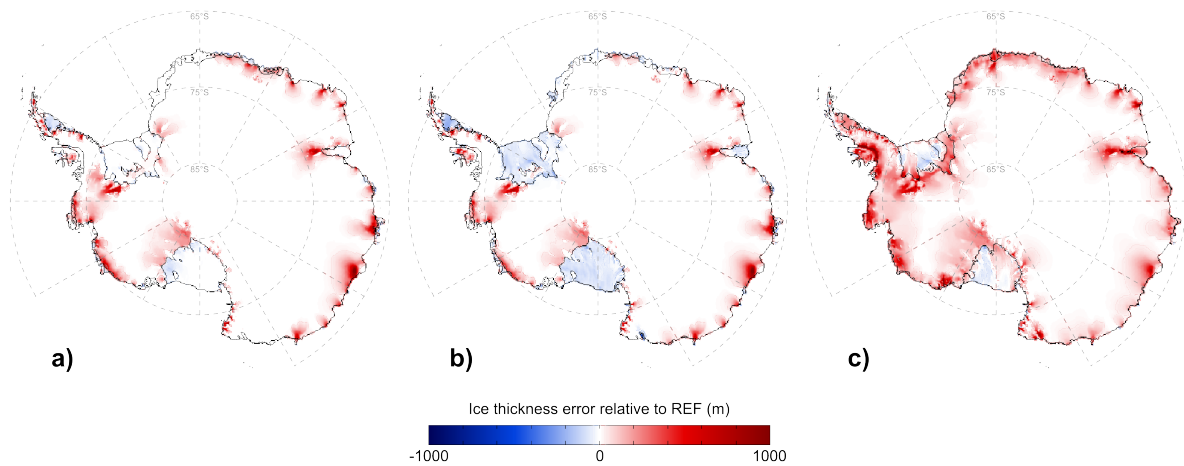
Figure A.2: Ice thickness errors relative to the REF simulation, in metres, at the end of 500-year-long prognostic simulations starting from the equilibrium ice-sheet configuration shown in Figures 3.1 and 3.2 (in the main text), with freely-evolving grounding lines and calving fronts, and a) prescribed calibrated ice-shelf basal melting and freezing rates from this study; b) as in (a), but with sub-shelf freezing neglected; and c) prescribed parameterisation based on Beckmann and Goosse (2003), following the parameter choices of Martin et al. (2011).

ice-ocean interaction in order to gauge the effects of the common simplifications of the melting and freezing patterns on the modelled ice sheet and ice shelves.

A.2.2　Direct use of the inferred basal melting and freezing rates as a boundary condition at the ice shelf base

The PRG experiment results in an ice sheet configuration that is close to the REF experiment presented in the main text. Figure A.2a shows the differences between the PRG and REF experiments. It can be observed that the errors in the ice sheet thickness remain nearly unchanged over most of the continental interior. However, these errors are amplified across regions where the REF simulation produces an overestimation of the ice thickness, especially in the vicinity of mountain ranges near the ice sheet margins. These areas are characterised by cold basal conditions, where basal thermal conditions do not favour sliding, and thus the calibration of the sliding coefficients has not been performed. Due to an accumulation of errors across such regions, the attained steady state is not absolute, thereby triggering the grounding line migration at the flux gates of some outlet glaciers, once the grounding line is released (e.g. Pine Island, Ross West, Totten, Amery, and Baudouin ice shelves). However, the predicted shifts in the grounding-line position in the PRG simulation are relatively minor, resulting in a realistic distribution of floating vs.

grounded ice areas.

It is important to keep in mind that the prescribed sub-shelf melting and freezing rates in the PRG experiment are not further calibrated to compensate for the changes in the ice sheet-shelf geometry. Thus, as soon as the ice sheet advances, the high-melt areas predicted by REF near the grounding line are replaced by areas of lower melt rates characteristic of the ice shelf interior. This results in an amplification of the grounding-line advance. Our retrieved ice-shelf BMB estimates are purely diagnostic and are not meant to be used directly as a boundary condition in transient, prognostic simulations. Instead, the BMB patterns and relative magnitudes for different ice shelves could be used to aid the development of new techniques (such as parameterisations) that would allow a prognostic BMB calculation. Knowing beforehand what BMB is necessary to maintain the ice sheet in a certain dynamical state (even if the grounding line is fixed) can provide a first-order approximation that can be later fine-tuned based on the specifics of a modelling study.

A.2.3   Effects of disregarding basal freezing

The results from MLT experiment are very similar to those from the PRG simulation. The main difference is that the largest ice shelves now exhibit a significant ice thickness deficit (Figure A.2b) in response to a step change in the boundary conditions. Such ice thickness underestimations are not restricted to the original accretion zones predicted by the REF simulation, but instead spread over the entire ice-shelf area. If the calibration procedure were originally designed with an assumption of non basal freezing, it would compensate for this ice thickness deficit through adjustments (reduction) of melting rates elsewhere. However, the ice-shelf thickness deficit would likely remain in the accretion zones, which may deliver an unrealistic mass flux input to an ice-shelf calving model component in large-scale, long-term ice-sheet simulations, thereby potentially accelerating the collapses of portions of ice shelves.

A.2.4   Comparison between the retrieved BMB and a standard parameterisation of ice-ocean interaction

In the BnG experiment, we have replaced the inferred basal melting and freezing rates by the parameterisation of Beckmann and Goosse (2003). The BnG experiment employs the same parameter choices as in the dynamic equilibrium simulation of Martin et al. (2011), with an ocean salinity set to 35 psu, an ocean temperature of $-1.7\,°C$, and a model

Ice shelf basal melt and freeze rates (m a^{-1})
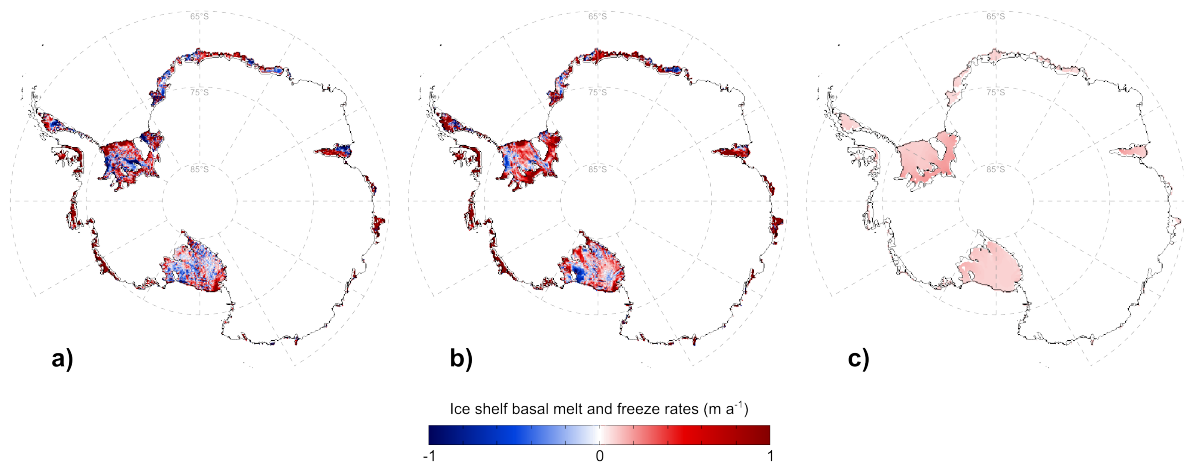
Figure A.3: Ice shelf basal melting and freezing rates (in metres per year). a) Observation-based estimates of Rignot et al. (2013). b) This study (as in Figure 3.1, in main text). c) Computed using the calibrated ice sheet from this study and a parameterisation based on Beckmann and Goosse (2003), following the parameter choices of Martin et al. (2011).

parameter $F_{\mathrm{melt}} = 5 \times 10^{-3}\,\mathrm{m\,s^{-1}}$ (see their Eq. 5). However, an important difference is that, in our study, the distribution of basal sliding coefficients in the grounded ice sheet sectors is calibrated to minimise the misfit between the modelled and observed ice sheet thickness, thus producing different modelled ice velocities and ice fluxes across the grounding line.

The resulting sub-shelf basal melting rates from the parameterisation of Beckmann and Goosse (2003) at the beginning of the transient experiment are shown in Figure A.3c, together with the observation-based distribution of Rignot et al. (2013) and the inferred distribution from our study included for comparison (Figures A.3a and b, respectively). The two main characteristics of the parameterised distribution of the ice shelf BMB is the lack of basal freezing and the large discrepancies with the observation-based estimates of Rignot et al. (2013). In this parameterisation, the melt rates are proportional to the current depth of an ice shelf, which defines its local pressure melting point. Since the deepest parts of the Antarctic ice shelves are usually located near grounding lines, this formulation generates slightly higher melt rates in these zones, in qualitative agreement with observations (e.g. Rignot et al., 2002). However, the parameterised melt rates near grounding lines are significantly lower than the observed values. Other parameter choices can in principle be used to increase the melt rates near the grounding line, but this would also generate higher melt rates across the entire ice shelf, leading to a strong ice shelf thinning and thus an ice shelf calving.

At the end of the 500-year-long simulation, the BnG experiment results in a strong degradation of the ice sheet geometry, including the grounded ice-sheet margins, and a significant grounding-line migration in many ice sheet sectors (Figure A.2c). As mentioned above, this can be attributed to the low melting rates (relative to the PRG experiment) near grounding lines, which are not sufficient to compensate for the high ice flux generated by the iterative calibration of basal sliding coefficients. Different parameter choices were tested in an attempt to reproduce the results of the PRG experiment (not shown), albeit with no success. The degradation observed in the BnG experiment indicates that this parameterisation is rather far from what our modelled ice sheet would need to keep the sheet-shelf system in an equilibrium state. Given the uncertainty in the ice sheet subglacial conditions, it may be possible to calibrate the basal sliding coefficients to obtain a realistic geometry of the modelled steady-state ice sheet using the parameterised BMB (as an independent boundary condition), but we expect that the results of such calibration will contain a significant error-compensation for the limitations described above, in addition to widespread discrepancies between the modelled and observed ice shelf geometries. In contrast, our modelled ice sheet has been actively tuned to produce the best possible ice sheet geometry that our model can generate, keeping the ice shelf geometries close to observations throughout the simulation. Thus, the ice sheet calibration is largely independent of the inferred ice shelf BMB, to which we attribute the good fit between our BMB estimates and observations.

List of Figures

Nomenclature

Abbreviations

AIS	Antarctic Ice Sheet
AOGCM	Atmosphere-Ocean Global Circulation Model
BEDMAP	Bed Topography of the Antarctic region (data set)
BMB	Basal Mass Balance
BMR	Basal Melt Rate
CMIP	Coupled Model Intercomparison Project
ERA-Interim	European global atmospheric re-analysis
FS	Full Stokes (model)
HS	Hybrid Scheme
ISMIP	Ice Sheet Model Intercomparison Project
IPCC	Intergovernmental Panel on Climate Change
PDD	Positive Degree-Day (method)
PMIP	Paleoclimate Modelling Intercomparison Project
RACMO	Regional Atmospheric Climate MOdel
RCM	Regional Climate Model
SIA	Shallow Ice Approximation
SICOPOLIS	SImulation COde for POLythermal Ice Sheets
SMB	Surface Mass Balance
SoS	SIA-only Scheme
SSA	Shallow Shelf Approximation
SStA	Shelfy Stream Approximation

List of symbols

Symbol	Definition	Unit
$\nabla, \nabla\cdot, \nabla\times$	Gradient, divergence, and curl operators	
A	Ice rate factor	$\mathrm{s}^{-1}\,\mathrm{Pa}^{-3}$
a_s	surface mass balance	$\mathrm{m}\,\mathrm{s}^{-1}$
a_b	basal mass balance	$\mathrm{m}\,\mathrm{s}^{-1}$

Symbol	Definition	Unit
α_{std}	PDD temperature standard deviation	$^{\circ}\mathrm{C}$
α_{ice}, β_{ice}	PDD factor for ice	$\mathrm{mm\,i.e.\,d^{-1}\,^{\circ}C^{-1}}$
α_{snow}, β_{snow}	PDD factor for snow	$\mathrm{mm\,i.e.\,d^{-1}\,^{\circ}C^{-1}}$
β	Clausius-Clapeyron gradient	$\mathrm{K\,m^{-1}}$
C_0	Calibrated basal sliding parameter	$\mathrm{m\,yr^{-1}\,Pa^{-1}}$
c	Specific heat of ice	$\mathrm{J\,kg^{-1}\,K^{-1}}$
γ	Sub-melt-sliding parameter	K
ΔH	Difference between modelled and observed ice thickness	m
Δt_{inv}	Time step for inversion of C_0	yr
E	Flow enhancement factor	
E_{SIA}, E_{SSA}	Flow enhancement factor for the SIA and SSA	
η	Ice shear viscosity	$\mathrm{s^{-1}\,Pa^{-2}}$
F_{tan}	Scaling parameter for the adjustment of sub-shelf basal melting	
$\mathbf{g}$	Gravitational acceleration	$\mathrm{m\,s^{-2}}$
H	Modelled ice thickness	m
H_{obs}, H_0	Observed ice thickness	m
H_{sw}	Difference between mean sea level and ice base topography	m
H_{inv}	Ice thickness factor for inversion of sliding coefficients	m
H_{scl}	Ice thickness factor for inversion of sub-shelf melting	m
h_{rlx}	Scaling factor for relaxation procedure	
I	Unit tensor	
κ	Heat conductivity of ice	$\mathrm{W\,m^{-1}\,K^{-1}}$
κ_{r}	Heat conductivity of the lithosphere	$\mathrm{W\,m^{-1}\,K^{-1}}$
L	Latent heat of ice	$\mathrm{kJ\,kg^{-1}}$
N_{b}	Effective basal pressure	Pa
n	Power-law exponent	
P	Pressure	Pa
p, q	Sliding law exponents	
R	Universal gas constant	$\mathrm{J\,mol^{-1}\,K^{-1}}$
r	Slip ratio of grounded ice	
r_{thr}	Default threshold value of r	
ρ_{ice}	Ice density	$\mathrm{kg\,m^3}$
ρ_{sw}	Sea-water density	$\mathrm{kg\,m^3}$
σ_e	Effective stress	Pa
σ_0	Residual stress	Pa
T	Absolute temperature of ice	K
T_{m}	Ice temperature relative to the pressure melting point	K
T_{r}	Absolute temperature of the lithosphere	K
$\mathrm{tr}()$	Trace operator	
$\vec{\tau}_{\mathrm{b}}$	Basal shear stress	Pa
$\vec{U}$, $\mathbf{U}$	Horizontal hybrid velocity	$\mathrm{m\,s^{-1}}$
$\vec{u}$, $\mathbf{u}_{\mathrm{sia}}$	Horizontal SIA velocity	$\mathrm{m\,s^{-1}}$
$\vec{u_{\mathrm{s}}}$	Surface horizontal SIA velocity	$\mathrm{m\,s^{-1}}$
$\vec{u_{\mathrm{b}}}$	Basal horizontal SIA velocity	$\mathrm{m\,s^{-1}}$
u_{ref}, v_{ref}	Default ice-stream reference value of $|\vec{v}|$	$\mathrm{m\,s^{-1}}$
$\mathbf{v}$	Ice velocity	$\mathrm{m\,s^{-1}}$
$\vec{v}$, $\mathbf{u}_{\mathrm{ssta}}$	Horizontal SStA velocity	$\mathrm{m\,s^{-1}}$
$\vec{v_{\mathrm{s}}}$	Surface horizontal SStA velocity	$\mathrm{m\,s^{-1}}$
$\vec{v_{\mathrm{b}}}$	Basal horizontal SStA velocity	$\mathrm{m\,s^{-1}}$
w	Weighting function in hybrid schemes	
$\mathbf{\Omega}$	Angular velocity of the Earth	$\mathrm{s^{-1}}$

Bibliography

Ahlkrona, J., Loetstedt, P., Kirchner, N., and Zwinger, T. (2016) Dynamically coupling the non-linear Stokes equations with the Shallow Ice Approximation in glaciology: Description and first applications of the ISCAL method. J. Comput. Phys., 308, 1–19, doi:10.1016/j.jcp.2015.12.025

Agosta, C., Fettweis, X., and Datta, R. (2015) Evaluation of the CMIP5 models in the aim of regional modelling of the Antarctic surface mass balance. The Cryosphere, 9, 2311–2321, doi:10.5194/tc-9-2311-2015

Alley, R.B., Blankenship, D.D., Bentley, C.R., and Rooney, S. (1987) Till beneath ice stream B: 3. Till deformation: evidence and implications. J. Geophys. Res., 92, 8921–8929, doi:10.1029/JB092iB09p08921

Alley, R.B., Spencer, M.K., and Anandakrishnan, S. (2007) Ice-sheet mass balance: assessment, attribution and prognosis. Annals of Glaciology, 46, 1–7.

Arthern, R.J. and Gudmundsson, G.H. (2010) Initialization of ice-sheet forecasts viewed as an inverse Robin problem. J. Glaciol., 56, 527–533, doi:10.3189/002214310792447699

Arthern, R.J., Hindmarsh, R.C., and Williams, C.R. (2015) Flow speed within the Antarctic ice sheet and its controls inferred from satellite observations. J. Geophys. Res. Earth Surf., 120, 1171–1188, doi:10.1002/2014JF003239

Ashmore, D., and Bingham, R. (2014) Antarctic subglacial hydrology: Current knowledge and future challenges. Antarctic Science, 26(6), 758–773, doi:10.1017/S0954102014000546

Bamber, J.L., Riva, R.E.M., Vermeersen, B.L.A., and Le Brocq, A.M. (2009) Reassessment of the potential sea-level rise from a collapse of the West Antarctic Ice Sheet. Science, 324(5929), 901–903, doi:10.1126/science.1169335

Bamber, J.L., and Aspinall, W.P. (2014) An expert judgement assessment of future sea level rise from the ice sheets. Nature Climate Change, 3, 424–427, doi:10.1038/nclimate1778

Barkov, N.I. (1985) Ice shelves of Antarctica. Amerind Publishing Company, New Delhi, New York, USA.

Beckmann, A., and Goosse, H. (2003) A parameterisation of ice shelf–ocean interaction for climate models. Ocean modelling, 5(2), 157–170, doi:10.1016/S1463-5003(02)00019-7

Bentley, M.J., Cofaigh, C.Ó., Anderson, J.B., and 84 others (2014) A community-based geological reconstruction of Antarctic ice sheet deglaciation since the Last Glacial Maximum. Quaternary Science Reviews, 100, 1–9, doi:10.1016/j.quascirev.2014.06.025

Bernales, J., Rogozhina, I., Greve, R., and Thomas, M. (2017a) Comparison of hybrid schemes for the combination of Shallow Approximations in numerical simulations of the Antarctic Ice Sheet. The Cryosphere, 11, 247–265, doi:10.5194/tc-11-247-2017

Bernales, J., Rogozhina, I., and Thomas, M. (2017b) Melting and freezing under Antarctic ice shelves from ice-sheet modelling. J. Glaciol. (accepted).

Bernales, J., Rogozhina, I., and Thomas, M. (2017c) Evaluating climate models over Antarctica using an ice sheet model. Journal of Geophysical Research (submitted).

Bindschadler, R.A., Nowicki, S., Abe-Ouchi, A., Aschwanden, A., Choi, H., Fastook, J., Granzow, G., Greve, R., Gutowski, G., Herzfeld, U., Jackson, C., Johnson, J., Khroulev, C., Levermann, A., Lipscomb, W.H., Martin, M., Morlighem, M., Parizek, .B.R, Pollard, D., Price, S.F., Ren, D., Saito, F., Sato, T., Seddik, H., Serouss, H., Takahashi, K., Walker, R., and Wang, W.L.(2013) Ice-sheet model sensitivities to environmental forcing and their use in projecting future sea level (the SeaRISE project). Journal of Glaciology, 59(214), 195–224, doi:10.3189/2013JoG12J125

Blankenship, D.D., Bentley, C.R., Rooney, S.T., and Alley, R.B. (1986) Seismic measurements reveal a saturated porous layer beneath an active Antarctic ice stream. Nature, 322, 54–57, 10.1038/322054a0

Blatter, H. (1995) Velocity and stress fields in grounded glaciers: a simple algorithm for including deviatoric stress gradients. J. Glaciol., 41, 333–344, doi:10.1017/S002214300001621X

de Boer, B., Dolan, A.M., Bernales, J., Gasson, E., Goelzer, H., Golledge, N.R., Sutter, J., Huybrechts, P., Lohmann, G., Rogozhina, I., Abe-Ouchi, A., Saito, F., and van de Wal, R.S.W. (2015) Simulating the Antarctic ice sheet in the late-Pliocene warm period: PLISMIP-ANT, an ice-sheet model intercomparison project. The Cryosphere, 9, 881–903, doi:10.5194/tc-9-881-2015

Bracegirdle, T.J., and Marshall, G.J. (2012) The reliability of Antarctic tropospheric pressure and temperature in the latest global reanalyses. J. Clim., 25(20), 7138–7146, doi:10.1175/JCLI-D-11-00685.1

Bragg, F.J., Lunt, D.J., and Haywood, A.M. (2012) Mid-Pliocene climate modelled using the UK Hadley Centre Model: PlioMIP Experiments 1 and 2. Geoscientific Model Development, 5, 1109–1125, doi:10.5194/gmd-5-1109-2012

Brinkerhoff, D.J., and Johnson, J. (2013) Data assimilation and prognostic whole ice sheet modelling with the variationally derived, higher order, open source, and fully parallel ice sheet model VarGlaS. The Cryosphere, 7, 1161–1184, doi:10.5194/tc-7-1161-2013

Bromwich, D.H., Nicolas, J.P., and Monaghan, A.J. (2011) An assessment of precipitation changes over Antarctica and the Southern Ocean since 1989 in contemporary global reanalyses. J. Clim., 24(16), 4189–4209, doi:10.1175/2011JCLI4074.1

Bueler, E. and Brown, J. (2009) Shallow shelf approximation as a "sliding law" in a thermomechanically coupled ice sheet model. J. Geophys. Res., 114, F03008, doi:10.1029/2008JF001179

Calov, R. and Greve, R. (2005) A semi-analytical solution for the positive degree-day model with stochastic temperature variations. J. Glaciol., 51, 173–175, doi:10.3189/172756505781829601

Church, J.A., Clark, P.U., Cazenave, A., Gregory, J.M., Jevrejeva, S., Levermann, A., Merrifield, M.A., Milne, G.A., Nerem, R.S., Nunn, P.D., Payne, A.J., Pfeffer, W.T., Stammer, D., and Unnikrishnan, A.S. (2013) Sea-level Change. In: Climate change 2013: The physical science basis, contribution of Working Group I to the fifth assessment report of the Intergovernmental Panel on Climate Change, edited by: Stocker, T.F., Qin, D., Plattner, G.K., Tignor, M., Allen, S.K., Boschung, J., Nauels, A., Xia, Y., Bex, V., and Midgley, P.M., Cambridge University Press, Cambridge, UK and New York, NY, USA.

Clarke, G.K.C., Nitsan, U., and Paterson, W.S.B. (1977) Strain heating and creep instability in glaciers and ice sheets. Reviews of Geophysics, 15(2), 235–247, doi:10.1029/RG015i002p00235

Cuffey, K.M. and Paterson, W.S.B. (2010) The physics of glaciers. Elsevier, Burlington, MA, USA.

Davies, B.J., Carrivick, J.L., Glasser, N.F., Hambrey, M.J., and Smellie, J.L. (2012) Variable glacier response to atmospheric warming, northern Antarctic Peninsula, 1988–2009. The Cryosphere, 6, 1031–1048, doi:10.5194/tc-6-1031-2012

Davis, C.H., Li, Y., McConnell, J.R., Frey, M.M., and Hanna, E. (2005) Snowfall-driven growth in East Antarctic ice sheet mitigates recent sea-Level rise. Science, 308(5730), 1898–1901, doi:10.1126/science.1110662

DeConto, R.M., and Pollard, D. (2003) Rapid Cenozoic glaciation of Antarctica induced by declining atmospheric CO2. Nature, 421(6920), 245–249, doi:10.1038/nature01290

Dee, D.P., Uppala, S.M., Simmons, A.J., Berrisford, P., Poli, P., Kobayashi, S., Andrae, U., Balmaseda, M.A., Balsamo, G., Bauer, P., Bechtold, P., Beljaars, A.C.M., vande Berg, L., Bidlot, J., Bormann, N., Delsol, C., Dragani, R., Fuentes, M., Geer, A.J., Haimberger, L., Healy, S.B., Hersbach, H., Hólm, E.V., Isaksen, L., Kållberg, P., Köhler, M., Matricardi, M., McNally, A.P., Monge-Sanz, B.M., Morcrette, J.-J., Park, B. K., Peubey, C., deRosnay, P., Tavolato, C., Thépaut, J.-N., and Vitart, F. (2011) The ERA-Interim reanalysis: configuration and performance of the data assimilation system. Q. J. Roy. Meteor. Soc., 137, 553–597, doi:10.1002/qj.828

Depoorter, M.A., Bamber, J.L., Griggs, J.A., Lenaerts, J.T.M., Ligtenberg, S.R.M., van den Broeke, M.R., and Moholdt, G. (2013) Calving fluxes and basal melt rates of Antarctic ice shelves. Nature, 502(7469), 89–92, doi:10.1038/nature12567

Doake, C.S.M. (1984) Antarctic mass balance: glaciological evidence from Antarctic Peninsula and Weddell Sea sector. In Glaciers ice sheets, and sea level: Effect of a CO2-induced climatic change. Report of a workshop held in Seattle Washington September 13–15, 1984, 197–209.

Dunse, T., Greve, R., Schuler, T.V., and Hagen, J.O. (2011) Permanent fast flow versus cyclic surge behavior: numerical simulations of the Austfonna ice cap, Svalbard. J. Glaciol., 57, 247–259, doi:10.3189/002214311796405979

Dupont, T.K., and Alley, R.B. (2005) Assessment of the importance of ice-shelf buttressing to ice-sheet flow. Geophysical Research Letters, 32(4), L04503,, doi:10.1029/2004GL022024

Engelhardt, H., and Kamb, B. (2013) Kamb Ice Stream flow history and surge potential. Ann. Glaciol., 54, 287–298, doi:10.3189/2013AoG63A535

Eyring, V., Bony, S., Meehl, G.A., Senior, C.A., Stevens, B., Stouffer, R.J., and Taylor, K.E.(2016) Overview of the Coupled Model Intercomparison Project Phase 6 (CMIP6) experimental design and organization. Geoscientific Model Development 9, 1937–1958, doi:10.5194/gmd-9-1937-2016

Feldmann, J., Albrecht, T., Khroulev, C., Pattyn, F., and Levermann, A. (2014) Resolution-dependent performance of grounding line motion in a shallow model compared with a full-Stokes model according to the MISMIP3d intercomparison. J. Glaciol., 60, 353–360, doi:10.3189/2014JoG13J093

Foldvik, A., Gammelsrod, T., Nygaard, E., and Osterhus, S. (2001) Current measurements near Ronne Ice Shelf: Implications for circulation and melting. Journal of Geophysical Research: Oceans, 106(C3), 4463–4477, doi:10.1029/2000JC000217

Fowler, A.C. (2010) Weertman, Lliboutry and the development of sliding theory. Journal of Glaciology (56)200, 965–972.

Fox Maule, C., Purucker, M.E., Olsen, N., and Mosegaard, K. (2005) Heat flux anomalies in Antarctica revealed by satellite magnetic data. Science, 309(5733), 464-467, doi:10.1126/science.1106888

Fretwell, P., Pritchard, H.D., Vaughan, D.G., Bamber, J.L., Barrand, N.E., Bell, R., Bianchi, C., Bingham, R.G., Blankenship, D.D., Casassa, G., Catania, G., Callens, D., Conway, H., Cook, A.J., Corr, H.F.J., Damaske, D., Damm, V., Ferraccioli, F., Forsberg, R., Fujita, S., Gogineni, P., Griggs, J.A., Hindmarsh, R.C.A., Holmlund, P., Holt, J.W., Jacobel, R.W., Jenkins, A., Jokat, W., Jordan, T., King, E.C., Kohler, J., Krabill, W., Riger-Kusk, M., Langley, K.A., Leitchenkov, G., Leuschen, C., Luyendyk, B.P., Matsuoka, K., Nogi, Y., Nost, O.A., Popov, S.V., Rignot, E., Rippin, D.M., Riviera, A., Roberts, J., Ross, N., Siegert, M.J., Smith, A.M., Steinhage, D., Studinger, M., Sun, B., Tinto, B.K., Welch, B.C., Young, D.A., Xiangbin, C., and Zirizzotti, A. (2013) Bedmap2: improved ice bed, surface and thickness datasets for Antarctica. The Cryosphere, 7, 375–393, doi:10.5194/tc-7-375-2013

Fyke, J.G., Sacks, W.J., and Lipscomb, W.H. (2014) A technique for generating consistent ice sheet initial conditions for coupled ice sheet/climate models. Geosci. Model Dev., 7, 1183–1195, doi:10.5194/gmd-7-1183-2014

Fyke, J.G., D'Orgeville, M., and Weaver, A.J. (2015) Drake Passage and Central American Seaway controls on the distribution of the oceanic carbon reservoir. Global and Planetary Change, 128, 72–82, doi:10.1016/j.gloplacha.2015.02.011

Gagliardini, O., Zwinger, T., Gillet-Chaulet, F., Durand, G., Favier, L., de Fleurian, B., Greve, R., Malinen, M., Martín, C., Råback, P., Ruokolainen, J., Sacchettini, M., Schäfer, M., Seddik, H., and Thies, J. (2013) Capabilities and performance of Elmer/Ice, a new-generation ice sheet model. Geosci. Model Dev., 6, 1299–1318, doi:10.5194/gmd-6-1299-2013

Galeotti, S., DeConto, R.M., Naish, T., Stocchi, P., Florindo, F., Pagani, M., Barret, P., Bohaty, S.M., Lancy, L., Pollard, D., Sandroni, S., Talarico, F.M., and Zachos, J.C. (2016) Antarctic ice sheet variability across the Eocene-Oligocene boundary climate transition. Science, 352(6281), 76–80, doi: 10.1126/science.aab0669

Gammelsrod, T., Foldvik, A., Nost, O.A., Foldvik, O., Anderson, L.G., Fogelqvist, E., Olsson, K., Tanhua, T., Jones, E.P., and Osterhus, S. (1994) Distribution of water masses on the continental shelf in the southern Weddell Sea. In: The polar oceans and their role in shaping the global environment, 159–176, doi:10.1029/GM085p0159

Gerdes, R., Determann, J., and Grosfeld, K. (1999) Ocean circulation beneath Filchner-Ronne Ice Shelf from three-dimensional model results. Journal of Geophysical Research: Oceans, 104(C7), 15827–15842, doi:10.1029/1999JC900053

Gillett, N.P., Arora, V.K., Zickfeld, K., Marshall, S.J., and Merryfield, W.J. (2011) Ongoing climate change following a complete cessation of carbon dioxide emissions. Nature Geoscience, 4, 83–87, doi:10.1038/ngeo1047

Glen, J.W. (1955) The creep of polycristalline ice. Proc. R. Soc. Lond. A, 228 519–538, doi:10.1098/rspa.1955.0066

Greve, R. (1997) A continuum-mechanical formulation for shallow polythermal ice sheets. Philos. T. Roy. Soc. A, 355, 921–974, doi:10.1098/rsta.1997.0050

Greve, R., and Blatter, H. (2009) Dynamics of ice sheets and glaciers. Advances in Geophysical and Enviromental Mechanics, Springer-Verlag Berlin Heidelberg, DE, doi:10.1007/978-3-642-03415-2

Greve, R., and Blatter, H. (2016) Comparison of thermodynamics solvers in the polythermal ice sheet model SICOPOLIS. Polar Science, 10(1), 11–23, doi:10.1016/j.polar.2015.12.004

Gudmundsson, G.H. (2013) Ice-shelf buttressing and the stability of marine ice sheets. The Cryosphere, 7, 647–655, doi:10.5194/tc-7-647-2013

Hay, W.W., Soeding, E., DeConto, R.M., and Wold, C.N. (2002) The Late Cenozoic uplift–climate change paradox. International Journal of Earth Sciences, 91(5), 746–774, doi:10.1007/s00531-002-0263-1

Haywood, A.M., Dowsett, H.J., Otto-Bliesner, B., Chandler, M.A., Dolan, A.M., Hill, D.J., Lunt, D.J., Robinson, M.M., Rosenbloom, N., Salzmann, U., and Sohl, L.E. (2010) Pliocene Model Intercomparison Project (PlioMIP): experimental design and boundary conditions (Experiment 1). Geoscientific Model Development, 3, 227–242, doi:10.5194/gmd-3-227-2010

Hellmer, H.H. (2004) Impact of Antarctic ice shelf basal melting on sea ice and deep ocean properties. Geophysical Research Letters, 31(10), doi:10.1029/2004GL019506

Hellmer, H.H., Kauker, F., Timmermann, R., Determann, J., and Rae, J. (2012) Twenty-first-century warming of a large Antarctic ice-shelf cavity by a redirected coastal current. Nature, 485(7397), 225–228, doi:10.1038/nature11064

Hindmarsh, R.C.A. (2004) A numerical comparison of approximations to the Stokes equations used in ice sheet and glacier modeling. J. Geophys. Res., 109, F01012, doi:10.1029/2003JF000065

Holland, P.R., Jenkins, A., and Holland, D.M. (2008) The response of ice shelf basal melting to variations in ocean temperature. Journal of Climate, 21(11), 2558–2572, doi:10.1175/2007JCLI1909.1

Holland, P.R., Corr, H.F., Vaughan, D.G., Jenkins, A., and Skvarca, P. (2009) Marine ice in Larsen ice shelf. Geophysical Research Letters, 36(11), doi:10.1029/2009GL038162

Holland, P.R., Jenkins, A., and Holland, D.M. (2010) Ice and ocean processes in the Bellingshausen Sea, Antarctica. Journal of Geophysical Research: Oceans, 115(C5), doi:10.1029/2008JC005219

Hulbe, C., and Fahnestock, M.: Century-scale discharge stagnation and reactivation of the Ross ice streams, West Antarctica. J. Geophys. Res., 112, F03S27, doi:10.1029/2006JF000603

Hutter, K. (1983) Theoretical glaciology; material science of ice and the mechanics of glaciers and ice sheets. D.D. Reidel Publishing Co./Tokyo, Terra Scientific Publishing Co.

IPCC (2013) Climate Change 2013: The Physical Science Basis. Contribution of Working Group I to the Fifth Assessment Report of the Intergovernmental Panel on Climate Change. Edited by Stocker, T.F., Qin, D., Plattner, G.K., Tignor, M., Allen, S.K., Boschung, J., Nauels, A., Xia, Y., Bex, V., and P.M. Midgley. Cambridge University Press, Cambridge, United Kingdom and New York, NY, USA.

Jacobs, S.S., Hellmer, H., Doake, C.S.M., Jenkins, A., and Frolich, R. (1992) Melting of ice shelves and the mass balance of Antarctica. Journal of Glaciology, 38(130), 375–387, doi:10.3198/1992JoG38-130-375-387

Jacobs, S.S., Jenkins, A., Giulivi, C.F., and Dutrieux, P. (2011) Stronger ocean circulation and increased melting under Pine Island Glacier ice shelf. Nature Geoscience, 4, 519–523, doi:10.1038/ngeo1188

Jenkins, A., and Holland, D.M. (2002) A model study of ocean circulation beneath Filchner-Ronne Ice Shelf, Antarctica: Implications for bottom water formation. Geophysical research letters, 29(8), 34–1, doi:10.1029/2001GL014589

Jenkins, A., and Holland, D. (2007) Melting of floating ice and sea level rise. Geophysical Research Letters, 34(16), doi:10.1029/2007GL030784

Jenkins, A., and Jacobs, S. (2008) Circulation and melting beneath George VI ice shelf, Antarctica. Journal of Geophysical Research: Oceans, 113(C4), doi:10.1029/2007JC004449

Jokat, W., Boebel, T., König, M., and Meyer, U. (2003) Timing and geometry of early Gondwana breakup, J. Geophys. Res., 108, 2428, doi:10.1029/2002JB001802, B9

Joughin, I., and Padman, L. (2003) Melting and freezing beneath Filchner-Ronne Ice Shelf, Antarctica. Geophysical Research Letters, 30(9), doi:10.1029/2003GL016941

Joughin, I., Tulaczyk, S., Bamber, J.L., Blankenship, D., Holt, J.W., Scambos, T., and Vaughan, D.G. (2009) Basal conditions for Pine Island and Thwaites Glaciers, West Antarctica, determined using satellite and airborne data. J. Glaciol., 55, 245–257, doi:10.3189/002214309788608705

Joughin, I., and Alley, R.B. (2011) Stability of the West Antarctic ice sheet in a warming world. Nature Geoscience, 4(8), 506–513, doi:10.1038/ngeo1194

Joughin, I., Alley, R.B., and Holland, D.M. (2012) Ice-sheet response to oceanic forcing. Science, 338(6111), 1172–1176, doi:10.1126/science.1226481

Kamb, B. (2001) Basal zone of the West Antarctic ice streams and its role in lubrication of their rapid motion. In: The West Antarctic ice sheet: behavior and environment, edited by: Alley, R.B., and Bindschadle, R.A., American Geophysical Union, Washington, D.C., 157–199, doi:10.1029/AR077p0157

Lenaerts, J.T.M., van den Broeke, M.R., Déry, S.J., van Meijgaard, E., van deBerg, W.J., Palm, S.P., and Sanz Rodrigo, J. (2012) Modeling drifting snow in Antarctica with a regional climate model: 1. Methods and model evaluation. Journal of Geophysical Research, 117(D05108), doi:10.1029/2011JD016145

Levermann, A., Albrecht, T., Winkelmann, R., Martin, M.A., Haseloff, M., and Joughin, I (2012) Kinematic first-order calving law implies potential for abrupt ice-shelf retreat. The Cryosphere, 6, 273–286, doi:10.5194/tc-6-273-2012

Lliboutry, L., and Duval, P. (1985) Various isotropic and anisotropic ices found in glaciers and polar ice caps and their corresponding rheologies. Ann. Geophys., 3, P207–224, doi:

Ligtenberg, S.R.M., van de Berg, W.J., van den Broecke, M.R., Rae, J.G.L, and van Meijgaard, E. (2013) Future surface mass balance of the Antarctic ice sheet and its influence on sea level change, simulated by a regional atmospheric climate model. Climate Dynamics, 41(3), 867–884, doi:10.1007/s00382-013-1749-1

Lythe, M.B., Vaughan, D.G., and the BEDMAP Consortium (2001) BEDMAP: A new ice thickness and subglacial topographic model of Antarctica. Journal of Geophysical Research, 106, 11335–11351, doi:10.1029/2000JB900449

Ma, Y., Gagliardini, O., Ritz, C., Gillet-Chaulet, F., Durand, G., and Montagnat, M. (2010) Enhancement factors for grounded ice and ice shelves inferred from an anisotropic ice-flow model. J. Glaciol., 56, 805–812, doi:10.3189/002214310794457209

Mackintosh, A.N., Verleyen, E., O'Brien, P.E., White, D.A., Jones, R.S., McKay, R., Dunbar, R., Gore, D.B., Fink, D., Post, A.L., Miura, H., Leventer, A., Goodwin, I., Hodgson, D.A., Lilly, K., Crosta, X., Golledge, N.R., Wagner, B., Berg, S., van Ommen, T., Zwartz, D., Roberts, S.J., Vyverman, W., and Masse, G. (2014) Retreat history of the East Antarctic Ice Sheet since the last glacial maximum. Quaternary Sci. Rev., 100, 10–30, doi:10.1016/j.quascirev.2013.07.024

Marsiat, I. (1994) Simulation of the northern hemisphere continental ice sheets over the last glacial-interglacial cycle: Experiments with a latitude-longitude vertically integrated ice sheet model coupled to a zonally averaged climate model. Palaeoclimates 1, 59–98

Martin, M.A., Winkelmann, R., Haseloff, M., Albrecht, T., Bueler, E., Khroulev, C., and Levermann, A. (2011) The Potsdam Parallel Ice Sheet Model (PISM-PIK)–Part 2: Dynamic equilibrium simulation of the Antarctic ice sheet. The Cryosphere, 5, 727–740, doi:10.5194/tc-5-727-2011

Martín-Español, A., Zammit-Mangion, A., Clarke, P.,J., Flament, T., Helm, V., King, M.A., Luthcke, S.B., Petrie, E., Rémy, F., Schön, N., Wouters, B., and Bamber, J.L. (2016) Spatial and temporal Antarctic Ice Sheet mass trends, glacio-isostatic adjustment, and surface processes from a joint inversion of satellite altimeter, gravity, and GPS data. Journal of Geophysical Research – Earth Surface, 121, 182–200, doi:10.1002/2015JF003550

Meehl, G.A., Stocker, T.F., Collins, W.D., Friedlingstein, P., Gaye, A.T., Gregory, J.M., Kitoh, A., Knutti, R., Murphy, J.M., Noda, A., Raper, S.C.B., Watterson, I.G., Weaver, A.J., and Zhao, Z.C. (2007) Global Climate Projections. In: Climate change 2007: The physical science basis, contribution of Working Group I to the fourth assessment report of the Intergovernmental Panel on Clinate Change, edited by: Solomon, S., Qin, D., Manning, M., Chen, Z., Marquis, M., Averyt, K.B., Tignor, M., and Miller, H.L., Cambridge University Press, Cambridge, UK and New York, NY, USA.

Mercer, J.H. (1978) West Antarctic ice sheet and CO_2 greenhouse effect: a threat of disaster. Nature, 271(5643), 321–325, doi:10.1038/271321a0

Morland, L.W. (1987) Unconfined ice-shelf flow. In: Dynamics of the West Antarctic Ice Sheet, edited by: Van der Veen, C. J. and Oerlemans, J., Springer Netherlands, Glac. Quat. G., 4, 99–116.

Morlighem, M., Rignot, E., Seroussi, H., Larour, E., Ben Dhia, H., and Aubry, D. (2010) Spatial patterns of basal drag inferred using control methods from a full-Stokes and simpler models for Pine Island Glacier, West Antarctica, Geophys. Res. Lett., 37, L14502, doi:10.1029/2010GL043853

Naish, T.R., Woolfe, K.J., Barrett, P.J., Wilson, and 31 others (2001) Orbitally induced oscillations in the East Antarctic ice sheet at the Oligocene/Miocene boundary. Nature, 413(6857), 719–723, doi:10.1038/35099534

Naish, T., Powell, R., Levy, R., Wilson, G., Scherer, R., Talarico, F., Krissek, L., Niessen, F., Pompilio, M., Wilson, T., Carter, L., DeConto, R., Huybers, P., McKay, R., Pollard, D., Ross, J., Winter, D., Barrett, P., Browne, G., Cody, R., Cowan, E., Crampton, J., Dunbar, G., Dunbar, N., Florindo, F., Gebhardt, C., Graham, I., Hannah, M., Hansaraj, D., Harwood, D., Helling, D., Henrys, S., Hinnov, L., Kuhn, G., Kyle, P., Laufer, A., Maffioli, P., Magens, D., Mandernack, K., McIntosh, W., Millan, C., Morin, R., Ohneiser, C., Paulsen, T., Persico, D., Raine, I., Reed, J., Riesselman, C., Sagnotti, L., Schmitt, D., Sjunneskog, C., Strong, P., Taviani, M., Vogel, S., Wilch, T., and Williams, T. (2009) Obliquity-paced Pliocene West Antarctic ice sheet oscillations. Nature, 458(7236), 322–328, doi:10.1038/nature07867

Nowicki, S.M.J., Payne, A.J., Larour, E., Seroussi, H., Goelzer, H., Lipscomb, W., Gregory, J., Abe-Ouchi, A., and Shepherd, A. (2016) Ice Sheet Model Intercomparison Project (ISMIP6) contribution to CMIP6. Geosci. Model Dev., 9, 4521–4545, doi:10.5194/gmd-9-4521-2016

Nye, J.F. (1957) The Distribution of Stress and Velocity in Glaciers and Ice-Sheets. Proc. R. Soc. Lond. A, 239 113–133; doi:10.1098/rspa.1957.0026

Padman, L., Costa, D.P., Dinniman, M.S., Fricker, H.A., Goebel, M.E., Huckstadt, L.A., Humbert, A., Joughin, I., Lenaerts, J.T.M., Ligtenberg, S.R.M., Scambos, T., and van den Broeke, M.R. (2012) Oceanic controls on the mass balance of Wilkins Ice Shelf, Antarctica. Journal of Geophysical Research: Oceans, 117(C1), doi:10.1029/2011JC007301

Paterson, W.S.B. (1994) The physics of glaciers. Pergamon Press, Oxford, UK.

Pattyn, F. (2003) A new three-dimensional higher-order thermomechanical ice sheet model: Basic sensitivity, ice stream development, and ice flow across subglacial lakes. J. Geophys. Res., 108, 2382, doi:10.1029/2002JB002329

Pattyn, F. (2010) Antarctic subglacial conditions inferred from a hybrid ice sheet/ice stream model. Earth and Planetary Science Letters 295(3), 451–461, doi:10.1016/j.epsl.2010.04.025

Pattyn, F., Schoof, C., Perichon, L., Hindmarsh, R.C.A., Bueler, E., de Fleurian, B., Durand, G., Gagliardini, O., Gladstone, R., Goldberg, D., Gudmundsson, G.H., Huybrechts, P., Lee, V., Nick, F.M., Payne, A.J., Pollard, D., Rybak, O., Saito, F., and Vieli, A. (2012) Results of the Marine Ice Sheet Model Intercomparison Project, MISMIP. The Cryosphere, 6, 573–588, doi:10.5194/tc-6-573-2012

Pattyn, F., Perichon, L., Durand, G., Favier, L., Gagliardini, O., Hindmarsh, R.C., Zwinger, T., Albrecht, T., Cornford, S., Docquier, D., and Fuerst, J.J. (2013) Grounding-line migration in plan-view marine ice-sheet models: results of the ice2sea MISMIP3d intercomparison. J. Glaciol., 59, 410–422, doi:10.3189/2013JoG12J129

Payne, A.J., Holland, P.R., Shepherd, A.P., Rutt, I.C., Jenkins, A., and Joughin, I. (2007) Numerical modeling of ocean-ice interactions under Pine Island Bay's ice shelf. Journal of Geophysical Research: Oceans, 112(C10), doi:10.1029/2006JC003733

Pollard, D., and DeConto, R.M. (2009) Modelling West Antarctic ice sheet growth and collapse through the past five million years. Nature, 458(7236), 329–332, doi:10.1038/nature07809

Pollard, D., and DeConto, R.M. (2012a) Description of a hybrid ice sheet-shelf model, and application to Antarctica. Geosci. Model Dev., 5, 1273–1295, doi:10.5194/gmd-5-1273-2012

Pollard, D., and DeConto, R.M. (2012b) A simple inverse method for the distribution of basal sliding coefficients under ice sheets, applied to Antarctica. The Cryosphere, 6, 953–971, doi:10.5194/tc-6-953-2012

Pollard, D., DeConto, R.M., and Alley, R.B. (2015) Potential Antarctic Ice Sheet retreat driven by hydrofracturing and ice cliff failure. Earth and Planetary Science Letters, 412, 112–121.

Pralong, M.R., and Gudmundsson, G.H. (2011) Bayesian estimation of basal conditions on Rutford Ice Stream, West Antarctica, from surface data. J. Glaciol., 57, 315–324, doi:10.3189/002214311796406004

Pritchard, H.D., Ligtenberg, S.R.M., Fricker, H.A., Vaughan, D.G., Van den Broeke, M.R., and Padman, L. (2012) Antarctic ice-sheet loss driven by basal melting of ice. Nature, 484(7395), 502–505, doi:10.1038/nature10968

Raymo, M.E., Mitrovica, J.X., OĹeary, M.J., DeConto, R.M., and Hearty, P.J. (2011) Departures from eustasy in Pliocene sea-level records. Nature Geoscience, 4, 328–332. doi:10.1038/ngeo1118

Reeh, N. (1991) Parameterization of melt rate and surface temperature in the Greenland ice sheet. Polarforschung, 59, 113–128.

Rignot, E., and Jacobs, S.S. (2002) Rapid bottom melting widespread near Antarctic ice sheet grounding lines. Science, 296(5575), 2020–2023, doi:10.1126/science.1070942

Rignot, E., Casassa, G., Gogineni, P., Krabill, W., Rivera, A.U., and Thomas, R. (2004) Accelerated ice discharge from the Antarctic Peninsula following the collapse of Larsen B ice shelf. Geophysical Research Letters, 31(18), doi:10.1029/2004GL020697

Rignot, E., Mouginot, J., and Scheuchl, B. (2011) Ice flow of the Antarctic ice sheet. Science, 333, 1427–1430, doi:10.1126/science.1208336

Rignot, E., Jacobs, S., Mouginot, J., and Scheuchl, B. (2013) Ice-shelf melting around Antarctica. Science, 341(6143), 266–270, doi:10.1126/science.1235798

Ritz, C., Rommelaere, V., and Dumas, C. (2001) Modeling the evolution of Antarctic ice sheet over the last 420,000 years: Implications for altitude changes in the Vostok region. J. Geophys. Res., 106, 31943–31964, doi:10.1029/2001JD900232

Rogozhina, I., Petrunin, A.G., Vaughan, A.P.M., Steinberger, B., Johnson, J.V., Kaban, M.K., Calov, R., Rickers, F., Thomas, M., and Koulakov, I. (2016) Melting at the base of the Greenland ice sheet explained by Iceland hotspot history. Nature Geoscience, 9, 366–369, doi:10.1038/ngeo2689

Rott, H., Müller, F., Nagler, T., and Floricioiu, D. (2011) The imbalance of glaciers after disintegration of Larsen-B ice shelf, Antarctic Peninsula . The Cryosphere, 5(1), 125–134, doi:10.5194/tc-5-125-2011

Salamon, T. (2015) Sedimentary record of a Scandinavian Ice Sheet drainage system and till deposition over subglacial obstacles promoting basal sliding (an example from southern Poland). Sedimentary Geology, 330, 108–121, doi:10.1016/j.sedgeo.2015.10.005

Sato, T., and Greve, R. (2012) Sensitivity experiments for the Antarctic ice sheet with varied sub-ice-shelf melting rates. Ann. Glaciol., 53, 221–228, doi:10.3189/2012AoG60A042

Scherer, R.P., Aldahan, A., Tulaczyk, S., Possnert, G., Engelhardt, H., and Kamb, B. (1998) Pleistocene Collapse of the West Antarctic Ice Sheet. Science, 281(5373), 82–85, doi:10.1126/science.281.5373.82

Schodlok, M.P., Menemenlis, D., Rignot, E., and Studinger, M. (2012) Sensitivity of the ice-shelf/ocean system to the sub-ice-shelf cavity shape measured by NASA Ice-Bridge in Pine Island Glacier, West Antarctica. Annals of Glaciology, 53(60), 156–162, doi:10.3189/2012AoG60A073

Schoof, C., and Hindmarsh, R.C. (2010) Thin-film flows with wall slip: an asymptotic analysis of higher order glacier flow models. Q. J. Mech. Appl. Math., 63, 73–114, doi:10.1093/qjmam/hbp025

Schroeder, D.M., Blankenship, D.D., Young, D.A., and Quartini, E. (2014) Evidence for elevated and spatially variable geothermal flux beneath the West Antarctic Ice Sheet. Proceedings of the National Academy of Sciences, 111(25), 9070–9072. doi:10.1073/pnas.1405184111

Sergienko, O.V., and Hulbe, C.L. (2011) 'Sticky spots' and subglacial lakes under ice streams of the Siple Coast, Antarctica. Annals of Glaciology, 52(58), 18–22.

Shapiro, N.M., and Ritzwoller, M.H. (2004) Inferring surface heat flux distributions guided by a global seismic model: particular application to Antarctica. Earth Planet. Sc. Lett., 223, 213–224, doi:10.1016/j.epsl.2004.04.011

Shepherd, A., Wingham, D., Wallis, D., Giles, K., Laxon, S., and Sundal, A.V. (2010) Recent loss of floating ice and the consequent sea level contribution. Geophysical Research Letters, 37(13), doi:10.1029/2010GL042496

Shepherd, A., Ivins, E.R., Geruo, A., Barletta, V.R., Bentley, M.J., Bettadpur, S., Briggs, K.H., Bromwich, D.H., Forsberg, R., Galin, N., Horwath, M., Jacobs, S., Joughin, I., King, M.A., Lenaerts, J.T.M., Li, J., Ligtenberg, S.R.M., Luckman, A., Luthcke, S.B., McMillan, M., Meister, R., Milne, G., Mouginot, J., Muir, A., Nicolas, J.P., Paden, J., Payne, A.J., Pritchard, H., Rignot, E., Rott, H., Sørensen, L.S., Scambos, T.A.,

Scheuchl, B., Schrama, E.J.O., Smith, B., Sundal, A.V., van Angelen, J.H., van de Berg, W.J., van den Broeke, M.R., Vaughan, D.G., Velicogna, I., Wahr, J., Whitehouse, P.L.W., Duncan, J., Yi, D., Young, D., Zwally, H.J. (2012) A reconciled estimate of ice-sheet mass balance. Science, 338(6111), 1183–1189, doi:10.1126/science.1228102

Snyder, J. (1987) Map projections – a working manual (USGS Professional Paper 1395). United States Government Printing Office, Washington, USA.

Taylor, K.E., Stouffer, R.J., and Meehl, G.A. (2012) An overview of CMIP5 and the experiment design. Bull. Amer. Meteor. Soc., 93, 485–498, doi:10.1175/BAMS-D-11-00094.1

Timmermann, R., Wang, Q., and Hellmer, H.H. (2012) Ice-shelf basal melting in a global finite-element sea-ice/ice-shelf/ocean model. Annals of Glaciology, 53(60), 303–314, doi:10.3189/2012AoG60A156

Turner, J., Colwell, S.R., Marshall, G.J., Lachlan-Cope, T.A., Carleton, A.M., Jones, P.D., Lagun, V., Reid, P.A., and Iagovkina, S. (2005) Antarctic climate change durin the last 50 years, International Journal of Climatology, 25, 279–294, doi:10.1002/joc.1130

van der Veen, C.J. (1999) Fundamentals of glacier dynamics. A. A. Balkema, Rotterdam, The Netherlands.

Velicogna, I., and Wahr, J. (2013) Time-variable gravity observations of ice sheet mass balance: precision and limitations of the GRACE satellite data. Geophys. Res. Lett., 40(12), 3055–3063, doi:10.1002/grl.50527

Vizcaíno, M. (2014) Ice sheets as interactive components of Earth System Models: progress and chanllenges. Wiley Interdisciplinary Reviews: Climate Change, 5, 557–568, doi:10.1002/wcc.285

Weertman, J. (1964) Glacier sliding. U.S. Army Cold Regions Research and Engineering Laboratory (CRREL), CRREL Research Report 162, Hanover, NH.

Van Wessem, J.M., Reijmer, C.H., Morlighem, M., Mouginot, J., Rignot, E., Medley, B., Joughin, I., Wouters, B., Depoorter, M.A., Bamber, J.L., and Lenaerts, J.T.M. (2014) Improved representation of East Antarctic surface mass balance in a regional atmospheric climate model. J. Glaciol., 60, 761–770, doi:10.3189/2014JoG14J051

Wen, J., Wang, Y., Wang, W., Jezek, K.C., Liu, H., and Allison, I. (2010) Basal melting and freezing under the Amery Ice Shelf, East Antarctica. Journal of Glaciology, 56(195), 81–90, doi:10.3189/002214310791190820

Winkelmann, R., Martin, M.A., Haseloff, M., Albrecht, T., Bueler, E., Khroulev, C., and Levermann, A. (2011) The Potsdam Parallel Ice Sheet Model (PISM-PIK) – Part 1: Model description. The Cryosphere, 5, 715–726, doi:10.5194/tc-5-715-2011

Winsborrow, M.C.M., Clark, C.D., and Stokes, C.R. (2010) What controls the location of ice streams? Eart-Science Reviews, 103, 45–59, doi:10.1016/j.earscirev.2010.07.003

Yin, J., Overpeck, J.T., Griffies, S.M., Hu, A., Russell, J.L., and Stouffer, R.J. (2011)
Different magnitudes of projected subsurface ocean warming around Greenland and
Antarctica. Nature Geoscience, 4, 524–528, doi:10.1038/ngeo1189

Zachos, J.C., Quinn, T.M., and Salamy, K.A. (1996) High-resolution (104 years) deep-
sea foraminiferal stable isotope records of the Eocene-Oligocene climate transition,
Paleoceanography, 11(3), 251–266, doi:10.1029/96PA00571

Acknowledgements

First of all, I would like to express my gratitude to my advisors, Prof. Dr. Maik Thomas and Prof. Dr. Rupert Klein, for giving me the opportunity to carry out this Ph.D. as part of the graduate research school GeoSim. Special thanks to Prof. Thomas for receiving me in GFZ and providing everything I needed to complete this project: a workplace, resources, and continuous support. If I could go back in time and contribute to the decoration of his Ph.D. hat, it would be with a welcoming and ever-open office door.

For Dr. Irina Rogozhina, the most dedicated supervisor ever, I have no words to describe how much I appreciate her commitment to the success of my project. From her reply to my first e-mail from Chile asking for info regarding this position to her final comments on this thesis sent from the Alps, she always managed to find time for me, even when it meant working until *very* late hours during weekdays, weekends, and even holidays. She helped me shape every single application, poster, presentation, and manuscript, from which I learned what will surely form the core of the next steps of my career. In fact, these are the only paragraphs she never commented on, simply because I never showed them to her. I hope I don't get too many edits. Finally, and most importantly, I got a friend. Thank you for never letting me down.

To Christopher Irrgang, Ph.D.: Thank you, my friend. There are so many things I could mention here, but nothing would do justice to the infinite affection I feel for our friendship. You turned my daily work at our office into such a fun and enriching experience that I do not even remember those first six months when I was alone. I also lost count of the number of times you have helped me here in Germany; from simple hassles caused by my chileanness to very sad moments, your hand was always there to lift me up. Of course, all the good and special moments are and will remain vivid in my mind, and boy had we tons of them.

Thanks to all my colleagues at Section 1.3 for sharing such a nice workplace with me over the past three and a half years. It was literally my second home and I enjoyed my time with you all. I am looking forward to playing games and going out together more often now that the intensity of my workload will be dramatically decreased.

Above everything, I thank my family in Chile. My parents, Jorge and Alicia, my siblings, Andrea and Álvaro, and of course Céfiro and Sable, are the reason I am who I am. Here is where the text turns into a bunch of exotic words, but the summary is quite simple: I love them and miss them so much. Papá, Mamá, estoy muy orgulloso de que sean mis padres. Estar lejos me ha enseñado muchas cosas, pero definitivamente la más intensa ha sido descubrir que los quiero, admiro y extraño infinitamente más de lo que jamás imaginé. Ahora comprendo muchas cosas que cuando más joven ignoraba, y les agradezco el amor y paciencia con el que me criaron y protegieron. A ustedes les debo todo, y quiero que acepten este logro mío como un logro de ustedes. Intentaré darles la mayor cantidad de alegrías posible, pero sé que nunca podré igualar lo feliz que ustedes me han hecho. Andrea, gracias por siempre estar ahí para nosotros. Siempre nos has puesto por delante de tus prioridades personales, y no hay manera suficiente de expresar la admiración y respeto que siento por ti. Álvaro, gracias por ser mi camarada por tantos años. Echo de menos tu compañía, y añoro poder compartir mi vida contigo nuevamente. Los quiero mucho. Gracias por ser mi familia.

To my wife, Catalina, and our little son, Geo: I do this for you. Thank you, Cata, for your love and patience. Our life together started with our Ph.D. projects, and sharing this experience with you has been a blast. I enjoy and hold dear every single bit of this adventure, and I am glad that I can walk this life alongside someone like you. You have made me complete. Geo, my little man, I know you know.

Eidesstattliche Erklärung

Hiermit versichere ich an Eides statt, die vorliegende Dissertation selbstständig und ohne unerlaubte Hilfe angefertigt zu haben.

Bei der Verfassung der Dissertation wurden keine anderen als die im Text aufgeführten Hilfsmittel verwendet.

Ein Promotionsverfahren zu einem früheren Zeitpunkt an einer anderen Hochschule oder bei einem anderen Fachbereich wurde nicht beantragt.

_____   _____

Ort, Datum   Jorge Bernales